

UCSF

UC San Francisco Electronic Theses and Dissertations

Title

Single cell imaging in yeast reveals the interplay between organelle size scaling and proteosome dynamics that impacts major aging hallmarks

Permalink

<https://escholarship.org/uc/item/75q7c4ht>

Author

Mobaraki, Michael Esa

Publication Date

2023

Peer reviewed|Thesis/dissertation

Single cell imaging in yeast reveals the interplay between organelle size scaling and proteasome dynamics that impacts major aging hallmarks.

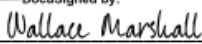
by
michael mobaraki

DISSERTATION
Submitted in partial satisfaction of the requirements for degree of
DOCTOR OF PHILOSOPHY

in
Developmental and Stem Cell Biology

in the
GRADUATE DIVISION
of the
UNIVERSITY OF CALIFORNIA, SAN FRANCISCO

Approved:

DocuSigned by:
 Wallace Marshall
43941FCFA7C0447... Chair

DocuSigned by:
 Hiten Madhani

DocuSigned by:
 Steven Altschuler

DocuSigned by:
 Hao Li
C2CA172BE8884DD...

Committee Members

Copyright 2023

By Michael Mobaraki

ACKNOWLEDGEMENTS

I am deeply grateful to my family for their unwavering support throughout the challenges and moments of hardship. My mother holds a special place in my heart for her relentless belief in me. It's because of her that I ventured into science and discovered my passion. She has been such a strong supporter in my career and life. My sister has been my lifelong pillar, always present whether it was to console me or review my papers. As a role model, she's been a constant source of reliability, bringing joy during my toughest times and always being there whenever I needed her. My father instilled in me the confidence that carried me through, especially during the tumultuous end of my PhD when the finish line seemed distant. A special note of appreciation goes to my aunts: Tooran, Katy, Iran, and Valeria. Even from afar, they made sure I never felt forgotten. Each of them showered me with motherly affection, be it through thoughtful care packages or uplifting words that brightened my day. I'm also thankful to my grandparents and cousins for their incredible support. Finally, my friends have been a cornerstone, offering both delightful moments and unwavering support throughout these lengthy years. We have laughed, cried, and celebrated together and they all made my PhD a remarkable journey. Shout out to Snow Naing and Fotie Kettle Chantiz. Snow Naing has been an incredible friend during these long years. We would often walk and motivate one another whether it was to eat a crazy amount of food or simply focusing on our science. She has been a true friend, a remarkable human who has taught me so much.

I would like to express my deepest gratitude to Hao Li for his support, patience, and kindness throughout the project. My appreciation also extends to Changhui Deng, who not only imparted his knowledge of yeast biology to me but also developed the DAP strain. Jiashun Zheng deserves special mention for creating an interface that facilitated the exploration of my data; his availability and responsiveness to questions and feedback were remarkable. Additionally, I'd like to extend my thanks to the rest of the Li lab especially to Jie Hong for teaching me how to use the microfluidic and flow cell cytometry.

I am immensely grateful for my committees' support and their invaluable feedback and the time they dedicated to meet with me individually. Hiten D. Madhani has consistently been a guiding light, generously offering his insight and always finding time to meet. Wallace Marshall's infectious enthusiasm for my project and his incisive questions greatly motivated me. His seminal work on mitochondria and vacuole morphology was the catalyst for my interest in the organelle phenotype. Last but by no means least, I'd like to thank Steve Altschuler for his astute insights and straightforward recommendations.

I would like to thank Soledad Reyes De Barboza Nabora and Diana Jurk for making the mice nucleus data available and for their prompt responses. Soledad is a wonderful human being, and I am extremely excited about her new lab! I also wish to express my gratitude to David Joy for assisting me with my deep learning challenges and early segmentation issues. His support and feedback were invaluable, especially during times when I felt overwhelmed and isolated. Even though he wasn't obligated, he would always find time to meet with me, whether via Zoom or in person, to discuss basic coding or deep learning problems. He's like a walking encyclopedia brimming with knowledge and is truly a remarkable individual.

Single cell imaging in yeast reveals the interplay between organelle size scaling and proteasome dynamics that impacts major aging hallmarks

Michael Mobaraki

ABSTRACT

Aging is a risk factor for many diseases, and understanding the hallmarks of aging is crucial for developing interventions to promote healthy aging. Despite the conservation of the aging hallmarks across phylogeny, the order in which these hallmarks appear and their relationship to each other remains unclear. To address these questions, we used the budding yeast *Saccharomyces cerevisiae* as a model organism due to its short lifespan and genetic tractability. The Li lab has developed a high-throughput microfluidics device to trap and monitor individual yeast cells over time. Using cell tracking technology, we quantified tagged proteins and classified different organelle phenotypes to predict lifespan based on cellular characteristics such as protein levels and organelle morphology. Our analysis revealed that the proteasome marker Rpn11p and size scaling is a strong predictor for proteostasis stress and mitochondrial dysfunction hallmarks. We identified slope changes and areas of certain organelles as strong predictors of replicative lifespan with differences in short-lived versus long-lived cells in maintaining a stable scaling ratio. We investigated the relationship between organelle scaling and protein dilution and found certain nuclear proteins to decrease with the increasing nuclear size. Our analysis revealed the proteasome as a regulator of the scaling ratio and influencer of the mitochondrial morphology and activity. We provide new insights into the mechanisms underlying aging and potential targets for interventions to promote healthy aging.

Table of Contents

INTRODUCTION	1
CHAPTER 1: Proteasome and scaling as a predictor of RLS with different aging trajectories..	6
ABSTRACT	7
RESULTS	8
DISCUSSION	28
CHAPTER 2: Determining causal relationship between nuclear size and proteasome.	29
ABSTRACT	30
RESULTS	31
DISCUSSION	41
CHAPTER 3: The proteasome and size scaling predicts and may drive aging hallmarks.	42
ABSTRACT	43
RESULTS	44
DISCUSSION	63
SUPPLEMENTAL	64
DISCUSSION	70
CONCLUSION	75
METHODS	76
REFERENCES	86

List of Figures

Fig 1.1. Li lab microfluidics layout	8
Fig 1.2. Screen top predictors for RLS based on protein intensity	10
Fig 1.3. Rpn11p Intensity correlations with RLS overtime	11
Fig 1.5. Proteostasis proteins maintain different aging dynamics	14
Fig 1.6. Nuclear proteins Hh01p, Whi5p, and Hsf1p display distinct trajectories	16
Fig 1.7. Cell area and nucleus area are strongly correlated to each other	17
Fig 1.8. Nucleus area negatively correlates with RLS	18
Fig 1.9. Ratio of nucleus area to cell area negatively correlates with RLS	19
Fig 2.1. Cell area does not strongly correlate with RLS	20
Fig 2.2. Cells with decreasing slope rate have a longer RLS	21
Fig 2.3. Bud generations of single cells reveal different increasing trajectories of organelle sizes	22
Fig 2.4.1. Nucleus area increases in aged mice livers	23
Fig 2.4.2. Nucleus area increases in aged mice lungs	24
Fig 2.5. Short-lived cells have a longer budding rate	25
Fig 2.6. Long-lived cells have an increasing nucleus and cell area with a steady scaling ratio	25
Fig 2.7. Rpn11p nuclear and cytoplasmic levels Differ in long-lived vs short-lived cells	26
Fig 2.8. Single cell curve representation displaying organelle area and Rpn11p trajectories	27
Fig 3.1. Granger causality reveals Rpn11p nuclear intensity as an early predictor of nucleus area	31
Fig 3.2. Proteasome perturbations influence the size scaling dynamics	32

Fig 3.3. Temporally perturbing the proteasome at 19.2hrs increases the scaling dynamics.	33
Fig 3.4. Nuclear size increase is not driven by nuclear influx of Rpn11p.	34
Fig 3.5. <i>fob1Δ</i>, <i>sgf73Δ</i>, and <i>dnm1Δ</i> display different scaling dynamics.	35
Fig 3.6.1. <i>fob1Δ</i>, <i>sgf73Δ</i>, and <i>dnm1Δ</i> separated by lifespan display similar dynamic trajectories. ...	
.....	36
Fig 3.6.2. Overexpression of proteasome separated by lifespan maintains rapidly increasing organelle size.	37
Fig 3.7.1. Survival curve of different constructs.	38
Fig 3.7.2. Growth curve of different constructs.	39
Fig 3.8. Measuring proteasome activity in different perturbation strains.	40
Fig 4.1. Classifying phenotypes and segmenting foci with AI.	45
Fig 4.2. Proteasome perturbation affects mitochondria morphology.	46
Fig 4.3.1. Perturbing mitochondrial morphology influences Cox4p and mitochondrial area.	47
Fig 4.3.2. Granger causality reveals that Rpn11p intensity is causal to Cox4p intensity.	48
Fig 4.4.1. Mitochondrial activity responds to proteasomal perturbations.	49
Fig 4.4.2. Cox4p overexpression does not impact Rpn11p or organelle scaling.	50
Fig 4.5. Loss of proteasome activity increases mitochondrial foci activity and size.	51
Fig 4.6. Cells displaying the mitochondrial dysfunction aging hallmark have a shorter RLS.	53
Fig 4.7. Mitochondrial morphology displays differences in scaling dynamics.	54
Fig 4.8. Cox4p and Rpn11p maintain distinct trajectories based on mitochondrial morphology.	
.....	55
Fig 4.9. Mitochondrial circular state has a greater number of foci.	55

Fig 5.1. Cells displaying proteostasis stress have a shorter RLS.	57
Fig 5.2. Hsp104p aggregates display distinct Rpn11p and size scaling trajectories.....	58
Fig 5.3. Granger causality reveals that Rpn11p cannot predict Hsp104p levels.....	60
Fig 5.4. Rpn11p temporal overexpression does not influence Hsp104p intensity.	61
Fig 5.5. Rpn11p may modestly increase the Hsp104p cytoplasm phenotype.....	62
Supplementary Table 1. Estradiol System Induction Strains	64
Fig. S1.1. Measuring estradiol dosage response by Rpn11p-GFP	65
Fig. S1.2. Observing Z4EM estradiol system in the microfluidics device.	66
Fig. S1.3. Validating methodology for non-linear Granger causality	68

List of Tables

Supplementary Table 1. Estradiol System Induction Strains 64

INTRODUCTION

Aging, a complex and multifactorial process, represents a major risk factor for numerous diseases. Understanding the hallmarks of aging is essential for developing interventions that promote healthy aging. Although the hallmarks of aging are conserved across phylogeny, the order in which they appear, and their interrelationships remain unclear¹⁻³. To address these questions, we employed the budding yeast *Saccharomyces cerevisiae* as a model organism, owing to its short lifespan, genetic tractability, and conservation of biological pathways with humans⁴⁻⁶. Some of the most notable aging pathways were first discovered in yeast such as the sirtuins and the mammalian target of rapamycin pathway^{4,6}. Unlike most mammalian cells, *S. cerevisiae* divide asymmetrically, producing a mother and daughter cell. *S. cerevisiae* replicative life span (RLS) studies measure how many daughter cells a mother can produce^{5,7}. RLS studies have been used to recapitulate aging in mitotically active cells^{6,7}. A single mother will produce ~10-25 daughter cells^{5,6}. Mother cells are larger than daughter cells and harbor harmful proteins that are implicated in aging itself^{5,8}. During the division of yeast cells, a mother cell will retain its' cell membrane, while a daughter cell will synthesize its own⁵. Past studies have used these differences to create microfluidic devices that can capture a mother cell by biotinylating its cell membrane and using streptavidin beads to bind the mother and flow pressure to remove new daughter cells. Other microfluidic devices relied on mothers' cell size to separate a mother and daughter cell^{5,9-11}. Major issues in using this method stem from clogging, the strength of biotinylating, inability to screen many strains, and loss of daughter or mother cells¹¹. To monitor the changing dynamics of a single yeast mother cell, the Li lab has developed a new microfluidics device that can perform high-throughput screening and imaging for *S. cerevisiae*. This is accomplished by using a *S. cerevisiae* strain that inhibits the expression of an essential membrane protein, Pma1p, in daughter cells, thereby arresting the daughter cells and allowing us to monitor single mother cells throughout their lifespan. We call the system daughter-arresting program (DAP). Unlike past microfluidic devices, which wash away daughter cells, DAP allows retention of the daughter cells, making it possible to measure lifespan by counting the number of daughter cells surrounding a mother cell. A mother cell can be distinguished from a daughter

cell by fluorescently tagging the essential membrane protein, which sequesters only to the mother cell. However, this method is optional as I have created an image analysis cell tracking tool to identify these single mother cells independent of the Pma1p membrane marker. Paring the high-throughput method with my image analysis pipeline; protein characterization, lifespan measurements, observations of organelle morphological changes, and cell cycle dynamics, all within a single cell can be monitored. The aggregated data reveals different trajectories in the aging process as well as relations to aging hallmarks. Among the twelve hallmarks of aging, four are readily observed in yeast, including genomic instability, epigenetic alterations, loss of proteostasis, and mitochondrial dysfunction^{1,2,7}. Other hallmarks are either inapplicable to yeast (stem cell exhaustion), may not be properly modeled by yeast (altered intracellular communication, cell senescence, disabled macroautophagy, chronic inflammation, and dysbiosis), or may not exhibit age-dependent changes (telomere attrition)^{1,2,7,12}. In *S. cerevisiae* and various other organisms, the environmental stress response (ESR) pathway impacts cellular homeostasis^{7,13}. While not explicitly classified as an aging hallmark, ESR is affected by the aging process in *S. cerevisiae*¹³. Previous studies have identified important cell cycle regulators that change over time and may function to arrest the cell cycle in aged cells¹⁴. Major age-associated pathways, such as proteostasis, have been extensively investigated in *S. cerevisiae*^{5,8,15,16}. Heat shock and chaperone proteins, which are highly conserved across eukaryotes, participate in proteostasis. They respond to environmental stress or protein aggregation by assisting in protein folding or degradation, thus implicating them in aging hallmarks^{5,17-19}. Hsp104p, a heat shock and chaperone protein in *S. cerevisiae*, can extend the lifespan of short-lived mutants when overexpressed and reduces misfolded proteins^{8,18,19}. Hsp104p has been identified as an early predictor of *S. cerevisiae* lifespan⁵. Hsp104p has also been used as a marker for observing the loss of proteostasis aging hallmark as the Hsp104p aggregates appear during times of proteostasis stress¹⁷. When cells suffer from an accumulation of misfolded proteins, Hsp104p will begin to aggregate and coalesce into specific protein inclusions found near the vacuole and nucleus. These Hsp104p protein inclusions are named as IPOD (Insoluble-Protein-Deposit), INQ (Intra-Nuclear-Quality-Control), and JUNQ (Juxta-Nuclear-Quality-Control)^{8,17-19}. The Hsp104p aggregates also appear within aged cells^{5,8,17}. Furthermore, when

misfolded proteins continue to accumulate, yeast cells upregulate the Rpn4 transcription factor to increase proteasome subunit proteins, such as the deubiquitinated lid protein Rpn11p^{20,21}. Rpn11p is part of the 19S proteasome subunit lid and has a role in removing the ubiquitination chains of proteins that are tagged for degradation²⁰. It is also one of the few proteasome proteins that can rescue mitochondrial morphology when overexpressed²². The proteasome is responsible for the degradation of proteins and is heavily relied on to remove misfolded proteins, as such the proteasome is tightly regulated to ensure proper cellular homeostasis. The transcription factor Rpn4p is a short-lived protein ($t_{1/2} \leq 2$ min) and is rapidly degraded by the proteasome and Ubr2p^{20,21}. Ubr2p is a ubiquitin-protein ligase (E3) and is involved in degradation of many cytoplasmic misfolded proteins²³. Rpn4p is degraded by a Ub-dependent degradation signal via the recognition of the 211–229 amino acids sequence²⁴. Rpn4p's Ub-independent degradation is mediated by the recognition of the first 1–10 amino acid sequence. The *ubr2* Δ extends RLS by enhancing proteostasis function in an Rpn4-dependent manner²¹. However, whether overexpression of Rpn4p alone is enough to increase RLS is debated as *ubr2* Δ impacts other pathways including the glucose repressor Mig1p. Additionally, Rpn4 can be overexpressed by removing both degradation sequences, the Δ 1–10 and Δ 211–229. The truncated Rpn4 (Rpn4*) does not increase cellular growth despite being transcriptionally active and increasing the proteasome^{24,25}. Despite the disparate results, the proteasome has recently been linked to various aging modes, suggesting an upstream role^{17,26}. Even within mammalian cells Rpn6p overexpression is beneficial to human embryonic stem cells and removal of aggregates in worms^{26,27}. Within the proteostasis pathway, extensive studies have been conducted on the vacuole and mitochondria in *S. cerevisiae*^{15,16}. The vacuole serves as the lysosomal and amino acid storage compartment in *S. cerevisiae*, playing a role in recycling proteins within the cell²⁸. Changes in vacuole acidity have been shown to lead to defective mitochondria^{15,16}. The relationship between these two aging hallmarks supports a linear cascade model of aging. Mitochondria, the powerhouse of the cell, is involved in various roles, including proteasome maintenance²⁹. In yeast, cellular respiration increases over time. The inner membrane subunit IV of cytochrome c oxidase, Cox4p, is involved in the electron transport chain. Several studies used Cox4p to measure mitochondrial activity such as cellular

respiration^{30,31}. In yeast, young mother cells will favor glycolysis more than cellular respiration, however, as the cell gets older, they will switch to cellular respiration³². What causes the switch in energy production remains largely unknown. One hypothesis stem from a decrease in glucose import possibly due to deregulated nutrient sensing or a decrease in the glucose transporters³². Different mitochondrial phenotypes have been associated with distinct aging trajectories^{15,33A} Interestingly, the amount and shape of the mitochondria changes in response to metabolic demands, yet the size of the mitochondria correlates strongly with the cell volume³⁴. Besides the mitochondria, many other cellular organelles have shown a strong correlation with cell size³⁵⁻³⁷. The cell size has been observed to increase with time in aged fibroblast cells and yeast cells^{34,36,38,39}. The scaling of organelle sizes is a conserved phenomenon that happens in even the smallest to the largest of animals^{37,38}. However, what drives the increase in cell size and organelle size remains largely unknown. One theory proposes that the increase in cell size is due to protein translation, this is largely supported from knockout out experiments of ribosomal proteins that decreases cell size and increases RLS^{35,40}. It is also unclear whether the scaling changes of organelle sizes is due to aging hallmarks or whether they may drive the appearance of these hallmarks. In this study, we explored the relationship between the proteasome and aging trajectories commonly found in long-lived cells. We identified the proteasome as a regulator of cell size to nucleus area ratio and discovered that proteasome perturbation influences mitochondrial morphology and activity. We demonstrated that the scaling of organelles is a strong predictor in the proteostasis stress and mitochondrial dysfunction aging hallmark. Our findings provide novel insights into the mechanisms underlying aging and further roles the proteasome may have. It also unveils for the first time a possible impact that scaling may have on the appearance of aging hallmarks. Furthermore, our results highlight the proteasome as an upstream regulator of organelle scaling. In summary, our study in *Saccharomyces cerevisiae* sheds light on the relationship between proteasome function and aging trajectories in long-lived cells, offering new perspectives in the intricate interplay between aging hallmarks. By elucidating the role of the proteasome as an upstream regulator of organelle scaling and a determinant of cell size to nucleus area ratio, our

findings contribute to a more comprehensive understanding of the aging process and suggest potential targets for interventions aimed at promoting healthy aging.

CHAPTER 1: Proteasome and scaling as a predictor of RLS with different aging trajectories.

ABSTRACT

This study investigates the complex interplay between various cellular components and their influence on Replicative Lifespan (RLS). Initially, our screen identified significant predictors for RLS, with a notable observation regarding the impact of Green Fluorescent Protein (GFP) tags on proteins. We identified Rpn11p as a strong predictor of RLS. Additionally, we identified contrasting behavior between the nuclear Rpn11p and cytoplasmic Rpn11p intensity. This was contrary to the chaperone protein Hsp104p. When examining the nucleus size changes, we identified the inverse between the increasing nucleus area and the decreasing Rpn11p nuclear intensity. Overall, our observational findings points to a possible relationship between the nucleus size and certain nuclear proteins.

RESULTS

Fig. 1.1A, depicts an overview of the microfluidic device set up, which depicts a 96 well plate that has been modified to trap and contain 32 different strains at a time; each well can hold 220 individual cells. The DAP strain uses the differences in asymmetric division between the daughter and mother cells to delineate between mother and daughter cells.

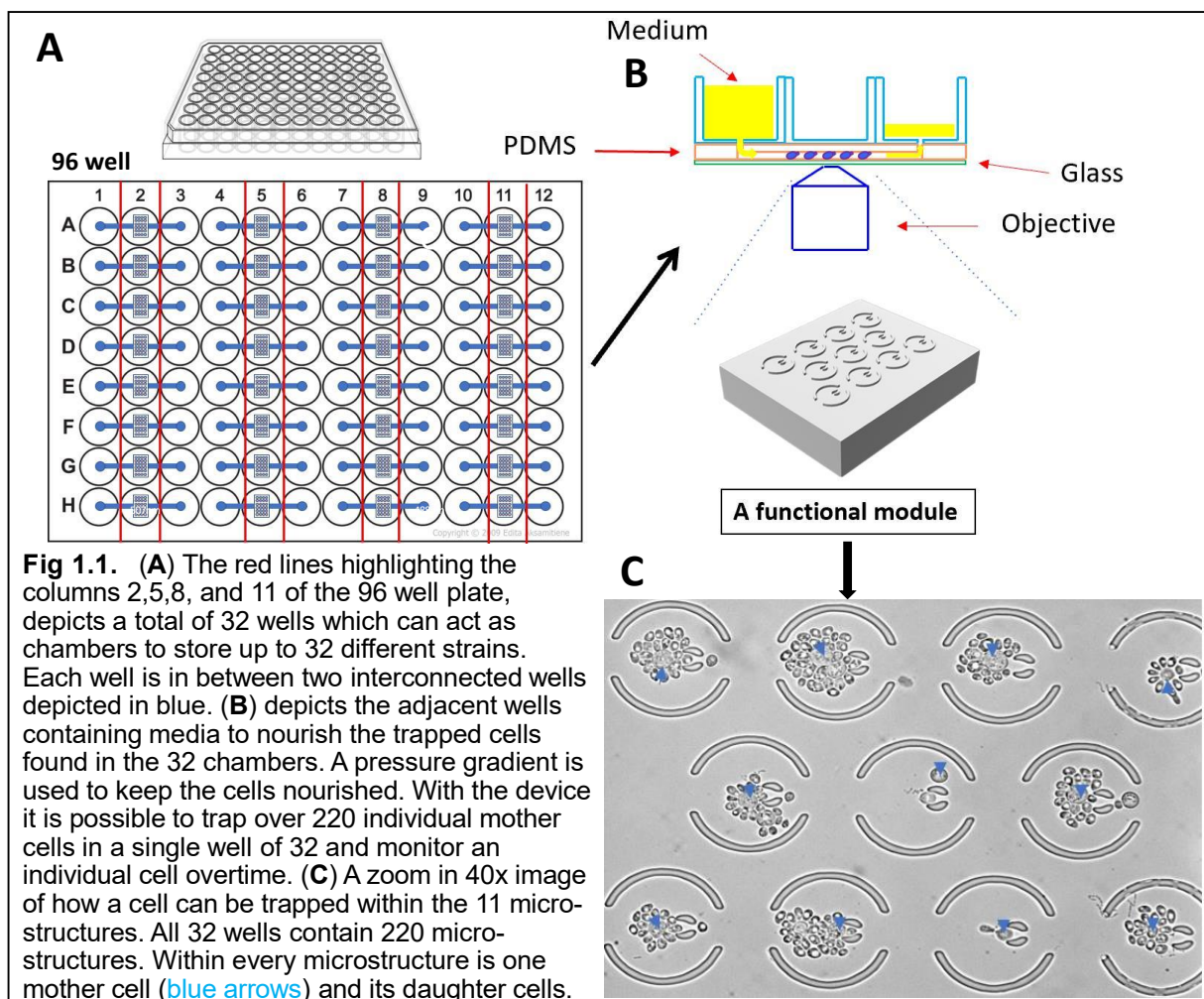


Fig 1.1. Li lab microfluidics layout

Our microfluidics device differs from past devices, as daughter cells are being arrested by inhibiting an essential membrane protein, Pma1p, needed for daughter cell propagation. The microfluidic

device uses a pressure gradient to move the flow of new media, thus keeping the cells nourished. The cells are plated on a 96 well plate, which can screen up to 32 different strains at a time. Each of the 32 wells, highlighted by the red lines in Fig. 1.1A, can hold up to 220 individual mother cells. Fig. 1.1A shows a layout of the device and Fig. 1.1C shows a 40X zoomed in image of cells trapped within a microstructure within an individual well. After exploring several datasets, we screened ~35 different markers and found the proteostasis and stress response pathways to be among our top hits. To quantify proteins and determine organelle structures, proteins were tagged with a Green Fluorescent Protein (GFP) on the carboxyl terminus⁴¹. Generated time series data measuring protein and phenotypic changes for over 20-100 individual dividing *S. cerevisiae* mother cells, per strain, in the span of 72 hours (images are taken every 20 minutes). Fig 1.2 depicts the correlations between our top hits of the GFP tagged strains. After quantifying GFP levels between differently tagged strains and filtering out false positives, I found Rpn11p, part of the 19s proteasome subunit lid, as our top predictor for RLS. Interestingly, we found different components of Rpn11p to have strong predictive properties.

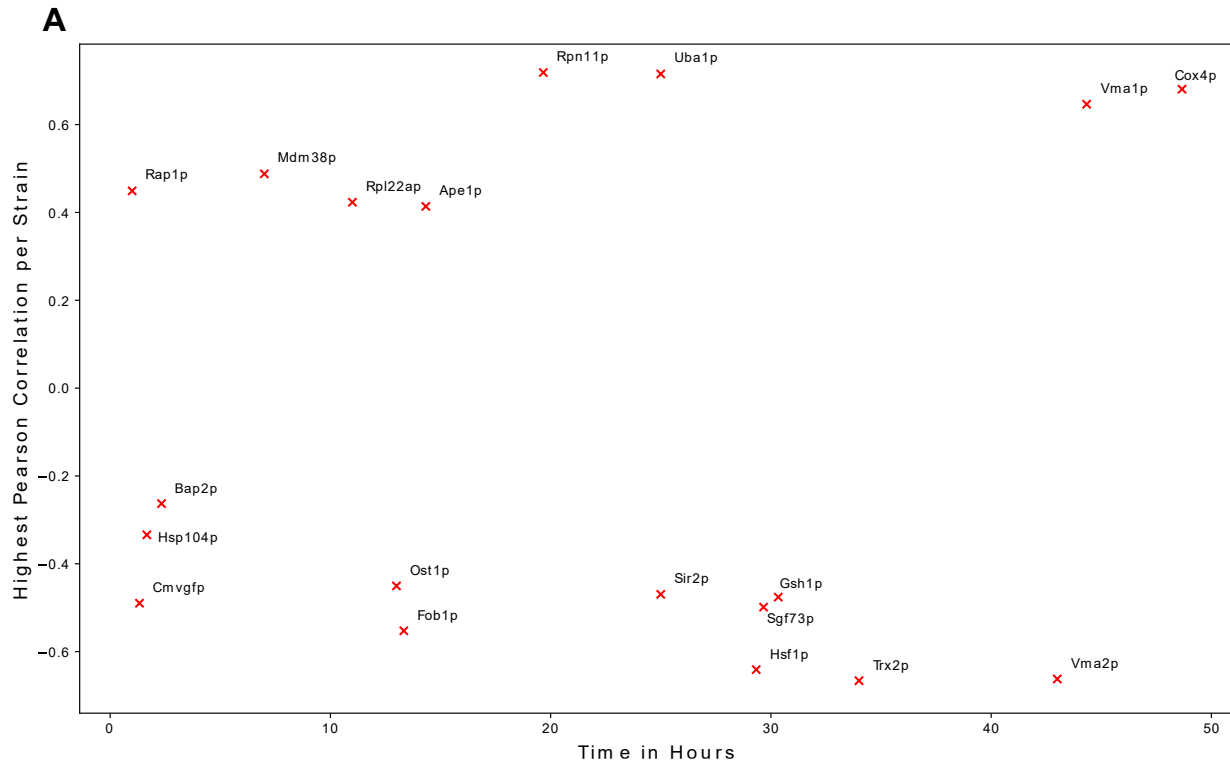


Fig 1.2. Screen top predictors for RLS based on protein intensity.

(A) The graph highlights the 19 most notable protein hits. Every red 'X' symbol on the graph corresponds to a distinct protein that was tagged with GFP at its carboxyl terminus. The x-axis represents the time in hours, marking the exact moment when the maximum Pearson correlation was detected for the cells. The number of cells was variable among the strains, with a minimum of 20 dividing cells being used for each Pearson correlation analysis.

Initially, many of these markers showed strong correlations, however, after careful observations some of the markers influenced lifespan like Rap1p or led to alternative phenotypes when tagged with other markers like Trx2p. Transcription factors and nuclear markers were dropped as they tended to influence lifespan or lead to unwanted phenotypic changes. Other nuclear markers like Fob1p, Sir2p, and Gsh1p had very weak GFP signal and were excluded in future downstream analysis. Cox4p is preferred over Mdm38p because of its relationship with cellular respiration, which tends to increase in older yeast cells^{30,31}. Ost1p proved to be very intriguing, however, obtaining proper organelle morphology proved to be challenging. Uba1p also had a strong correlation, however it is within the same pathway as Rpn11p and for this reason we decided to proceed with Rpn11p⁴². Rpn11p is part of the proteasome subunits, which is found in both the cytoplasm and the nucleus⁴³.

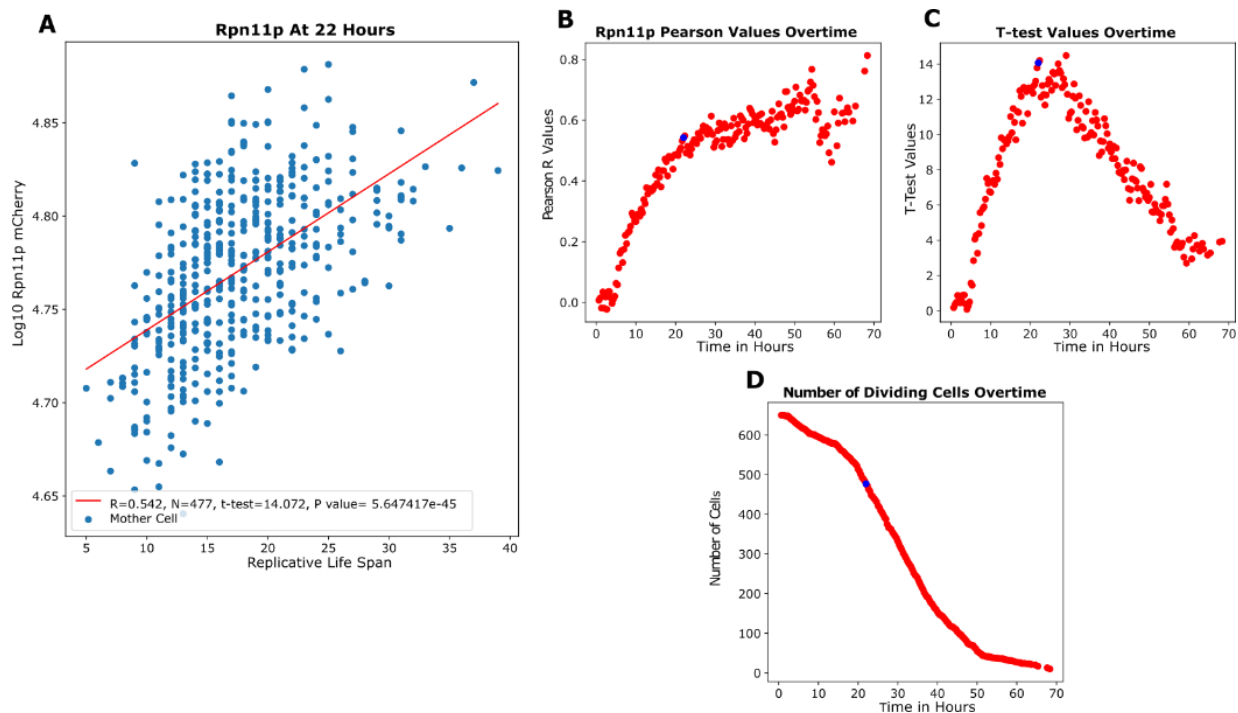


Fig 1.3. Rpn11p Intensity correlations with RLS overtime.

These graphs integrate data collected from dual-reporter strains of Rpn11p-mCherry. (A) The x-axis displays the Replicative Life Span (RLS) of individual mother cells that continue to divide at the 22-hour mark. The y-axis, in contrast, exhibits the log₁₀ intensity of Rpn11p, computed following the Mobaraki methodology. (B-D) delineates the time in hours, denoted on the x-axis, for cells in the process of division. The y-axis represents a variety of calculated outputs: the Pearson correlation coefficient, the t-test value, and the count of cells undergoing division over time. The blue dot highlights the instance at 22 hours where the Pearson correlation value reaches its apex, which is related to the number of cells and the t-test value. The presented data aggregates findings from 12 independent experiments, each differing in terms of the GFP-tagged protein, but consistently featuring an Rpn11p-mCherry tag (N= 650).

Proteasome function has been implicated to decline with cellular aging⁴⁴. Interestingly, we noticed that when Rpn11p regions are partitioned based on their localization, the nuclear levels of Rpn11p dropped significantly (Fig. 1.4B). Conversely, the cytoplasmic levels initially rise before eventually diminishing over time (Fig. 1.4C). To corroborate our observations, we examined the Rpn6p mCherry tagged levels in both subcellular regions (Fig. 1.4E-F). Rpn6p, also a component of the proteasome subunit, facilitates the coupling of the 19s and 20s constituents^{26,27}. Remarkably, in both scenarios, the proteasome proteins exhibited a decrease in their nuclear levels.

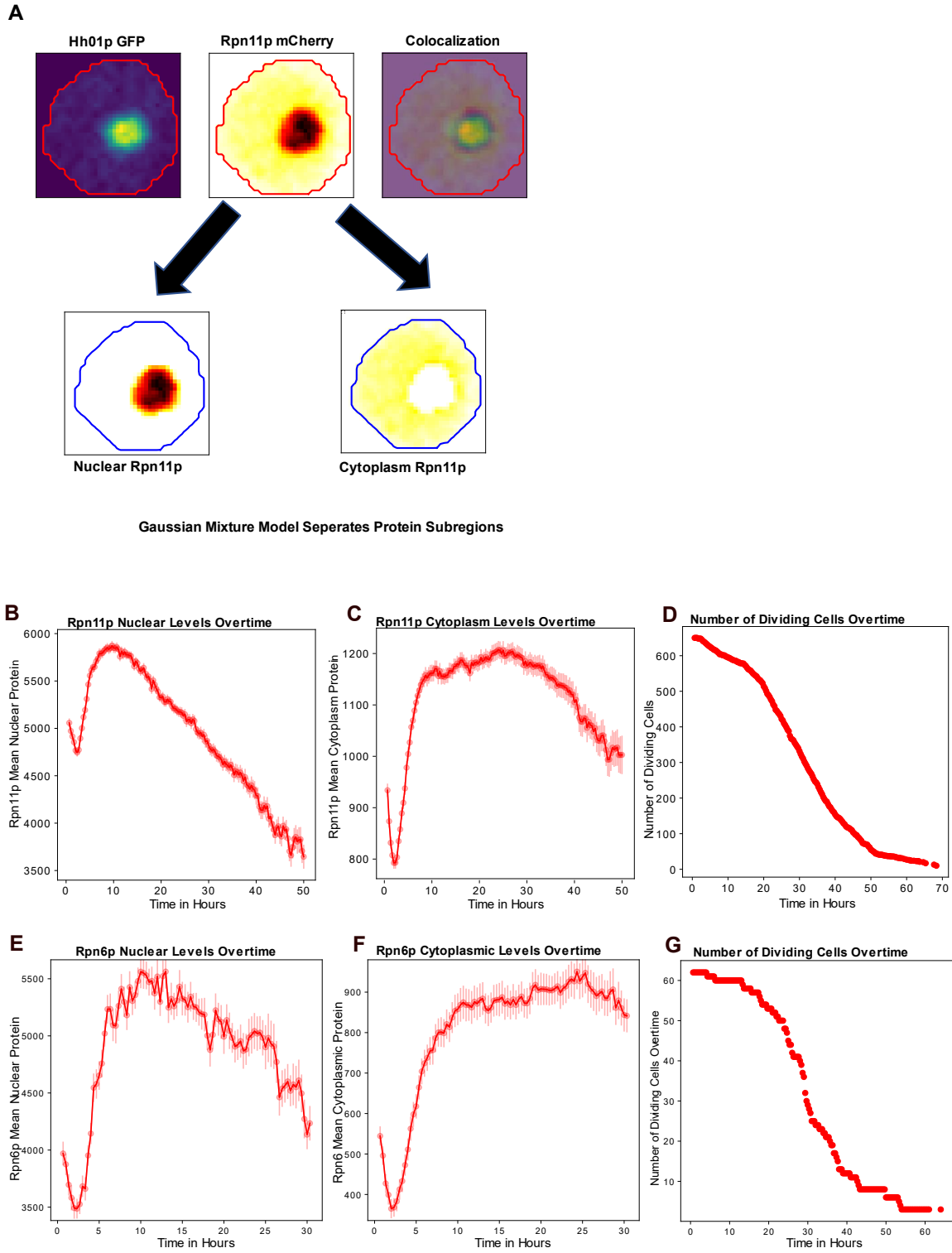


Fig 1.4. Proteasome proteins subcellular regions have different trajectories over time.

(Figure caption continued on the next page).

(Figure caption continued from the previous page).

(A) The image depicts a single cell from a dual-reporter strain, expressing Rpn11p-mCherry and Hh01p-GFP. Colocalization is apparent in the image on the far right. A Gaussian Mixture Model (GMM) is employed to segregate and quantify regions based on Rpn11p intensity. This method facilitates the determination of organelle shape and protein localization. (B-D) represents the aggregated Rpn11p data across 12 experiments. The time in hours is on the x-axis, tracking live cells that continue to divide. Only time points featuring a minimum of 25 cells are included in the analysis. (B) charts the mean nuclear intensity of Rpn11p over time. (C) displays the mean cytoplasmic intensity of Rpn11p over the same period. (D) enumerates the total number of dividing cells for each time point. The shaded region indicates the standard errors of the mean (SEM). (E-G), is the Rpn6-mCherry strain with a total of 62 cells being used. (E) is the nuclear Rpn6p intensity. (F) is the Rpn6 cytoplasmic intensity. (G) is the number of dividing cells overtime.

Upon noticing variations in Rpn11p levels across different subcellular regions, we next sought to understand how this decline relates to the Hsp104p chaperone protein, a component of the proteostasis pathway. Hsp104p is generally found in the cytoplasm, however, during periods of high stress the protein can be found to aggregate in the nucleus⁸. Prior studies have documented a time-dependent increase in Hsp104p⁵. To assess the interplay between proteasome and chaperone protein changes, we tagged Hsp104p and Rpn11p in the same cell and quantified their total mean, intensity, nuclear intensity, and cytoplasmic intensity. Although the combined protein sum increased over time, only Hsp104p displayed an overall increase in both cytoplasm and nuclear levels (Fig. 1.5). Intriguingly, this suggests that certain proteostasis pathway proteins, such as Hsp104p, might increase with time, while others like the proteasome decrease.

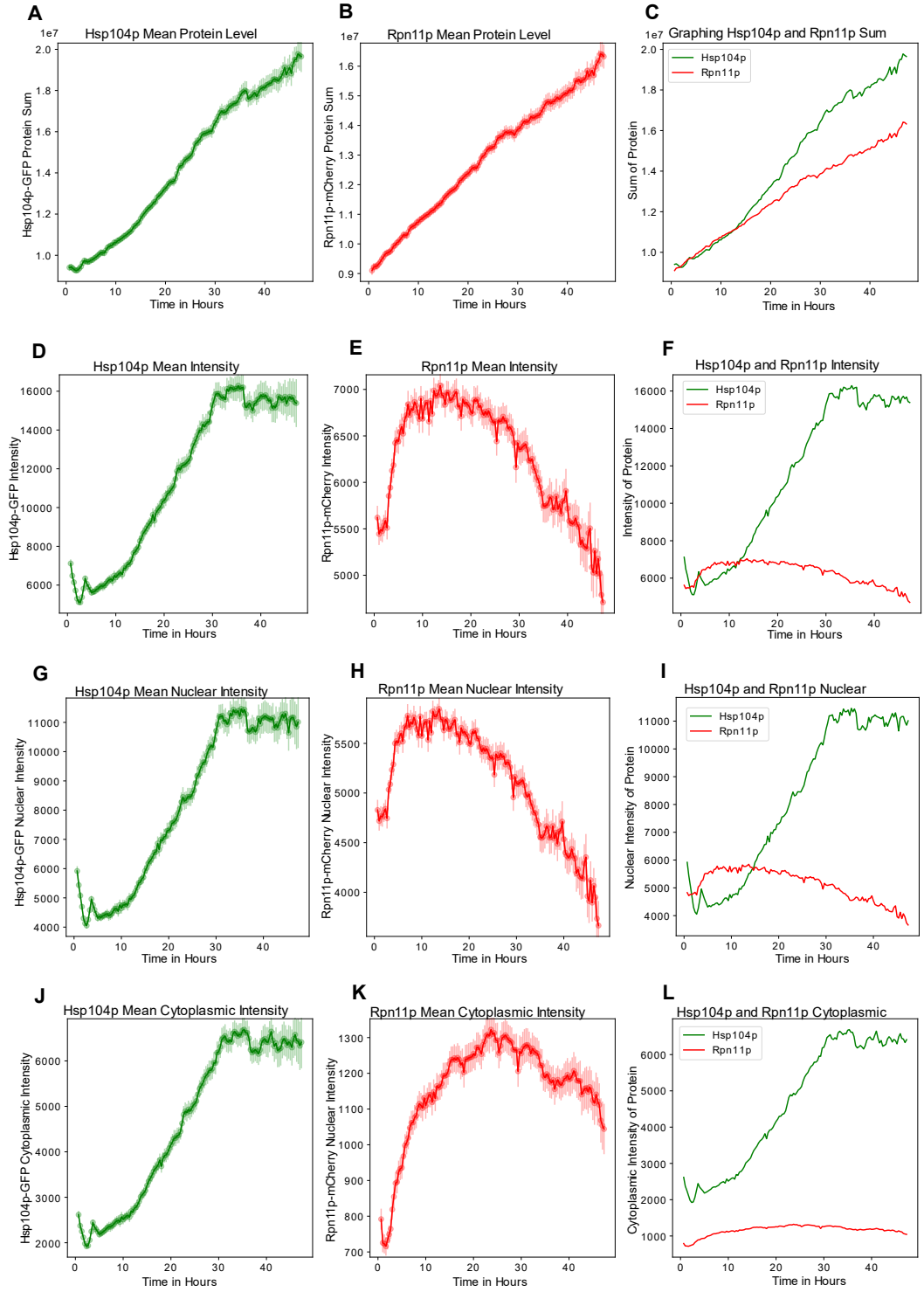


Fig 1.5. Proteostasis proteins maintain different aging dynamics.

(Figure caption continued on the next page).

(Figure caption continued from the previous page).

graphs are the average variations for Hsp104p-GFP and Rpn11p-mCherry mean protein levels in actively dividing live cells. It comprises separate plots for Hsp104p, Rpn11p, and a combined view of both proteins. (A-C), depicts the sum of proteins present within the cells. (D-F), is the protein intensities, which are normalized for the cell area. (G-I), is the nuclear intensity of the proteins. (J-L), is the intensity of the proteins in the cytoplasm. The nuclear and cytoplasmic sub-regions have been defined based on the GMM of the Rpn11p marker. The study incorporated a total of 127 cells, with time points that had fewer than 25 actively dividing cells being omitted. The data is the aggregation of two independent experiments. The SEM is represented by the shaded regions in the graph.

Considering our observation that nuclear Rpn11p levels decrease over time, we aimed to ascertain if this trend held true for other types of nuclear proteins. For this purpose, we measured Hsf1p, Whi5p, and Hh01p levels. Hsf1p, the heat shock transcription factor, is known to increase under conditions of heat shock or cellular stress⁵. Whi5p is a regulator of yeast cell cycle, while Hh01p is a histone protein^{45,46}. Our findings indicate that, in general, these proteins appear to increase. However, the trajectory of Hh01p aligns closely with that of Rpn11p (Fig. 1.6A). Conversely, the Hsf1p and Whi5p proteins seem to increase over time and maintain a relative steady state, illustrating a differential aging pattern amongst nuclear proteins (Fig. 1.6B-C).

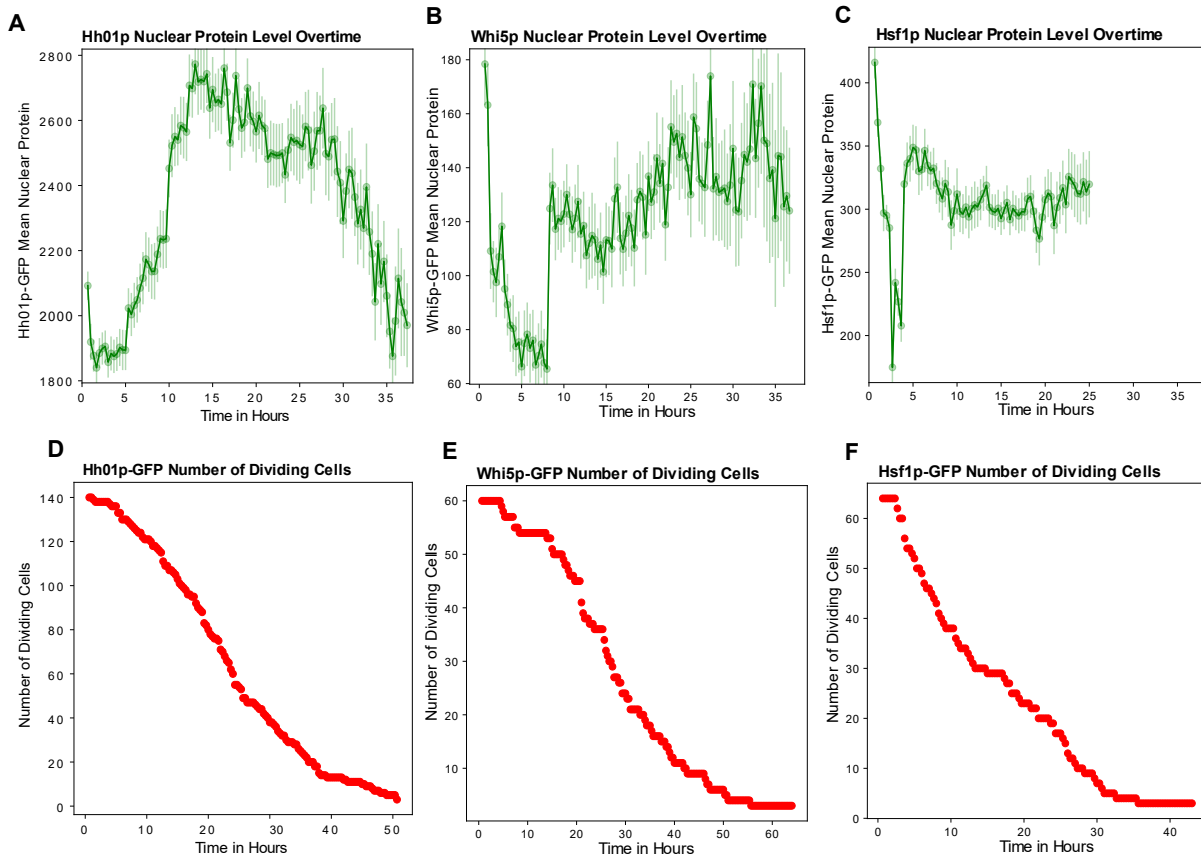


Fig 1.6. Nuclear proteins Hh01p, Whi5p, and Hsf1p display distinct trajectories.

(A-D), is the nuclear intensities of Hh01p, Whi5p, and Hsf1p all of which are tagged with GFP. The x-axis is the time in hours of live cells and the y-axis for the top three graphs is the mean protein nuclear intensity levels of the respective proteins. Times with less than 15 live dividing cells are omitted. The shaded areas are the SEM. (D-E) is the number of cells alive over time for the Hh01p, Whi5p, and Hsf1p tagged strains. Whi5p and Hsf1p both had an Rpn11p-mCherry tag. The Hh01p-GFP marker is an aggregation of our dual tagged Hh01p strains, some of which had Rpn11p-mCherry.

To investigate the factors behind the observed alterations in nuclear Rpn11p levels, we found a relation between increasing nuclear size and decreasing Rpn11p levels. With GMM, we determined the relative area of the nucleus and noted a time-dependent increase. This implies an increasing nucleus size could be diluting Rpn11p nuclear levels or the inverse. Our findings also revealed a strong correlation between nucleus area and cell area (Fig. 1.7A).

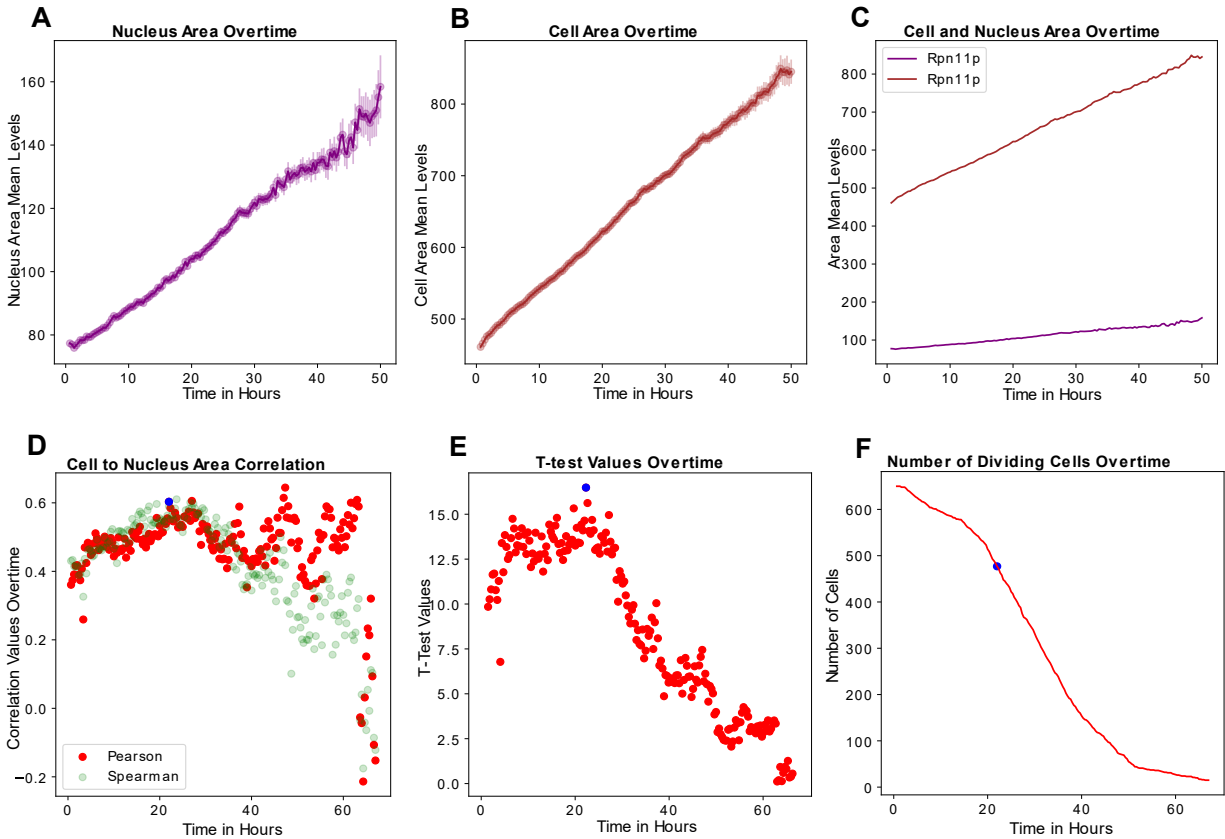


Fig 1.7. Cell area and nucleus area are strongly correlated to each other.

(A-C) The x-axis represents the time in hours for live dividing cells. These plots display the mean organelle areas of live cells. Times with less than 25 dividing cells are excluded. (A) illustrates the mean nuclear area over time. (B) presents the mean cellular area over time. The shaded area is the SEM. (C) concurrently is the mean nuclear and cellular areas over time, with the purple line indicating the nuclear area and the brown line representing the cellular area. (D) is the Spearman and Pearson correlation between cellular and nuclear area over time. Each dot corresponds to a Spearman value calculated using all dividing cells at that time, comparing their nuclear area to their cellular area. (E), is the t-test values calculated using the Pearson correlation. (F) Enumerates the sum of dividing cells per time. The blue dot represents when the strongest Pearson correlation with the highest number of dividing cells (time=22hrs, Pearson=.603, Spearman=.59, N= 477, t-test=16.48).

After observing an increasing nucleus area and cell area, we wanted to ascertain whether the organelle sizes correlated with RLS. Interestingly, the nucleus had the strongest negative correlation with RLS. Longer lived cells had a smaller nucleus area at 27 hours (Fig. 1.8A, $R=-.42$). The ratio between the nucleus to cell area also had a strong negative correlation with RLS at 27 hours (Fig. 1.9A, $R=-.444$). The ratio correlation is likely driven by the nucleus area as the cell area had a relatively weak correlation with RLS (Fig. 2.1A, $R=-.215$). The data suggests a potential relationship between scaling dynamics and RLS.

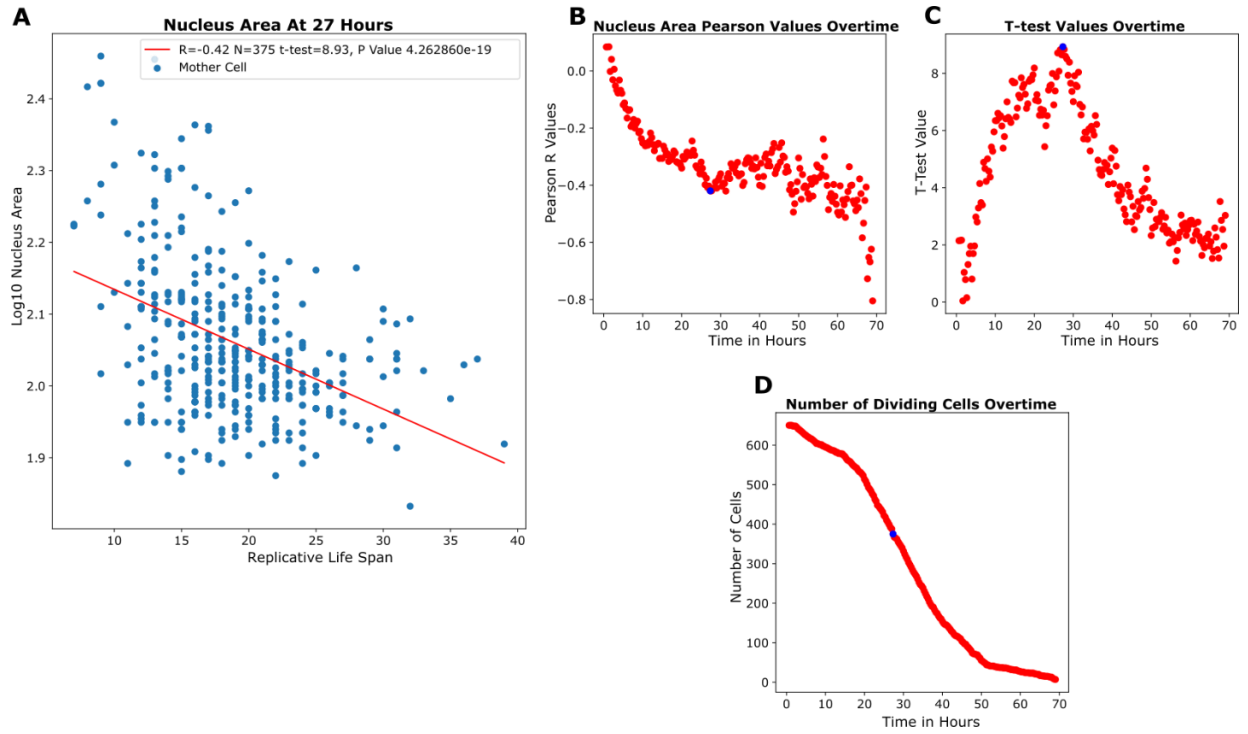


Fig 1.8. Nucleus area negatively correlates with RLS.

These graphs integrate data collected from dual-reporter strains of Rpn11p-mCherry. (A) is the strongest negative correlation between nucleus area and RLS at time 27 hours. The x-axis is the RLS of individual mother cells and the y-axis is the log10 nucleus area. Each blue dot represents a single mother cell. Pearson correlation is -0.42 , number of live cells is 375, P value is $4.262860e-19$, and t-test value is 8.93. (B) is the Pearson correlation between the nucleus area and RLS overtime. (C) is the t-test value corresponding to the Pearson correlation. (D) is the number of cells overtime which are still dividing.

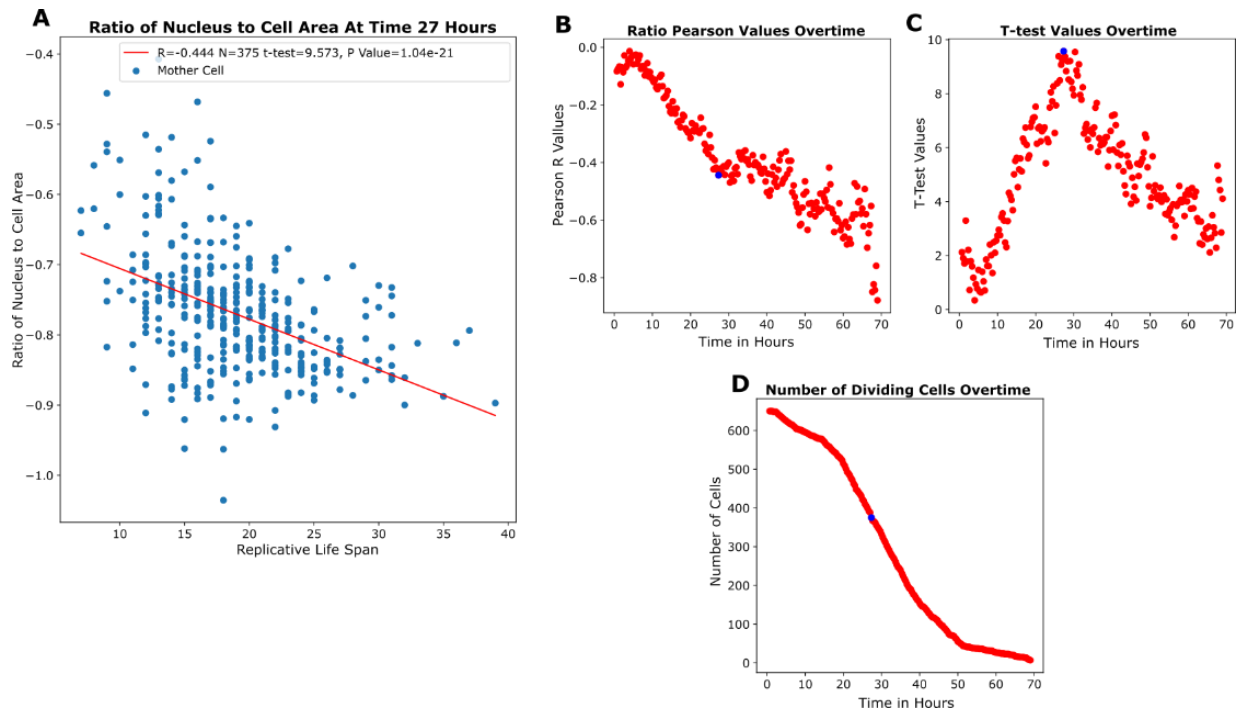


Fig 1.9. Ratio of nucleus area to cell area negatively correlates with RLS.

These graphs integrate data collected from dual-reporter strains of Rpn1^{1p-mCherry}. (A) is the strongest negative correlation between the ratio of the nucleus to cell area vs RLS at time 27 hours. The x-axis is the RLS of individual mother cells and the y-axis is the ratio of the nucleus to cell area. Each blue dot represents a single mother cell. Pearson correlation is -0.444 , number of live cells is 375, P value is $1.04e-21$, and t-test value is 9.573. (B) is the Pearson correlation between the ratio of the areas and RLS overtime. (C) is the t-test value corresponding to the Pearson correlation. (D) is the number of cells overtime which are still dividing.

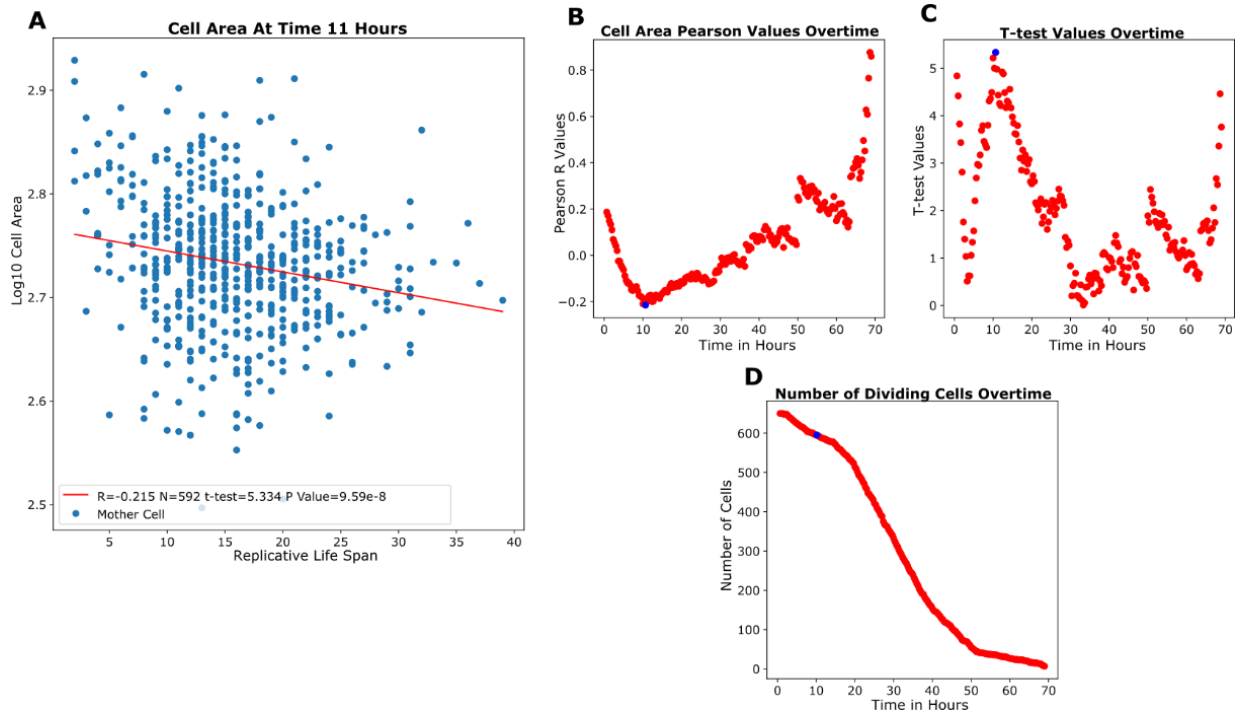


Fig 2.1. Cell area does not strongly correlate with RLS.

These graphs integrate data collected from dual-reporter strains of Rpn11p-mCherry. (A) is the strongest negative correlation between the cell area vs RLS at time 11 hours. The x-axis is the RLS of individual mother cells and the y axis is the cell area. Each blue dot represents a single mother cell. Pearson correlation is -0.215 , number of live cells is 592, P value is $9.59e-8$, and t-test value is 5.334. (B) is the Pearson correlation between the cell area and RLS overtime. (C) is the t-test value corresponding to the Pearson correlation. (D) is the number of cells overtime which are still dividing.

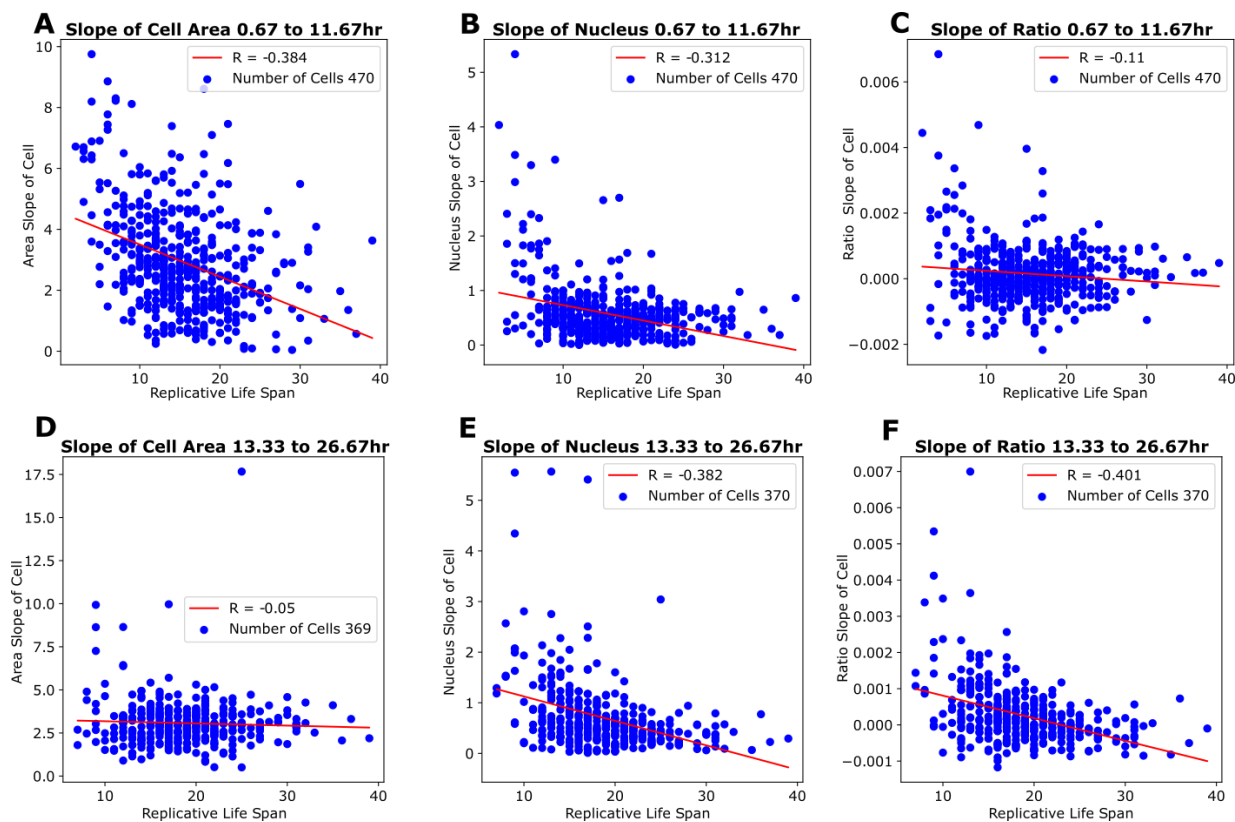


Fig 2.2. Cells with decreasing slope rate have a longer RLS.

The Slope rate of the Nucleus and Nucleus to Cell area ratio between .67-11.67 hrs and 13-26.67hrs. Cells are the aggregation of twelve independent experiments with a Rpn11p-mCherry tag. The x-axis is the RLS, and the y axis is the slope rate between the time intervals. Each Blue dot represents a single mother cell and its designated slope. (A-C), is the slope rate between .67-11.67 hours. (D-E) is the slope rate from 13.33-26.67 hours. Pearson correlation is displayed as the R values and number of cells is written in the box. Cells in which missing time points appeared during these intervals are removed.

Although the cell area had a relatively weak correlation with RLS, we found the slope rate of the cell area between .67 to 11.67 hours to be negatively correlated with RLS. Additionally, we found cells with a faster nuclear slope rate and ratio of nucleus to cell area between the hours of 13.3hrs to 26.6hrs had a shorter RLS. However, this correlation seems to be driven largely by short-lived cells (Fig. 2.2). The slope changes and the increasing cell area led us to explore whether trajectories between the cell area, nucleus area, and ratio existed between budding events. Our microfluidics device and continuous imaging of mother cells gives a detailed overview of cell growth and cell division dynamics, which can lead to mechanistic insight. We recorded the time at which each bud appeared and plotted the time interval between two successive budding events as a function of the generation (Fig. 2.3). We observed differing

dynamics between the cell area and nucleus area, where the cell area grows at a more linear rate while the nucleus area remains relatively consistent before increasing in size during the last few buds (Fig. 2.3B). Additionally, the ratio between the nucleus to cell area jumps towards the last few buds (Fig. 2.3C).

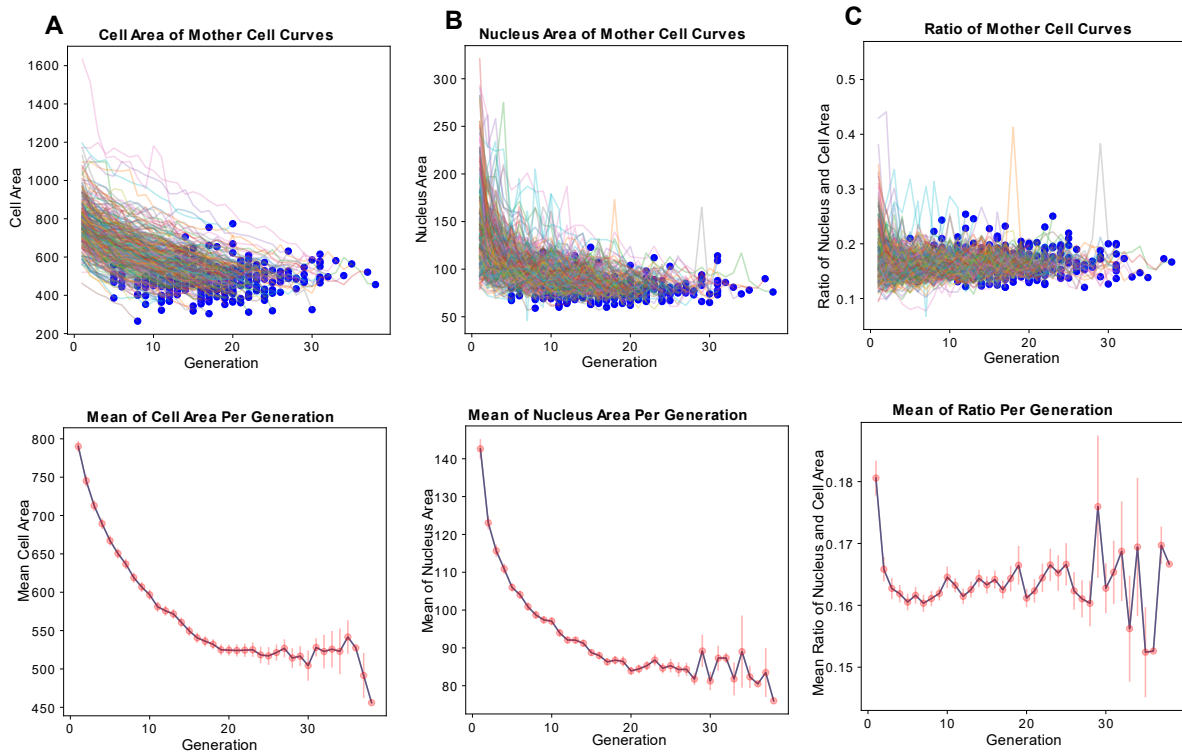


Fig 2.3. Bud generations of single cells reveal different increasing trajectories of organelle sizes.

(A-C) is the cell area, nucleus area, and ratio between the nucleus to cell area. The x-axis represents the number of buds left depicted as Generation and the y-axis represents the respective values. The time variable is removed as cells are synchronized by generation. Each blue dot represents the first budding event for the cells. The graphs on the bottom are the mean area curves of live budding cells. The standard error mean is depicted in the vertical pink line. The graphs are representative of the dynamics seen graphing 300 cells with RLS ranging from 5 – 40 buds.

Just like in yeast, passaged fibroblast cells have an increasing nucleus area³⁹. The nucleus area is also a biomarker of cellular senescence in fibroblast, astrocytes, and neuron cells³⁶. To determine whether the phenomenon of increasing nucleus size exists in other tissue types, I reanalyzed publicly available datasets^{47,48}. In differently aged mice liver tissue, the nucleus area increases in 24 months when compared to 3 months and 12-month-old mice (Fig. 2.4.1)⁴⁷. Additionally, when observing the nucleus area of cryosection lung samples, cells displayed an increasing nucleus area with time, except for the 2-month-

old mice (Fig. 2.4.2)⁴⁸. It is important to note that for both lung and liver sections I did not separate out specific cell populations. In the lung tissue, immune cells such as macrophages and monocytes are highly prolific⁴⁸. Overall, the increasing nucleus size highlights a conserved mechanism where nucleus size increases in older cells.

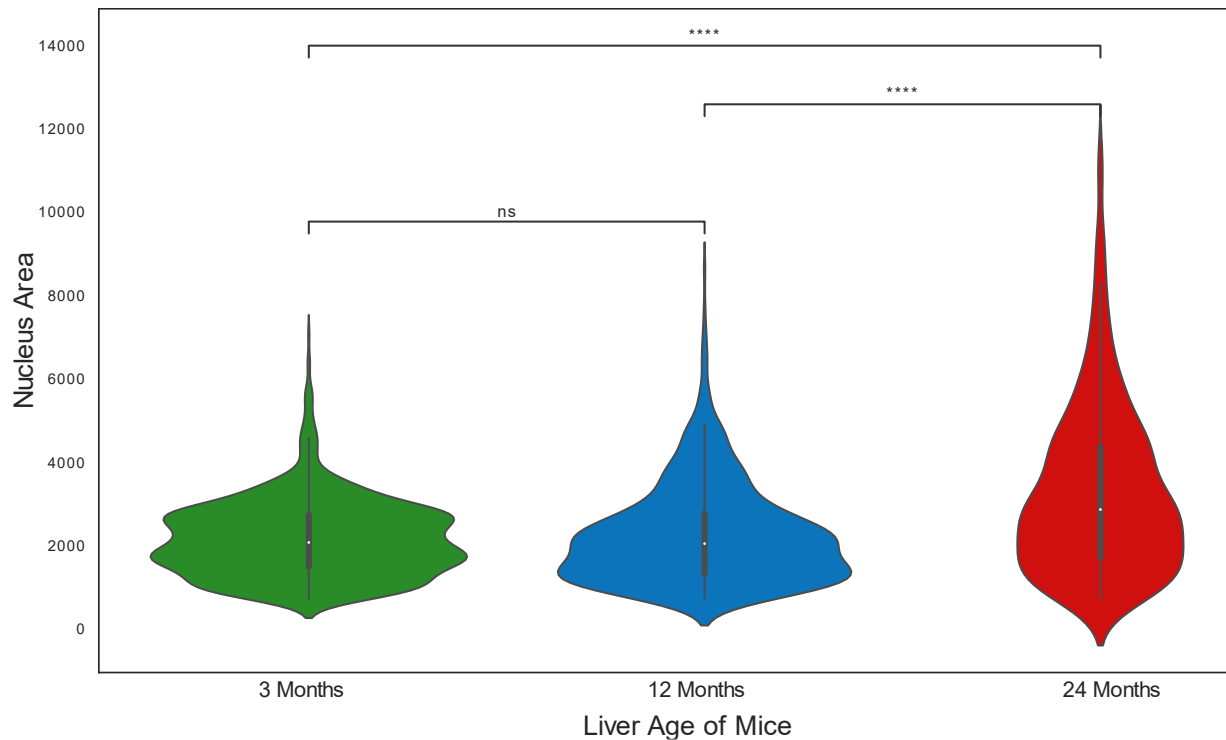


Fig 2.4.1. Nucleus area increases in aged mice livers.

(A), the violin plot depicts the differently aged mice in months and the y-axis displays the nucleus area of the differently aged mice. The white dot is the nucleus area median. There are ~1034 nucleus for 3 months, 693 nucleus for 12 months, and 616 nucleus for 24 months. Mann-Whitney U test is used to calculate the significance with $* < .05$. The P value for 12 months to 24 months is $9.931e-22$ and 24 months to 3 months is $8.245e-29$.



Fig 2.4.2. Nucleus area increases in aged mice lungs.

(A), the violin plot depicts the different aged mice lungs. PN5 is post-natal day. The y-axis displays the nucleus area of the differently aged mice. The white dot is the nucleus area median. There are 6016 cells for PN5, 2568 cells for 2 weeks, 13041 cells for 1.5 months, 9288 cells for 2 months, 3385 cells for 13 months, and 3900 cells for 18 months. Mann-Whitney U test is used to calculate the significance with $* < .05$.

Because of the predictive properties of organelle shape, I next explored whether different trajectories exist between short-lived vs long-lived cells. Short-lived cells are defined as mother cells with less than 15 total buds and long-lived have 15 or more buds. When observing the budding rate overtime, short-lived cells had a longer budding rate when compared to long-lived cells overtime (Fig. 2.5A). When separating the sizing trajectories between the two groups, the mean nucleus area and scaling ratio of the nucleus to cell area was higher in short-lived cells overtime (Fig. 2.6).

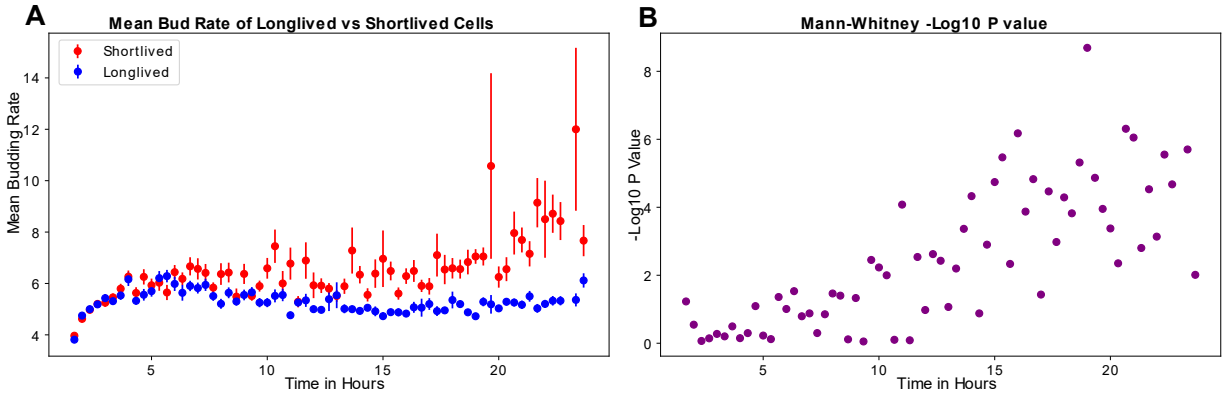


Fig 2.5. Short-lived cells have a longer budding rate.

Plot displays the budding rate difference between long-lived vs short-lived cells. The x-axis is the time in hours of live dividing cells. Time points containing less than 10 actively dividing cells are dismissed. (A), is the mean budding rate of dividing cells on the y-axis. The SEM is depicted as error bars. (B), is the $-\log_{10}$ P value calculated using Mann-Whitney t-test. Cells are the aggregation of twelve independent experiments with a Rpn1 1p-mCherry tag.

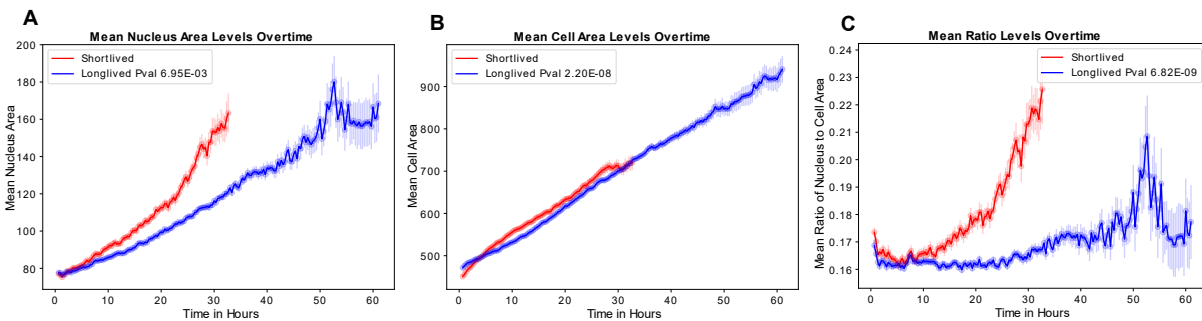


Fig 2.6. Long-lived cells have an increasing nucleus and cell area with a steady scaling ratio.

The figure displays the nucleus and cell area differences in short-lived vs long-lived cells. Short-lived cells are classified as cells with a RLS less than 15 and long-lived is classified as cells greater than or equal to 15. The x-axis is the time in hours of live dividing cells. Times with less than 25 actively dividing cells are excluded. The red curves are the short-lived cells (N=327, mean RLS=9.16) and the blue curves are the long-lived cells (N=323, mean RLS= 20.21). (A) is the mean nucleus area of the short-lived in red and the long-lived cells in blue (P value is $6.95e-3$). (B) is the mean cell area of the short-lived in red and the long-lived cells in blue (P value is $2.20e-8$). (C) is the nucleus to cell area ratio (P value $6.82e-9$). All P values are calculated using the Mann-Whitney U test. SEM is the shaded region. Cells are the aggregation of twelve independent experiments with a Rpn1 1p-mCherry tag.

Seeing that short-lived and long-lived cells displayed distinct sizing trajectories, we sought to determine whether the same cells had similar Rpn1 1p trajectories. We found that the short-lived cells had a steeper decline in nuclear Rpn1 1p intensity and a higher cytoplasmic Rpn1 1p intensity (Fig. 2.7). This is contrary to the chaperone protein Hsp104p, which is found to increase with time (Fig. 1.5). Fig. 2.8

depicts a representative curve of a single cell. Keep in mind not all cells display the same exact trajectories.

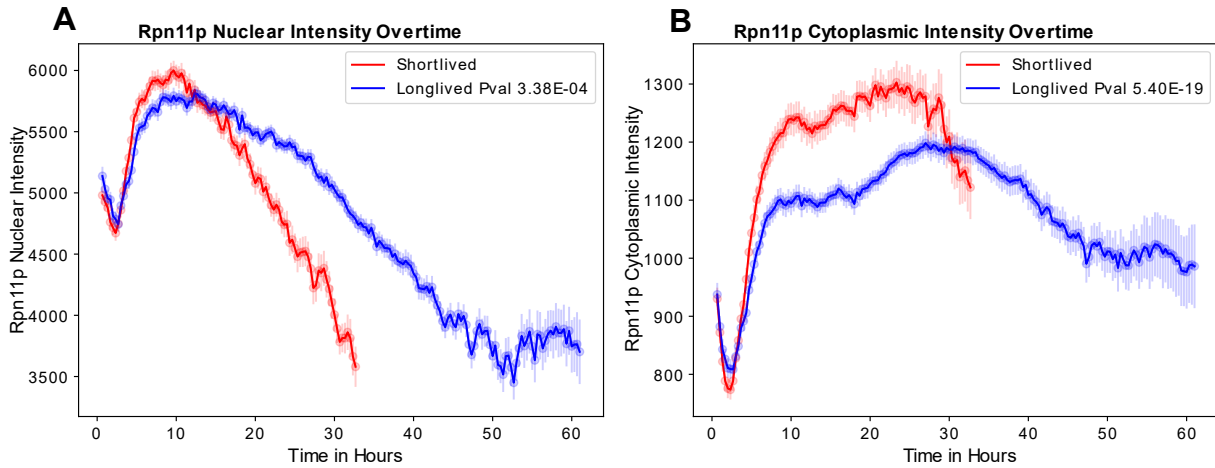


Fig 2.7. Rpn11p nuclear and cytoplasmic levels Differ in long-lived vs short-lived cells.

The figure displays Rpn11p differences in short-lived vs long-lived cells. Short-lived cells are classified as cells with a RLS less than 15 and long-lived is classified as cells greater than or equal to 15 RLS. The x-axis is the time in hours of live dividing cells. The red curves are the short-lived cells (N=327, mean RLS=9.16) and the blue curves are the long-lived cells (N=323, mean RLS= 20.21). (A) is the mean Rpn11p nucleus intensity of the short-lived in red and the long-lived cells in blue (P value is 3.38e-4). (B) is the mean Rpn11p cytoplasmic intensity of the short-lived in red and the long-lived cells in blue (P value is 5.40-19). All P values are calculated using the Mann-Whitney U test. SEM is depicted as the shaded area.

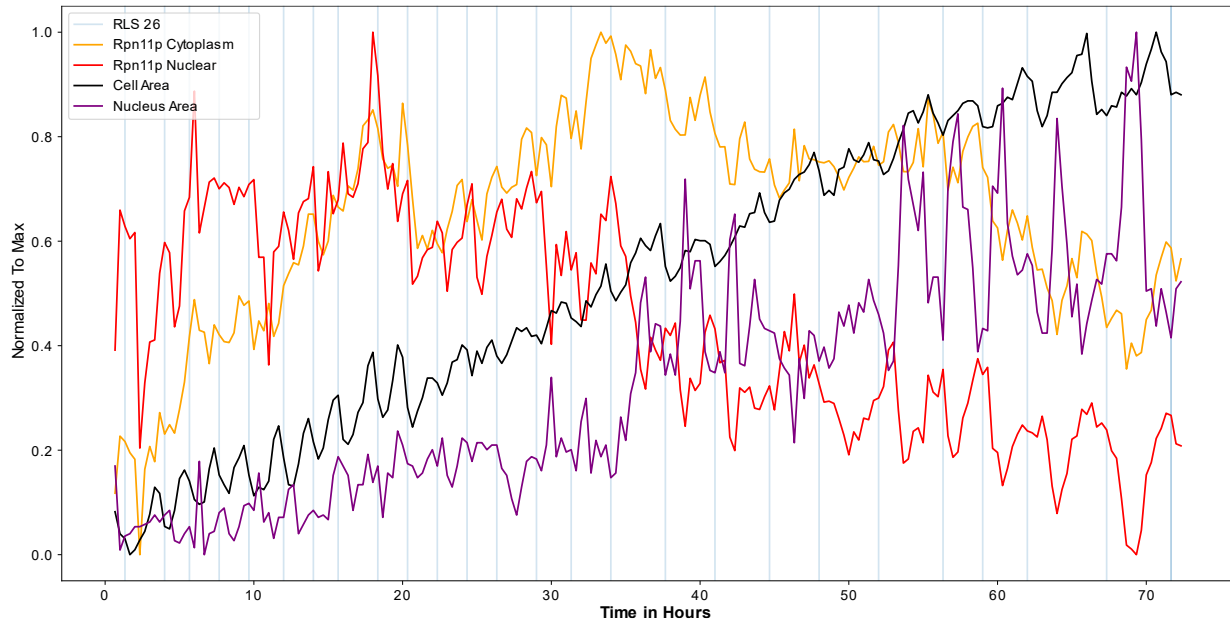


Fig 2.8. Single cell curve representation displaying organelle area and Rpn11p trajectories.

Plot displays a representative image of a single cell's organelle areas and Rpn11p changes. The x-axis is the time in hours. The cell is imaged every 20 minutes. The y-axis is the normalized levels of the values from 0 to 1. The blue vertical line is the appearance of a bud. The orange curve is the Rpn11p cytoplasmic intensity, and the red curve is the Rpn11p nucleus intensity. Both are identified using the GMM. The black curve displays the cell area, and the purple curve is the nucleus area.

DISCUSSION

Our initial screen pinpointed potent predictors for RLS (Fig. 1.2). Notably absent from existing literature is the potential impact of GFP tags on proteins; we observed that certain tags reduced lifespan. Rpn11p emerged as having a robust correlation with RLS. Upon partitioning Rpn11p regions, we noted the cytoplasm's modest rise over time before its decline, while the nuclear region consistently decreased (Fig. 1.4). Contrarily, not all proteostasis proteins exhibited this decline, with Hsp104p presenting a more linear increase (Fig. 1.5). It raises the question of why cells might increase Hsp104p levels but not those of proteasome proteins. It's plausible that a regulatory disconnect exists within the proteostasis pathway since one would anticipate the cell bolstering both pathways under heightened proteostasis stress. Intriguingly, nuclear proteasome proteins appear to wane over time (Fig. 1.4). The trigger for this decline remains elusive, but our observations hint at a possible link with the expanding nucleus area over time (Fig. 1.7). Yet, this decrease in nuclear proteins isn't universal; proteins like Whi5p and Hsf1p displayed increasing concentrations (Fig. 1.6), hinting that certain proteins might adjust in proportion to organelle size. Whether this adaptation is promoter- or protein-driven is an open question. Our data further revealed both nucleus and cell areas expanding over time, with only the latter showing a steady linear trajectory (Fig. 1.7 and Fig. 2.3). Unlike the cell area that maintained a steady increase over time, the nucleus area displayed a rapid growth towards the last generations (Fig. 2.3). One possibility is that the nucleus size is adapting to match the cell size, implying that an increase in cell area might stimulate the nucleus to expand, potentially driven by cytoplasmic protein translation. This could also be propelled by an augmented extracellular protein import. This phenomenon of nucleus size augmentation is also evident in various mouse tissues, suggesting evolutionary conservation. In short-lived cells, we discerned distinct patterns in both scaling size and Rpn11p levels (Fig. 2.6 and Fig. 2.7). These varied trajectories imply a potential causal link between proteasome dysregulation and size scaling.

CHAPTER 2: Determining causal relationship between nuclear size and proteasome.

ABSTRACT

The causes and drivers of aging have remained unclear for a long time. It is still uncertain whether aging occurs in a linear cascade model or a parallel model. In our previous chapter, we identified changes in nucleus size and proteasome nuclear intensity. Whether one is causal of the other remains to be elucidated. Methods to understand temporal patterns are often confounded by the difficulty of capturing nonlinear relationships. Interestingly, most real-world time series examples, including our own dataset, are non-linear. Here, I utilized a non-linear Granger causality approach to determine whether changes in the proteasome preceded those of the nuclear area. I found the proteasome to be a strong determinant of nucleus size. Alterations in the proteasome led to an increased nucleus size, but interestingly, this was not due to an influx of Rpn11p into the nucleus, suggesting a strong relationship between the active proteasome and nucleus size scaling.

RESULTS

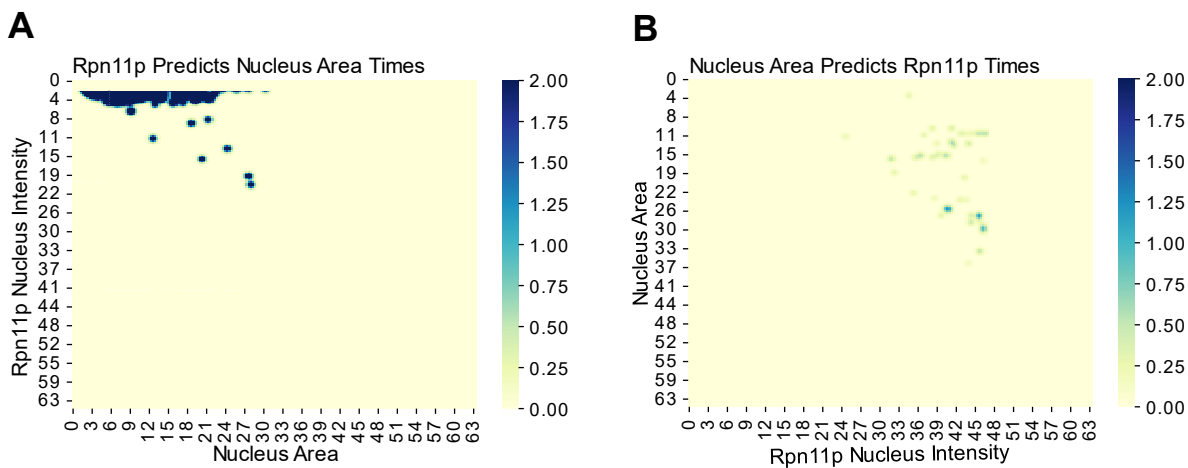


Fig 3.1. Granger causality reveals Rpn11p nuclear intensity as an early predictor of nucleus area.

Predicting temporal order using Granger causality with decision trees. The following heatmaps display the $-\log_{10} P$ values calculated from an F-test. (A), is using Rpn11p nuclear intensity to predict nucleus area in later times. (B), predicting Rpn11p nuclear intensity based on nucleus area. The time points for both the y-axis and x-axis are the time in hours for the respective variables. Dataset is an accumulation of our Rpn11p-mCherry strains with ~650 cells. Time points with less than 56 dividing cells are excluded.

Seeing that the proteasome dynamics and scaling size seemed to be related, we wanted to determine the temporal order between the Rpn11p nuclear levels and nucleus area. By using Granger causality with decision trees, I captured the non-linear relationships of the variables and determined temporal ordering between the nucleus area and proteasome⁴⁹⁻⁵¹. The exact method was tested and validated using our mitochondrial and vacuole dataset (see supplemental and methods). Surprisingly, our model indicated that Rpn11p nuclear intensity is predictive of the nucleus area during earlier times of 2-5 hours (Fig 3.1A). On the other hand, the nucleus area seemed to be weakly predictive of Rpn11p intensity (Fig 3.1B). Although our non-linear Granger causality approach indicated a sequential order, it cannot alone determine causality. To prove causality, we sought to perturb the proteasome and determine whether scaling dynamics are also perturbed. Decreasing the proteasome through the *rpn4* Δ curtailed lifespan and led to a higher nucleus size and ratio between nucleus to cell area (Fig. 3.2A-E). Interestingly, by amplifying the proteasome via *ubr2* Δ deletion, both the nuclear area and the overall cell

size are enlarged (Fig. 3.2F-J). This facilitates the maintenance of a stable scaling ratio between the nuclear and cell area over an extended duration. To verify the influence of proteasome activity on the scaling ratio, I induced Rpn4* variant at 5.5 hours using an estradiol-inducible system. Rpn4*, is known for its stability and resistance to Ubr2-mediated degradation^{24,25} (Fig. 3.2K-O). As expected, Rpn11p levels increased along with cell area, nucleus area, and the ratio. This indicated that the proteasome changes influence the scaling factor in cells thereby proving causality.

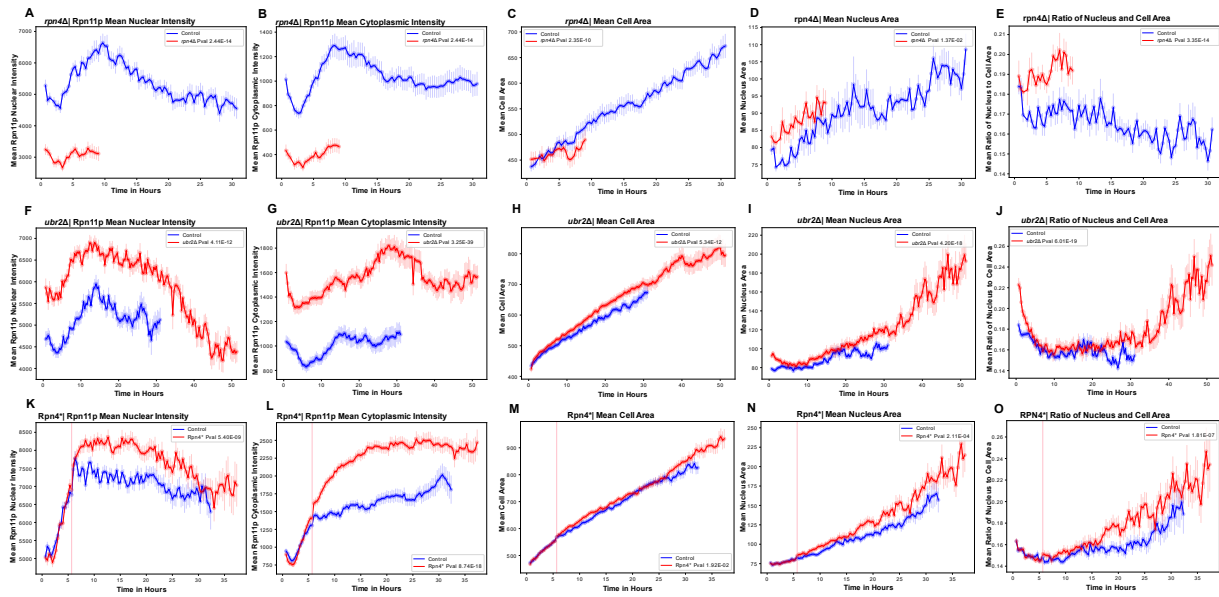


Fig 3.2. Proteasome perturbations influence the size scaling dynamics.

The graphs compare the different proteasome perturbations of *rpn4Δ*, *ubr2Δ*, and Rpn4* strains to the control. All strains have Cox4p-GFP tag and a Rpn11p-mCherry tag. The sequence of the graphs, from left to right, represents Rpn11p nuclear intensity, Rpn11p cytoplasmic intensity, cell area, nucleus area, and the ratio of the nucleus to cell area. The y-axis corresponds to the mean values depicted in the graph titles. The x-axis is the hours of live cells overtime. Time points with fewer than 15 live dividing cells are excluded from analysis. The red curves denote the mean values for the respective knockout strain, while the blue curves indicate the mean values for the control. (A-E) is the *rpn4Δ* in red (N=47, mean RLS=4.04) and in blue the control (N=47, mean RLS=11.21). (F-J), is the *ubr2Δ* in red (N=61, mean RLS=16.69) and in blue the control (N=46, mean RLS=13.24). (K-O), is the Rpn4* (N=103, mean RLS=13.31) in red which received 16nM of estradiol at 5.5 hours as designated by the pink vertical line. The blue curve is the control (N=107, mean RLS=13.72). The Rpn4* experiment is the aggregated data of two independent experiments. The P values are depicted in the graphs and are calculated using a Mann-Whitney U test. The shaded region signifies the SEM.

To confirm whether perturbation of Rpn4* increases Rpn11p activity and nucleus size, induction was performed at 19.2 hours (Fig. 3.3). Just as predicted, Rpn11p and the nucleus area increased.

However, whether the increase in nuclear area is due to the nuclear influx of Rpn11p proteins remained ambiguous. Targeting the nucleus transporter wasn't feasible due to broad protein impact. Thus, a Rpn11p mCherry with a SV40NLS tag was constructed. The estradiol construct was integrated into the genome in a strain background which had endogenous Rpn11p tagged with mCherry. Using the same fluorescent tag did not affect our GMM model in separating out regional intensities as the induced SV40NLS protein becomes significantly higher than the endogenous Rpn11p mCherry. Overexpressed Rpn11p-SV40NLS remained in the nucleus allowing us to observe whether nuclear size changes were due to the increasing Rpn11p influx. Despite no observable increase in nuclear size post-induction, there was a noticeable reduction in RLS and remaining buds (Fig. 3.4). This indicated that an increase in nuclear Rpn11p may not be beneficial to the cell. Furthermore, we did notice that there was an increase in the cytoplasmic Rpn11p level. This is likely the endogenous Rpn11p-mCherry, which may have been displaced due to the induced Rpn11p-SV40NLS protein. Attempts to solely increase Rpn11p led to difficulty in nucleus segmentation with no difference in lifespan or the number of buds left (supplemental).

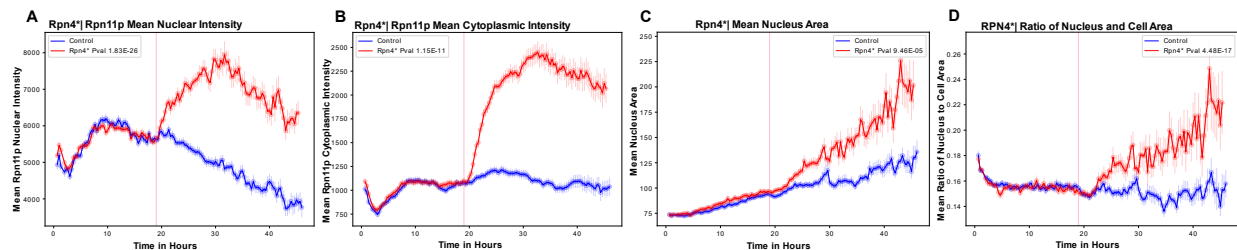


Fig 3.3. Temporally perturbing the proteasome at 19.2hrs increases the scaling dynamics.

The graphs display the Rpn11p intensity, and the nucleus organelle changes when Rpn4* is induced at a different time. The sequence of the graphs, from left to right, represents Rpn11p nuclear intensity, Rpn11p cytoplasmic intensity, nucleus area, and the ratio of the nucleus to cell area. The y-axis corresponds to the mean values depicted in the graph titles. The x-axis is the hours of live cells overtime. Time points with fewer than 15 live dividing cells are excluded from analysis. (A-D), is the Rpn4* (N=115, mean RLS=16.5) in red which received 16nM of estradiol at 19.2 hours as designated by the pink vertical line. The blue curve is the control (N=114, mean RLS=18.03). The control contains the Rpn4* construct with no estradiol. The experiment was performed twice, and the figures represent the cumulative data. The P values are depicted in the graphs and are calculated using a Mann-Whitney U test. The shaded region signifies the SEM.

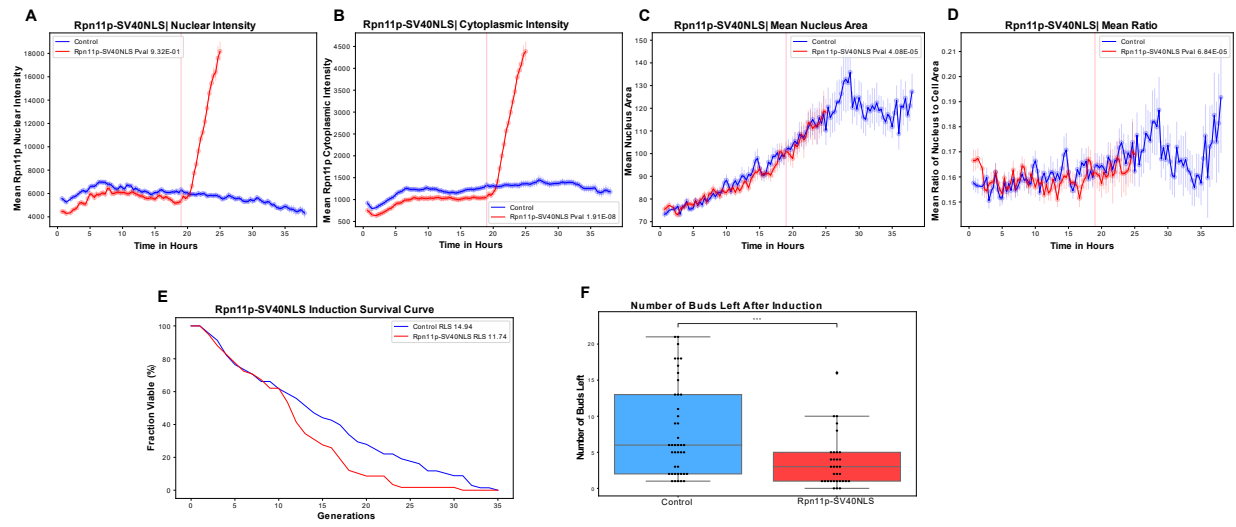


Fig 3.4. Nuclear size increase is not driven by nuclear influx of Rpn11p.

(A-D), display the Rpn11p intensity, and the nucleus organelle changes when Rpn11p-SV40NLS is induced at time 19.2 hours. The sequence of the graphs, from left to right, represents Rpn11p nuclear intensity, Rpn11p cytoplasmic intensity, nucleus area, and the ratio of the nucleus to cell area. The x-axis is the hours of live cells overtime. Time points with fewer than 15 live dividing cells are excluded from analysis. The Rpn11p-SV40NLS (N=33, mean RLS=11.74) is in red and received 16nM of estradiol at 19.2 hours as designated by the pink vertical line. The blue curve is the control (N=42, mean RLS=14.94). The control contains the Rpn11p-SV40NLS construct with no estradiol. The P values are depicted in the graphs and are calculated using a Mann-Whitney U test. The shaded region signifies the standard error mean. (E), is a survival curve with the number of generations on the x-axis and the fraction viable on the y-axis. (F), is the number of buds left after media is switched with or without estradiol. The P value is calculated using Man-Whitney U test and is 5.083e-04.

Given the relationship between the proteasome and nucleus size, we investigated differences in proteasome activity in *fov1Δ*, *sgf73Δ*, and *dnm1Δ* mutants. Some of these mutants have been noted to also affect the scaling of certain organelles^{35,52}. The *fov1Δ* reduces rDNA accumulation, rDNA increases towards the end of a cell's lifespan, which impacts nucleus area⁵². In *fov1Δ* cells, nucleus area did not exhibit a significant increase at the end of the lifespan, thus affecting the scaling ratio (Fig 3.5C-E). Notably, Rpn11p levels in both nuclear and cytoplasmic compartments is higher in *fov1Δ* cells (Fig 3.5A-B). This supports the idea that rDNA can influence proteasome proteins¹⁷. However, the absence of elevated scaling ratio, nucleus, and cell area in *fov1Δ* cells suggests that proteasome activity is not the exclusive determinant of the scaling ratio. Gene deletions affecting cell growth have previously been established to affect the cell and nucleus area³⁵. We identified *sgf73Δ* to influence the nucleus and scaling

ratio (Fig 3.5H-J). Interestingly, we found *sgf73Δ* to also influence Rpn11p dynamics as the nuclear and cytoplasmic intensity seemed to be lower and more constant overtime (Fig 3.5F-G). This could suggest proteasomal decline is due to increasing protein translation. Perhaps the increase in protein translation drives the scaling size, which in turn dilutes the proteasome level. Interestingly, the constant proteasome observed in the *sgf73Δ* coincided with a steady scaling ratio (Fig 3.5F-G). Dnm1 is a dynamin related GTPase and has a role in mitochondrial fission. The knockout affects mitochondrial morphology and leads to aggregate mitochondrial structures⁵³. The *dnm1Δ* did not seem to change the dynamic of Rpn11p, however, cells towards the end of life had an increasing nucleus area and nucleus to cell area ratio (Fig 3.5N-O). The *dnm1Δ* also led to an initial increase in the cytoplasmic Rpn11p levels (Fig 3.5K-L). Overall, it appears that *dnm1Δ* had little influence on proteasome activity and scaling, suggesting that perhaps mitochondrial morphology may be more specific to the mitochondria changes.

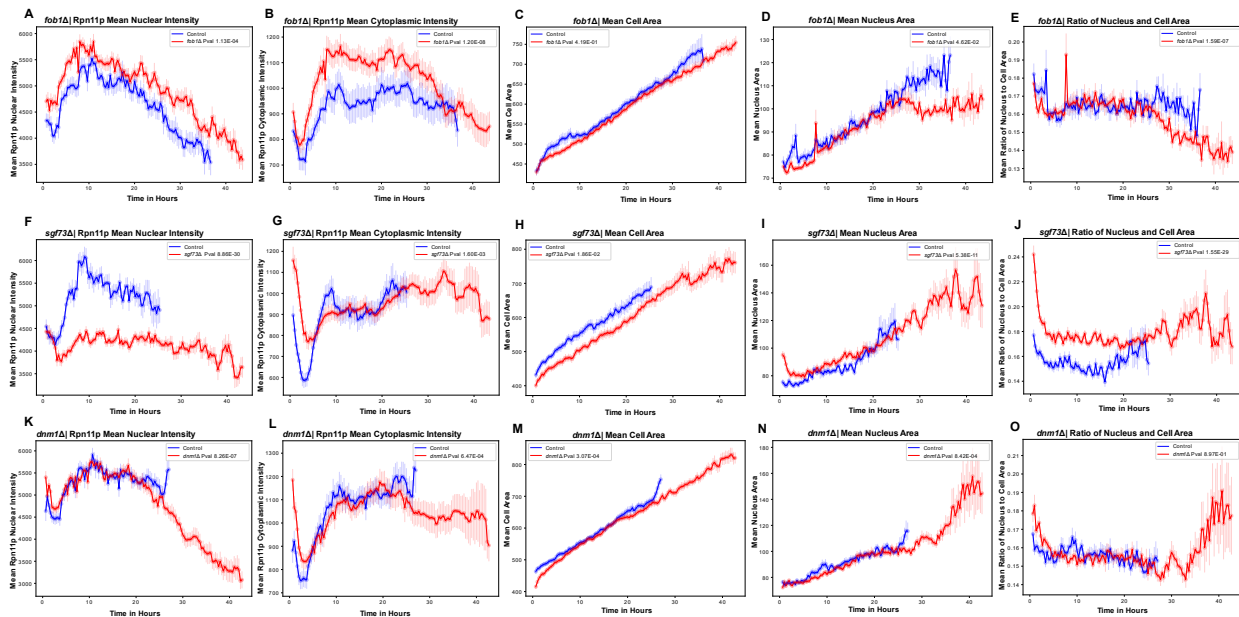


Fig 3.5. *fob1Δ*, *sgf73Δ*, and *dnm1Δ* display different scaling dynamics.

The graphs compare the different *fob1Δ*, *sgf73Δ*, and *dnm1Δ* strains to the control. All strains have a Cox4p-GFP tag and a Rpn11p-mCherry tag. The sequence of the graphs, from left to right, represents Rpn11p nuclear intensity, Rpn11p cytoplasmic intensity, cell area, nucleus area, and the ratio of the nucleus to cell area. The y-axis corresponds to the mean values depicted in the graph titles. The x-axis is the hours of live cells overtime. Time points with fewer than 15 live dividing cells are excluded from analysis. The red curves denote the mean values for the respective knockout strain, while the blue curves indicate the mean values for the control. (Figure caption continued on the next page).

(Figure caption continued from the previous page). (A-E) is the *fov1Δ* in red (N=67, mean RLS=16.75) and in blue the control (N=50, mean RLS 14.6). (F-J), is the *sgf73Δ* in red (N = 73, mean RLS=16.52) and in blue the control (N=56, mean RLS=10.41). (K-O), is the *dnm1Δ* (N=89, mean RLS=13.66) in red and in blue the control (N=63, mean RLS=12.619). The P values are depicted in the graphs and are calculated using a Mann-Whitney U test. The shaded region signifies the SEM.

We next sought to aggregate our knockout experiments and separate the aging dynamics based on short-lived vs long-lived cells (Fig 3.6.1). We observed the *fov1Δ* to have a lower scaling ratio in the long-lived cells when compared to the short-lived cells. Additionally, the cytoplasmic Rpn1 Ip levels are higher in short-lived cells when compared to long-lived cells (Fig 3.6.1). Regardless of the knockouts performed, we found that when cells are segregated into long-lived and short-lived, the differences between the two trajectories are comparable. In all cases the short-lived cells had an increasing organelle size scaling when compared to the long-lived cells (Fig 3.6.1 and Fig 3.6.2). Furthermore, the levels of Rpn1 Ip in short-lived cells is higher than the long-lived cells for all different knockouts (Fig 3.6.1 and Fig 3.6.2).

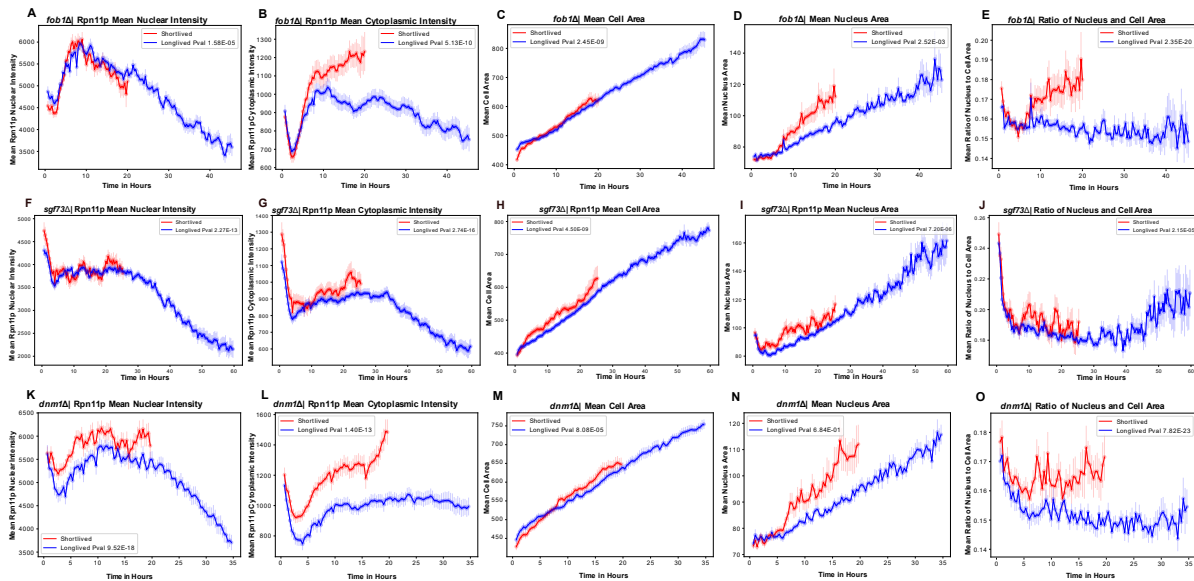


Fig 3.6.1. *fov1Δ*, *sgf73Δ*, and *dnm1Δ* separated by lifespan display similar dynamic trajectories.

The graphs display the *fov1Δ*, *sgf73Δ*, and *dnm1Δ* strains segregated into long-lived vs short-lived cells. The sequence of the graphs, from left to right, represents Rpn1 Ip nuclear intensity, Rpn1 Ip cytoplasmic intensity, cell area, nucleus area, and the ratio of the nucleus to cell area. The y-axis corresponds to the mean values depicted in the graph titles. The x-axis is the hours of live cells overtime. Time points with fewer than 25 live dividing cells are excluded. The red curves denote the mean values for short-lived cells with an RLS of less than 15, while the blue curves indicate the mean values for long-lived cells with an RLS of 15 or more. (Figure caption continued on the next page).

(Figure caption continued from the previous page). (A-E) is the *fab1Δ* (N=163, mean RLS=15.5), comparing short-lived (N=77, mean RLS=8.57) and long-lived cells (N=89, mean RLS=22.03). (F-J), is the *sgf73Δ* (N=168, mean RLS=17.20), comparing short-lived (N=53, mean RLS=9.51) and long-lived cells (N=115, mean RLS=20.74). (K-O), is the *dnm1Δ* (N=137, mean RLS=12.29), comparing short-lived (N=81, mean RLS = 7.80) and long-lived cells (N=56, mean RLS=18.79). The P values are depicted in the graphs and are calculated using a Mann-Whitney U test. The shaded region signifies the SEM. All graphs display the aggregation of two experiments.

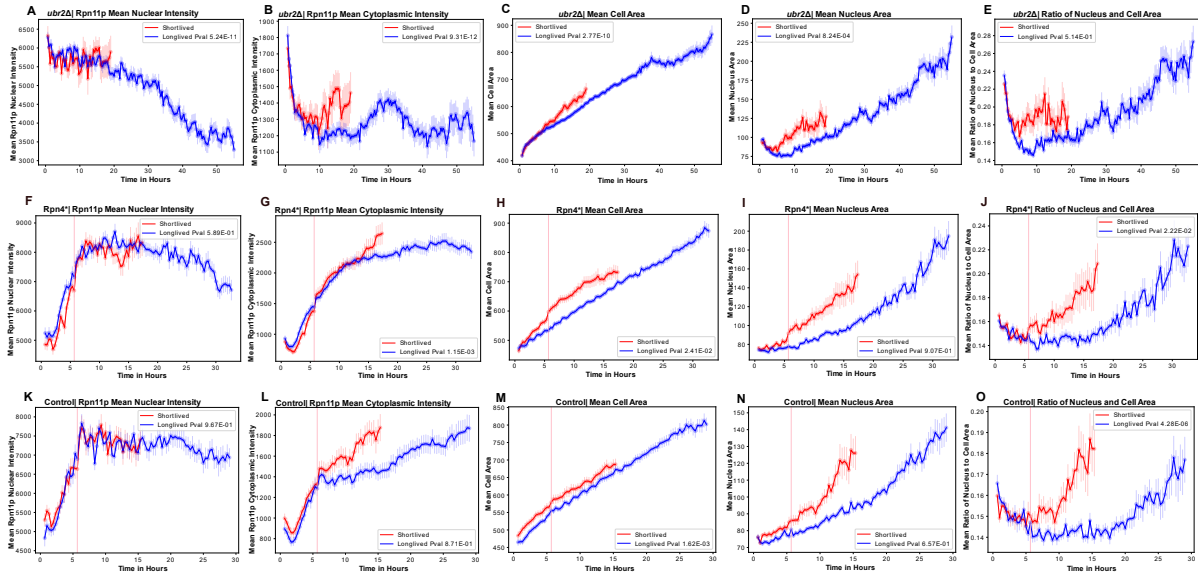


Fig 3.6.2. Overexpression of proteasome separated by lifespan maintains rapidly increasing organelle size.

The graphs display the *ubr2Δ* and Rpn4* segregated into long-lived vs short-lived cells. The sequence of the graphs, from left to right, represents Rpn11p nuclear intensity, Rpn11p cytoplasmic intensity, cell area, nucleus area, and the ratio of the nucleus to cell area. The y-axis corresponds to the mean values depicted in the graph titles. The x-axis is the hours of live cells overtime. Time points with fewer than 25 live dividing cells are excluded. The red curves denote the mean values for short-lived cells with an RLS of less than 15, while the blue curves indicate the mean values for long-lived cells with an RLS of 15 or more. (A-E) is the *ubr2Δ* (N=167, mean RLS=17.86), comparing short-lived (N=50, mean RLS=8.24) and long-lived cells (N=117, mean RLS=22). (F-J), is the Rpn4* receiving 16nM of Estradiol at time 5.5 hours (N=102, mean RLS=13.41), comparing short-lived (N=55, mean RLS=8.42) and long-lived cells (N=47, mean RLS=19.19). (K-O), is the Rpn4* control which did not receive estradiol (N=106, mean RLS=13.82), comparing short-lived (N=52, mean RLS = 8.71) and long-lived cells (N=54, mean RLS=18.74). The P values are depicted in the graphs and are calculated using a Mann-Whitney U test. The shaded region signifies the standard error of the mean. All graphs display the aggregation of two experiments.

When comparing how the different genetic perturbations influenced lifespan, we confirmed lifespan extension in all our long-lived mutants except for *dnm1Δ* (Fig 3.7.1). The combined stress of imaging cells every 20 minutes with protein tags may be too stressful for the *dnm1Δ*. Additionally, variations in lifespan measurement techniques might lead to inconsistencies in RLS. Specifically, employing micromanipulation on petri dishes versus using microfluidic devices with liquid media could result in

different RLS outcomes¹¹. To our knowledge, this is the first time *dnm1Δ* has been screened on a microfluidic device with lifespan measurements displayed. Furthermore, we also confirmed that Rpn4* did not increase lifespan as well^{24,25} (Fig 3.7.1). This could be because of specific downstream targets of Rpn4* that are not beneficial to lifespan.^{24,25} Our growth rate curves indicate that some of these mutants affect the growth rate of cells. This was the case for Rpn4* induction, *rpn4Δ*, and *sgf73Δ* (Fig 3.7.2). Additionally, we also confirmed our proteostasis activity and found that Rpn4* increases activity almost as high as *ubr2Δ* (Fig. 3.8).

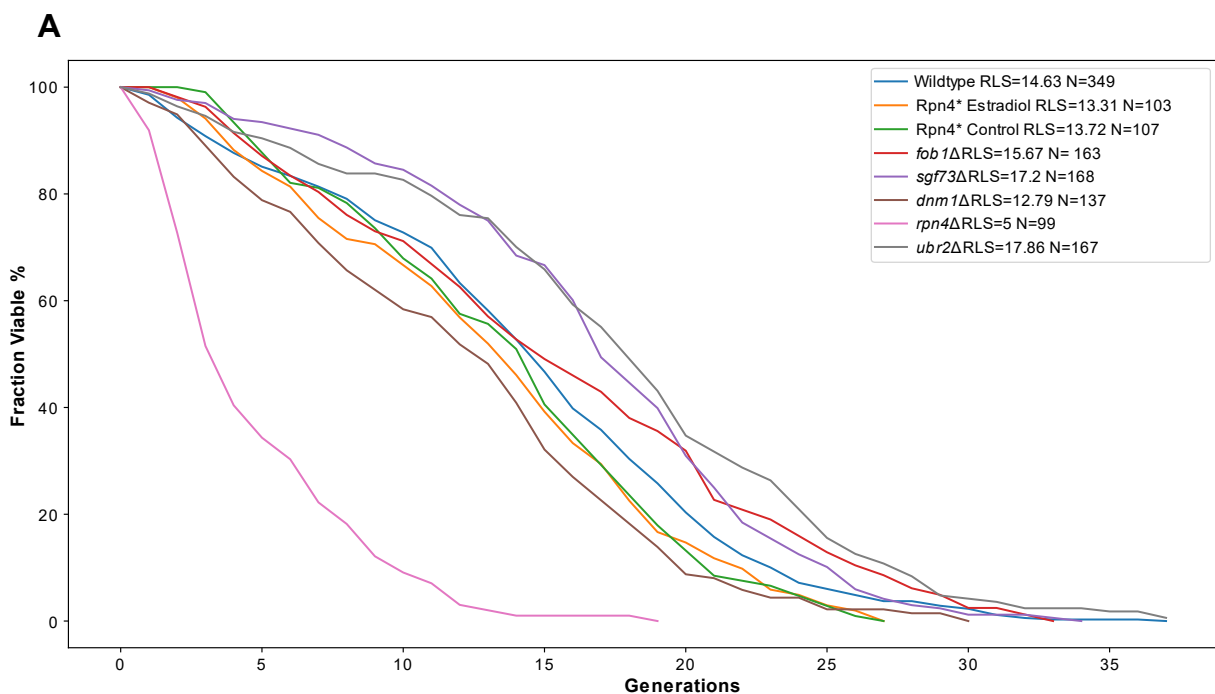


Fig 3.7.1. Survival curve of different constructs.

(A) is the survival curves for the different constructs. All strains have the Cox4p-GFP and Rpn1 1p-mCherry tag. Each strain was acquired independently at least two times and aggregated together. The Rpn4* strain is treated with either estradiol at 5.5hours or regular YEPD media.

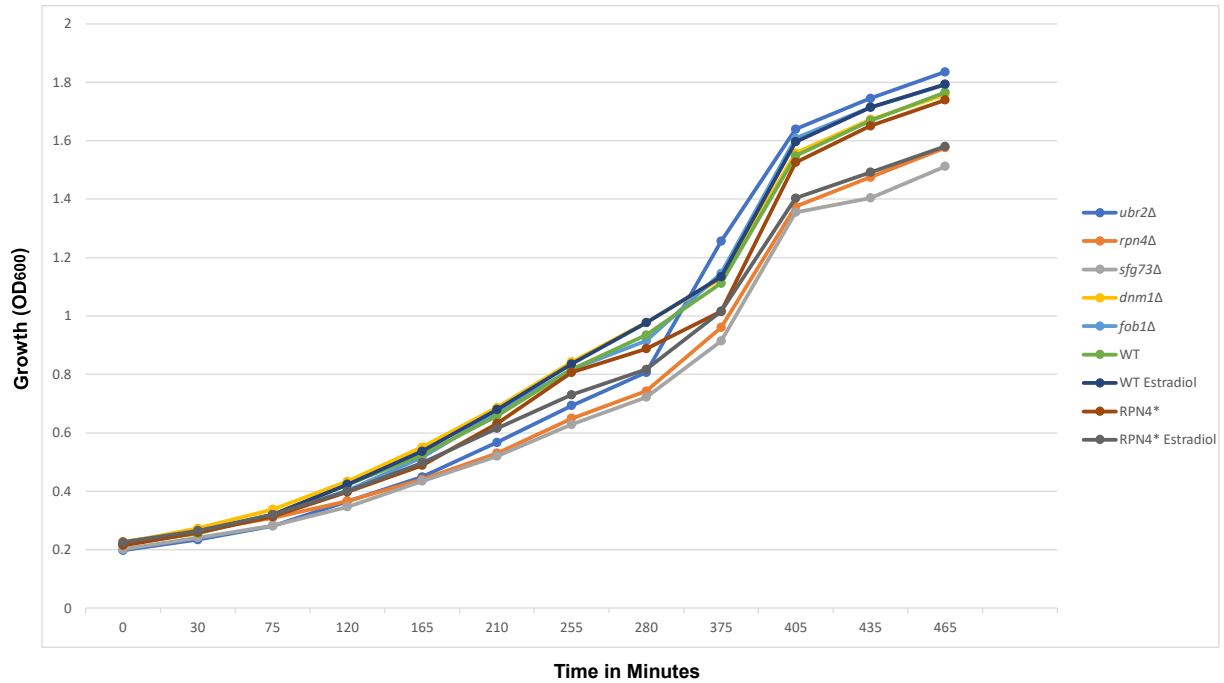
A

Fig 3.7.2. Growth curve of different constructs.

Growth measurements of *ubr2Δ*, *rpn4Δ*, *sfg73Δ*, *dnm1Δ*, *fob1Δ*, WT, WT estradiol, Rpn4*, and Rpn4* estradiol. Overnight cultures were diluted to an OD₆₀₀ of ~0.2 in galactose rich media and grown near stationary phase. Cell density (OD₆₀₀) was measured at intervals as indicated and used to plot the growth curves. Samples given 16nM of estradiol were incubated during the start of the experiment.

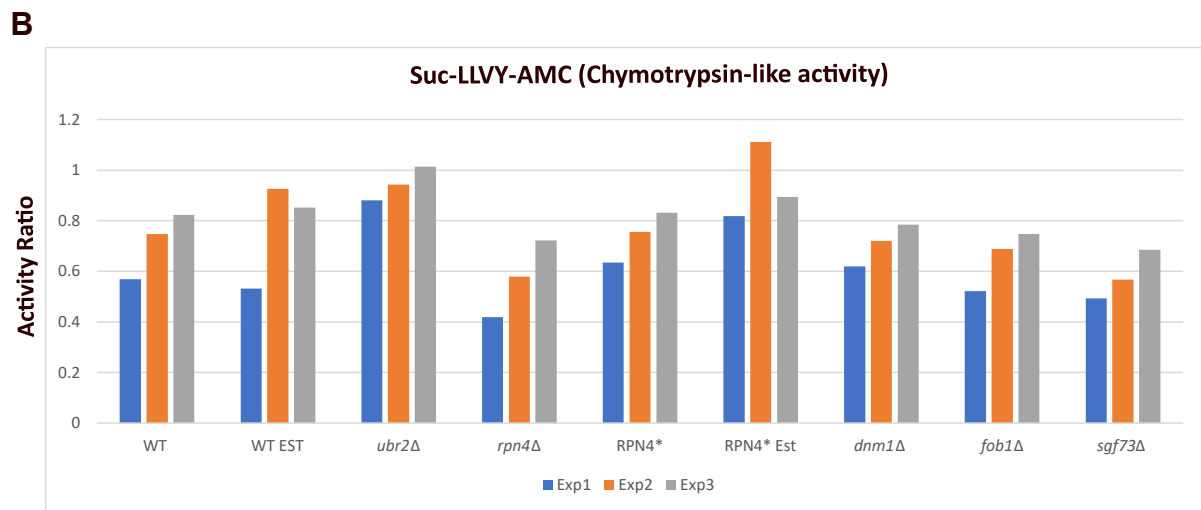
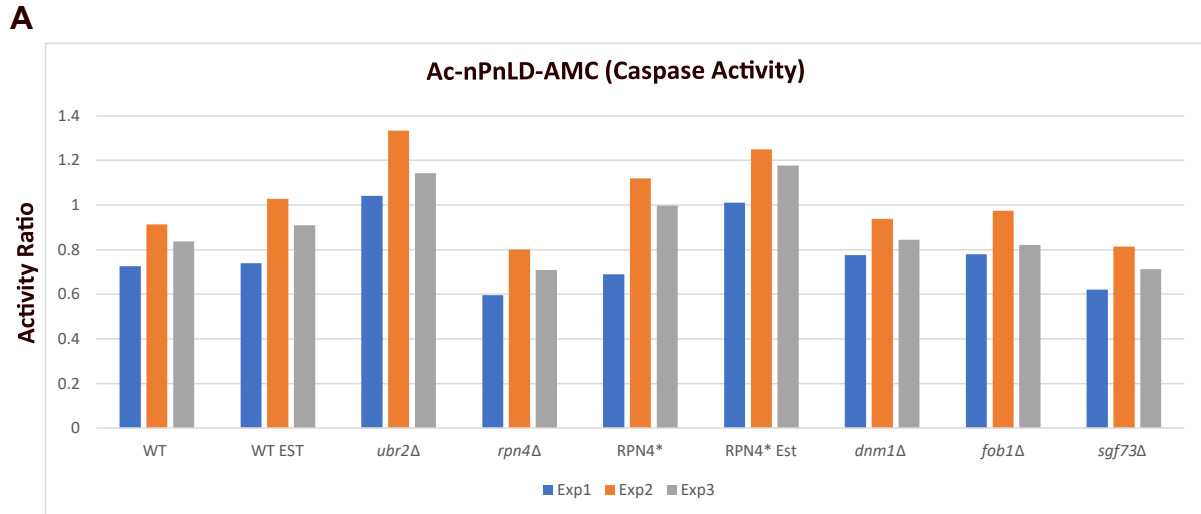


Fig 3.8. Measuring proteasome activity in different perturbation strains.

(A-B) Elevated cellular proteasomal peptidase activity in wildtype (WT), WT estradiol, *ubr2*Δ, *rpn4*Δ, Rpn4*, Rpn4* estradiol, *dnm1*Δ, *fob1*Δ, and *sgf73*Δ. Samples given 16nM of estradiol were incubated for ~14 hours with estradiol before harvesting. All samples were collected at an OD₆₀₀ of .8-1. Strains were tested with 50 μg of total protein in the presence of 100 μM of the fluorogenic substrates Ac-nLPnLD-AMC (caspase activity) and Suc-LLVY-AMC (chymotrypsin-like activity) in three independent experiments. The activity ratio is calculated using reactions with and without 50 μg/ml of the proteasome inhibitor MG132 to demonstrate specificity of the reactions.

DISCUSSION

The intricate interplay between organelle scaling and protein levels remains a focal point of research. Using the non-linear Granger causality method, we identified the proteosome as a potential determinant of nucleus size (Fig 3.1). This was corroborated when alterations in the proteosome led to increased nucleus size (Fig 3.2 and Fig 3.3). Importantly, the nucleus size increase was not attributed to the influx of Rpn11p into the nucleus (Fig 3.4). This raises the possibility that the active proteosome plays a role in nucleus size scaling, perhaps by optimizing nuclear transport. Intriguingly, a majority of long-lived mutants, including those with proteosome alterations, exhibited changes in organelle scaling (Fig 3.5 and Fig 3.2). This could hint at a shared longevity mechanism. Yet, while Rpn4* influenced both nucleus and organelle size, it did not enhance lifespan (Fig 3.7.1). The potential accumulation of harmful proteosome proteins might offset the benefits of such scaling. In summary, we identify the proteosome as a modulator of organelle scaling. Nevertheless, the relationship between nucleus size and the proteosome remains ambiguous. Our data indicate that, despite an increase in the proteosome, there is a concomitant decline in nuclear Rpn11p levels as the nucleus area expands (Fig 3.2 and Fig 3.3). Establishing a direct causative link proves challenging due to the absence of methods to exclusively perturb scaling. While we attempted to pinpoint the scaling effect using knockout experiments, their intrinsic effects on major pathways confounds proper data interpretation.

CHAPTER 3: The proteasome and size scaling predicts and may drive aging hallmarks.

ABSTRACT

Previously, studies have suggested that the loss of vacuole acidity affects mitochondrial morphology^{15,16}. This causal relationship supports a linear cascade model in which changes in the functionality of one organelle can lead to changes in another. To determine whether proteasome perturbation could affect mitochondrial morphology, we perturbed the proteasome and compared the trajectory of phenotypic changes across various genetic perturbations. We found that both mitochondrial phenotype and activity responded to proteasome changes. Our data suggest that the mitochondria may respond to changes in proteasomal activity, but not vice versa. Interestingly, we also identified strong predictive characteristics of Rpn11p levels and proteostasis stress. Overall, our findings indicate that the proteasome is a key predictor and possible driver of aging hallmarks.

RESULTS

To perform a high-throughput classification, an artificial intelligence (AI) ResNet50 model was trained to identify seven cellular phenotypes⁵⁴ (Fig. 4.1). Increasing proteasome activity by *ubr2Δ* and temporal overexpression of Rpn4* lead to an increase in the unclassified mitochondrial phenotype called other (Fig. 4.2B, E, F). Alternatively, the reduction of the proteasome by *rpn4Δ* led to a drastic reduction in every phenotype except for the circular phenotype (Fig. 4.2C). The loss of the proteasome activity has been tied to affecting mitochondrial activity⁵⁵. In our analysis we observed a rise in the circular phenotype for the *rpn4Δ*; however, whether the circular phenotype is indicative of an overworked mitochondria remains to be seen. Overall, our data suggests that proteasome perturbation influences the mitochondrial morphology.

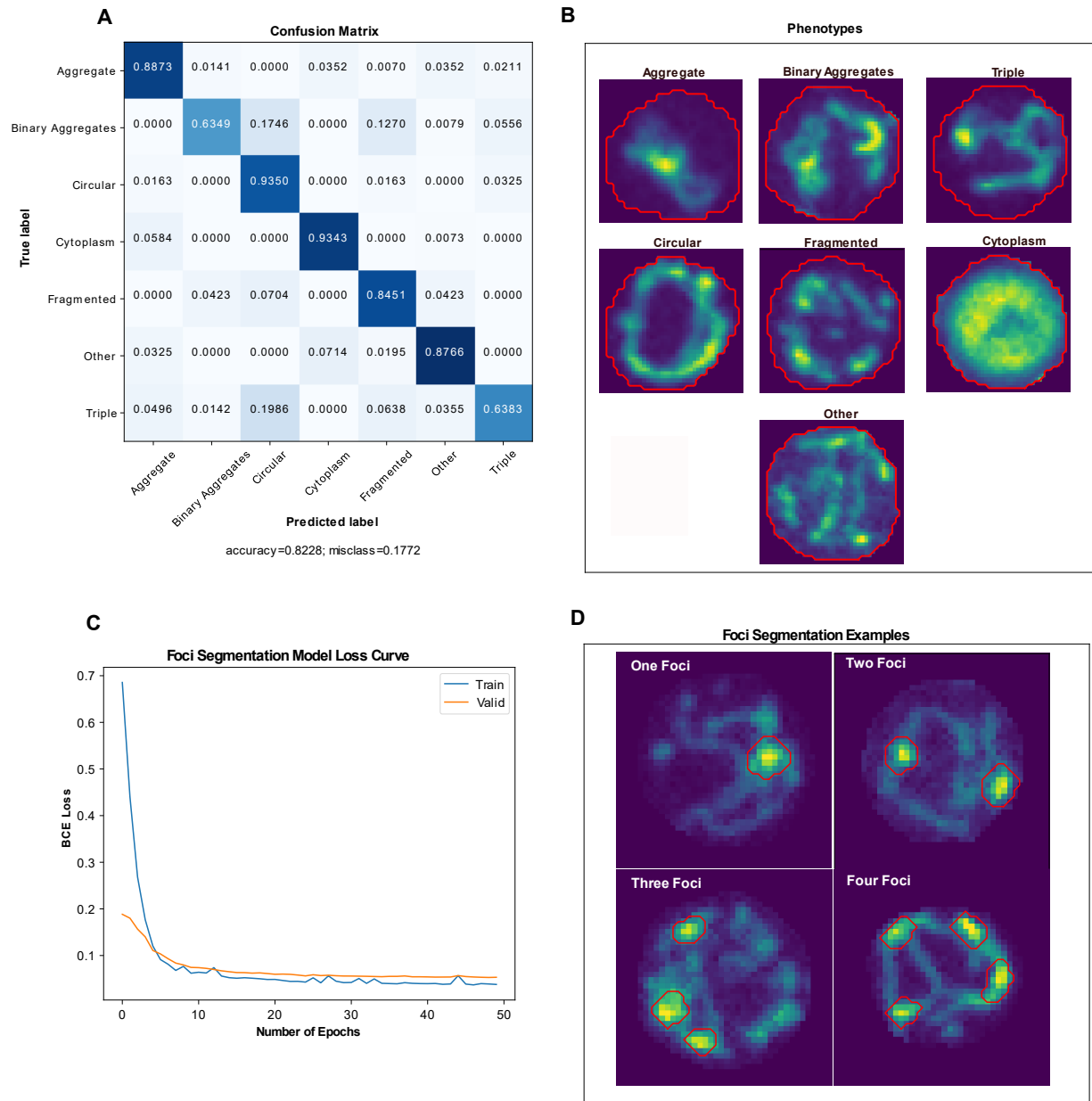


Fig 4.1. Classifying phenotypes and segmenting foci with AI.

(A), Represents a confusion matrix of the ResNet50 model predictions for the validation dataset, with true labels on the y-axis and predicted labels on the x-axis. The validation dataset encompasses diverse experiments, integrating different protein organelle tags and knockout experiments. (B), Exhibits a representative image of identified phenotypes. The red circle delineates the cell boarder. (C-D), Relate to the Foci Segmentation Model. (C), the loss curve is presented, with the training data depicted by the blue curve and the validation data by the orange curve. The y-axis signifies the Binary Cross-Entropy with Logits Loss (BCE), while the x-axis denotes the number of epochs. (D), depicts a selection of mitochondrial phenotypes with foci highlighted in red. The foci count per cell is outlined in white, ranging from one to four. The model can detect up to four or more foci.

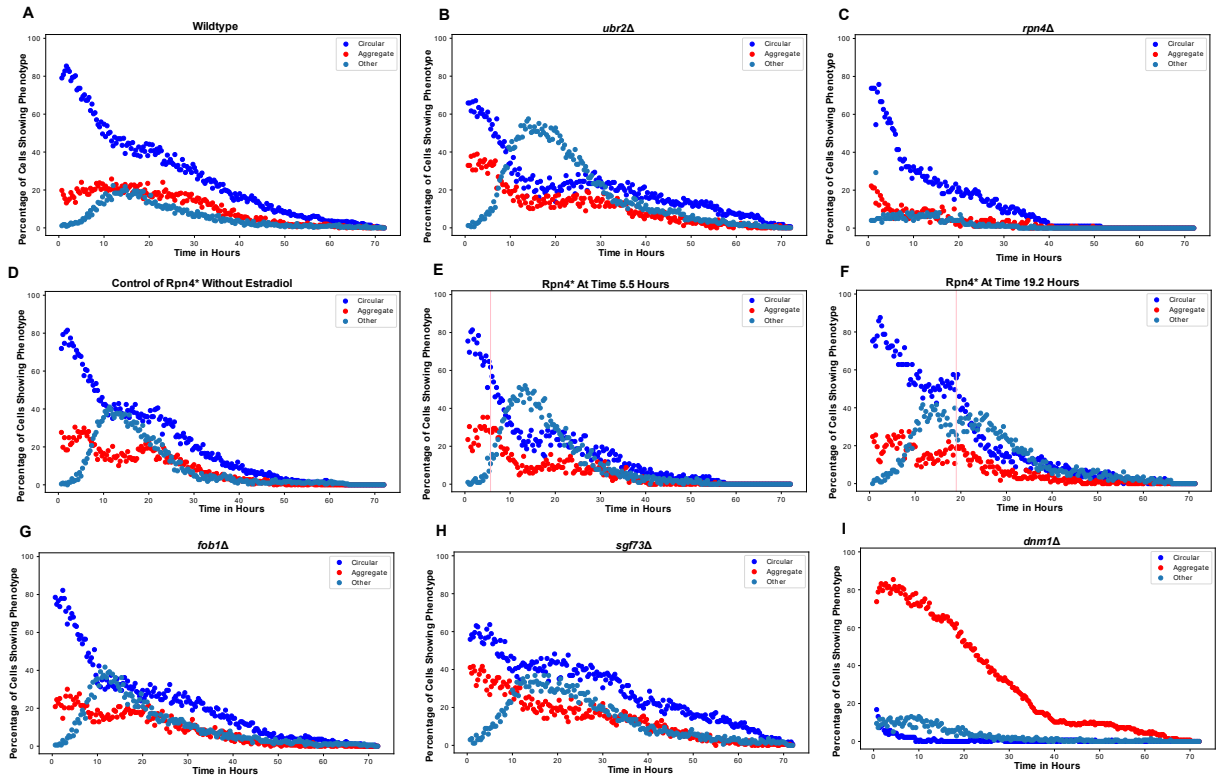


Fig 4.2. Proteasome perturbation affects mitochondria morphology.

The eight graphs represent the percentage of live cells at each time displaying either the circular, aggregate, or other phenotype. The x-axis is the time in hours of live cells and the y-axis is the percentage of cells alive displaying a particular phenotype. The following graphs are for Wildtype (N=343), *ubr2Δ* (N=167), *rpn4Δ* (N=99), Rpn4* without Estradiol (N=221), Rpn4* induction at 5.5hours (N=103), Rpn4* induction at 19.2hours (N=115), *fob1Δ* (N=163), *sfg73Δ* (N=168), and *dnm1Δ* (N=137). The pink vertical line indicates when the estradiol system was induced. The perturbation experiments are the accumulation of two experiments performed independently. The wildtype and Rpn4* without estradiol are the accumulation of the controls during the induction experiments.

Furthermore, since the proteasome impacted the mitochondria morphology but not the other way around, we wanted to determine the relation between mitochondrial morphology and mitochondrial activity (Fig. 4.2 and Chapter 2 Fig 3.5). The *dnm1Δ* influences mitochondrial morphology by preventing mitochondrial fission, thereby leading to mitochondrial aggregates. Likewise, *dnm1Δ* leads to cells predominantly staying in the aggregate state⁵³ (Fig. 4.2I). Observing our *dnm1Δ* Cox4p levels, we ascertained whether mitochondrial morphology influenced Cox4p activity and the area of the inner mitochondria. The Cox4p mitochondrial intensity level was significantly higher in the *dnm1Δ*, and the

trajectory was also altered, suggesting that mitochondrial morphology influences mitochondrial activity rather than nucleus area or proteasome (Fig. 4.3.1 and Chapter 2 Fig. 1.5).

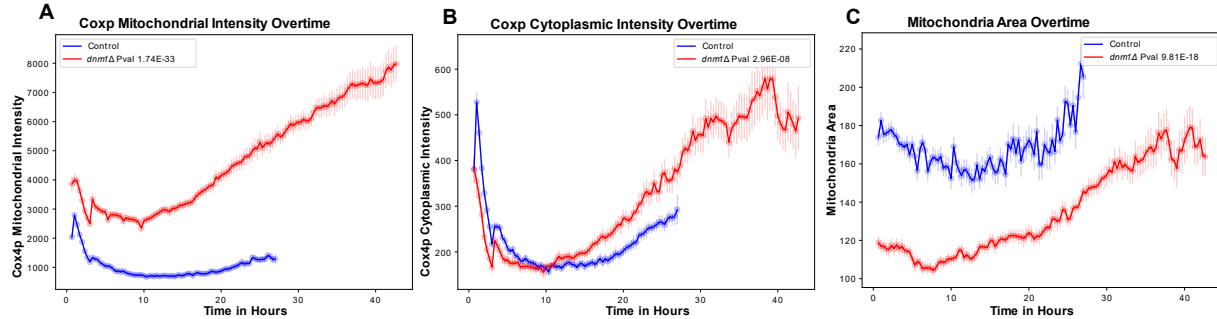


Fig 4.3.1. Perturbing mitochondrial morphology influences Cox4p and mitochondrial area.

(A-C), displays the control in blue (n= 63) and the *dnm1Δ* in red (n= 89). The x-axis is the time in hours of live dividing cells with a minimum of 15 cells being used. A Mann-Whitney U test is calculated between the control and knockout curves with respective P values of 1.74E-33, 2.96E-08, and 9.81E-18. GMM is used to separate out regions of intensity for the Cox4p protein. (A), displays the mean Cox4p mitochondrial intensity calculated from dividing cells for each timepoint. (B), displays the mean Cox4p cytoplasmic intensity calculated from dividing cells for each timepoint. (C), displays the mean inner mitochondrial area calculated from dividing cells for each timepoint. Sharded areas represent the standard errors of mean between cells.

Since proteasomal perturbations could influence mitochondrial morphology, we sought to determine whether proteasomal perturbations could also affect mitochondrial activity. Our non-linear Granger causality method suggested that Rpn11p levels are casual to Cox4p (Fig. 4.3.2). The causality is validated by perturbing the proteasome. The proteasome loss directly influenced the mitochondrial activity and area. The *rpn4Δ* had higher levels of Cox4p intensity overtime (Fig. 4.4.1A-C). Interestingly, when Rpn4* was temporally increased, at times 5.5hrs and 19.2 hours, the Cox4p intensity decreased (Fig. 4.4.1 G-L). The notable decrease was not observed in the *ubr2Δ*, indicating that the mitochondrial response is Rpn4 specific as Ubr2 can influence various proteins including the Mig1p (Fig. 4.4.1D-F). The timing of Rpn4* induction influenced the strength of response, where a later perturbation led to a substantially larger change in Cox4p intensity (Fig. 4.4.1). On the other hand, Cox4p induction did not affect either the Rpn11p intensity or the organelle scaling dynamics (Fig. 4.4.2). Additionally, the foci

area and intensity were higher in *rpn4Δ* (Fig 4.5). Overexpression of the proteasome leads to no major significant changes in the foci Cox4p intensity or foci mitochondrial area (Fig. 4.5).

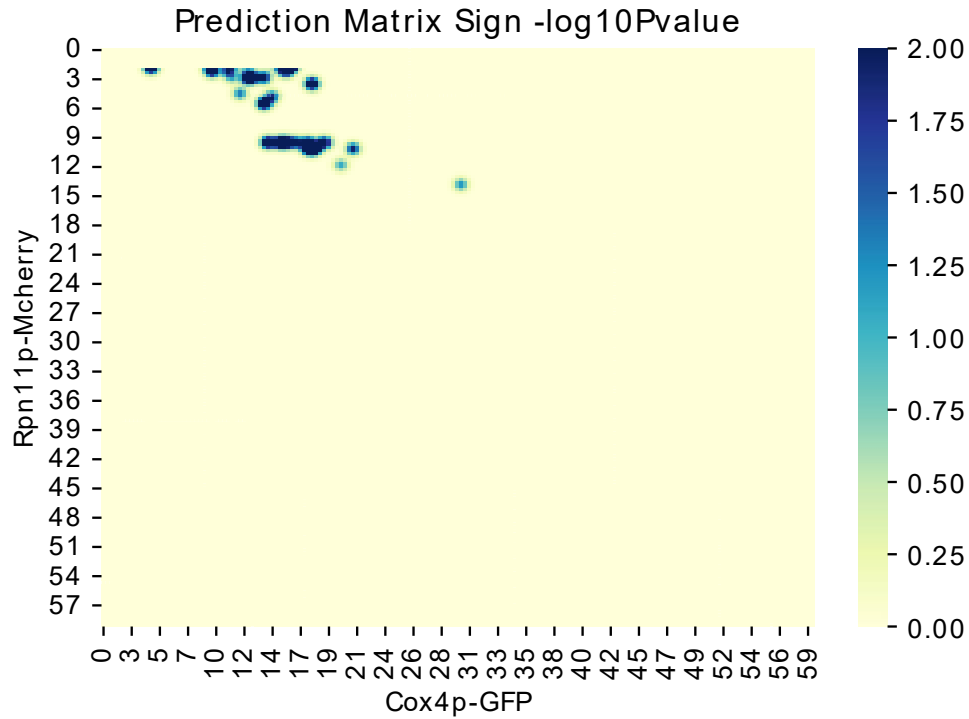


Fig 4.3.2. Granger causality reveals that Rpn11p intensity is causal to Cox4p intensity.

Predicting temporal order using Granger causality with decision trees. The heatmap presented displays the $-\log_{10} P$ values, calculated from an F-test. The y-axis utilizes Rpn11p intensity to predict subsequent Cox4p levels represented on the x-axis. Time points for both the y-axis and x-axis indicate the hours for the respective variables. The dataset consolidates our Cox4p-GFP and Rpn11p-mCherry strains from six independent experiments, encompassing 343 cells. Time points with fewer than 56 dividing cells have been excluded.

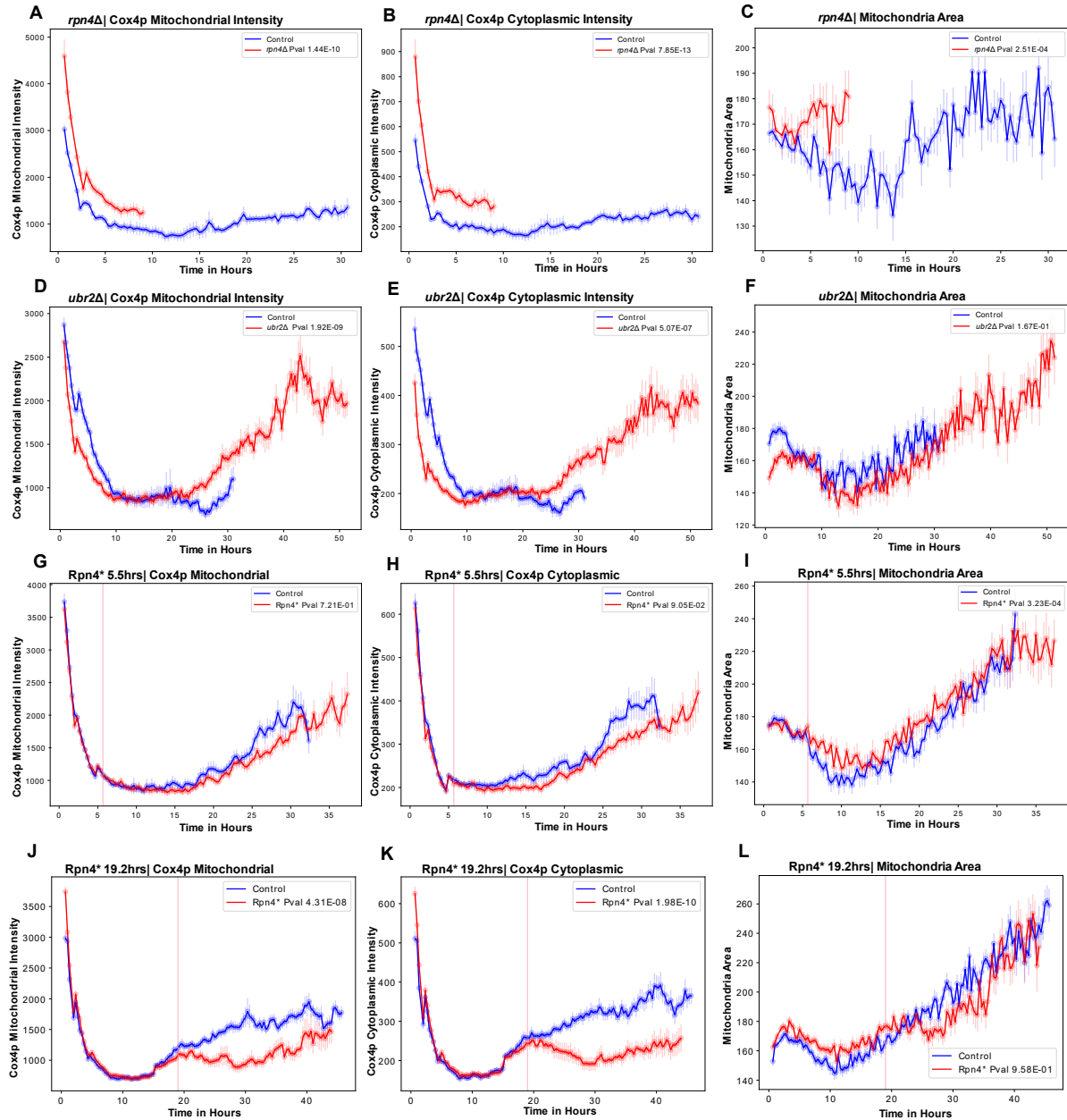


Fig 4.4.1. Mitochondrial activity responds to proteasomal perturbations.

The graphs above display the different proteasome perturbations of *rpn4Δ*, *ubr2Δ*, and temporal induction of Rpn4* at time 5.5hrs and 19.2hrs. The x-axis is time in hours of live cells with a minimum of 15 cells used. The Blue curves represent the control, and the red curves represent the proteasome perturbation. SEM is displayed in the shaded areas within the curves. (A-C), is the *rpn4Δ* (N= 47) vs the control (N= 47). (A), y-axis is the mean Cox4p mitochondrial intensity of live dividing cells. (B), y-axis is the mean Cox4p cytoplasmic intensity of live dividing cells. (C), y-axis is the mean inner mitochondrial area of live dividing cells. (D-F), is the *ubr2Δ* (N=61) vs the control (N= 46) with corresponding y-axis to (A-C). (G-I), is the Rpn4* induction (N=103) at time 5.5 hours vs the control with the same construct but without estradiol (N=107). (J-L) is the Rpn4* induction (N=115) at time 19.2 hours. (Figure caption continued on the next page).

(Figure caption continued from the previous page). The control (N=114) represents the same construct but without estradiol. The pink line indicates when induction occurs. Both Rpn4* experiments were performed twice, and the data represents the accumulation of the separate experiments.

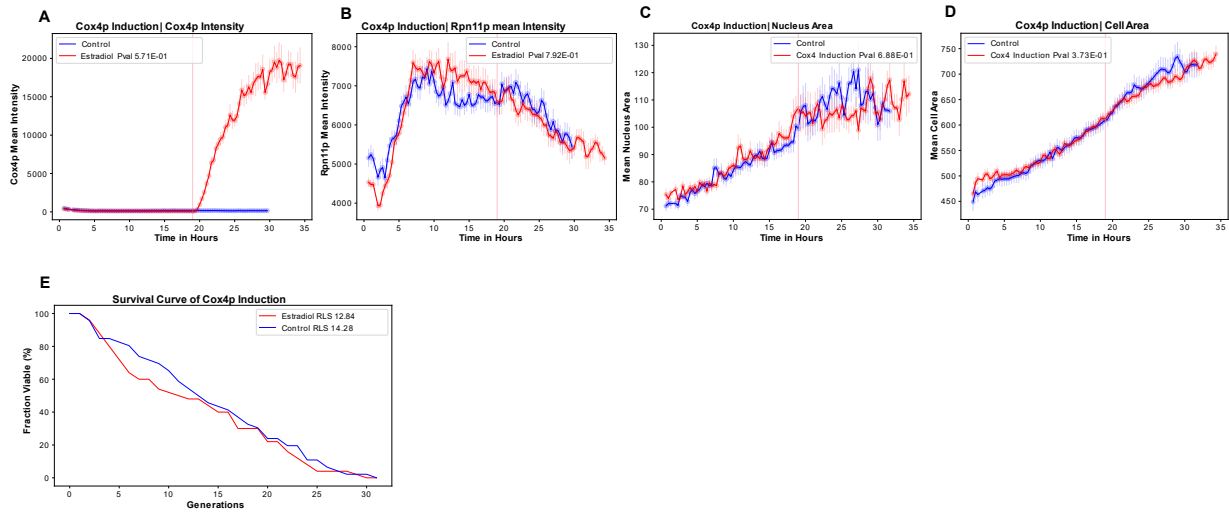


Fig 4.4.2. Cox4p overexpression does not impact Rpn11p or organelle scaling.

The graphs depict Cox4p-GFP temporal overexpression in a Rpn11p-mCherry strain. The blue curve represents the control (N=30, mean RLS=14.28), while the red curve corresponds to the Cox4p estradiol system induced with 16nM of estradiol (N=32, mean RLS=12.84). The pink line marks the 19.2hrs when media was replaced, either with or without estradiol, to initiate Cox4p induction. (A) shows mean Cox4p intensity, (B) displays Rpn11p mean intensity, (C) represents the average nucleus area, and (D) depicts the average cell area. The x-axis measures time in hours for live dividing cells, excluding time points with fewer than 15 dividing cells. (E) illustrates the survival curve.

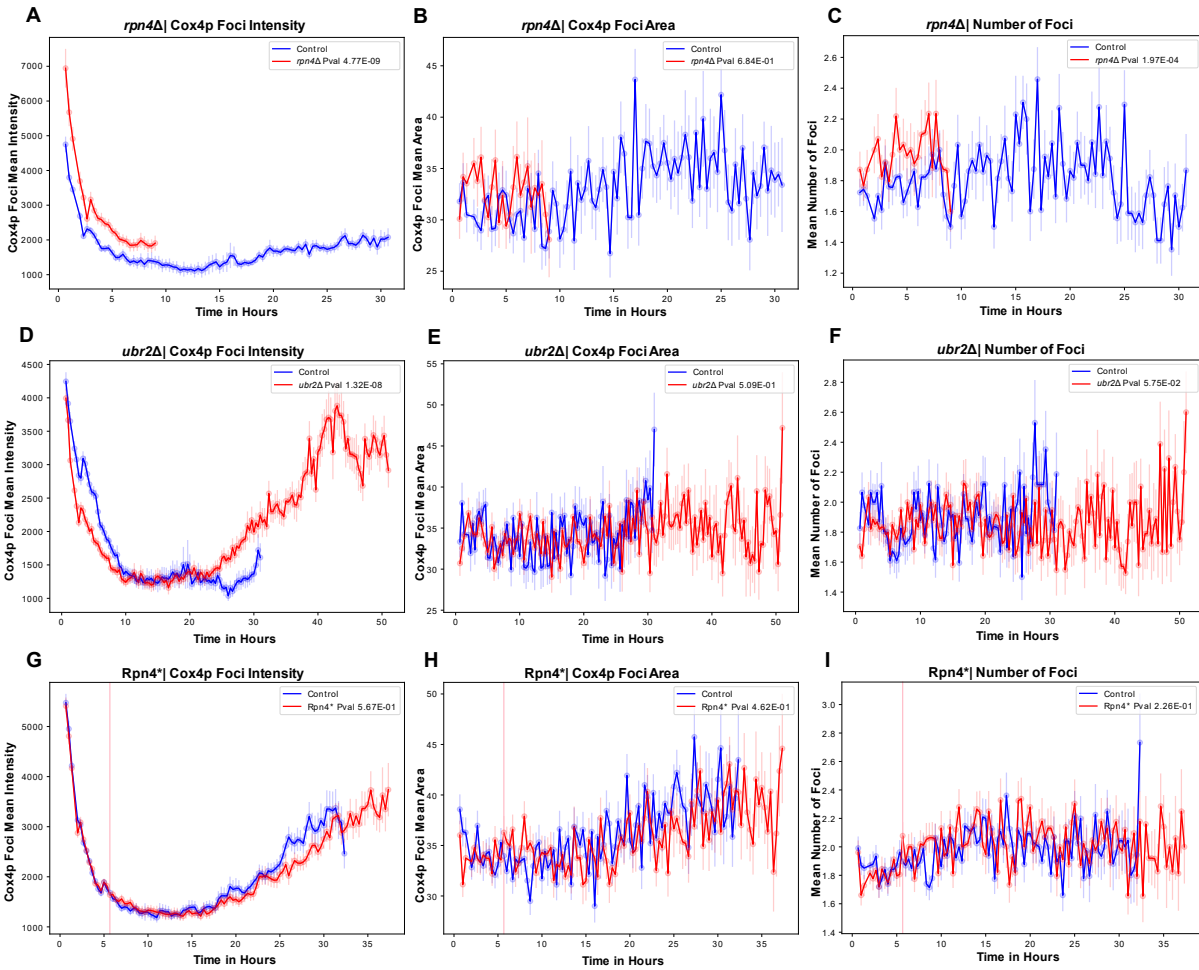


Fig 4.5. Loss of proteasome activity increases mitochondrial foci activity and size.

The graphs above display the foci changes in the mitochondria during different proteasome perturbations of *rpn4Δ*, *ubr2Δ*, and temporal induction of Rpn4* at time 5.5hrs. The x-axis is time in hours of live cells with a minimum of 14 cells used. The blue curves represent the control, and the red curves represent the proteasome perturbation. SEM is displayed in the shaded areas within the curves. (A-C), is the *rpn4Δ* (n= 47) vs the control (n= 47). (A), y-axis is the mean Cox4p foci mitochondrial intensity of live dividing cells. (B), y-axis is the mean foci area of live dividing cells. Multiple foci areas were not treated separately. (C), y-axis is the mean num of foci in live dividing cells. (D-F), is the *ubr2Δ* (n= 61) vs the control (n= 46) with corresponding y-axis to (A-C). (G-I), is the Rpn4* induction (n= 103), the pink line indicates when induction occurs. The control (n= 107) represents the same construct but without estradiol.

Seeing that proteasome perturbation can influence mitochondrial morphology and activity, we next set out to determine whether observational mitochondrial phenotypes had any relationship to aging trajectories.

Phenotypes have been used to identify aging trajectories and collapses in the mitochondrial and proteostasis hallmarks. Using our classification tool, we can distinguish between the cells that display the

aggregate state more so than another phenotype, which is indicative of the mitochondrial dysfunction and the proteostasis stress aging hallmark^{15-17,33}. For determining cells displaying mitochondrial dysfunction, we separated cells into two groups, the circular and aggregate phenotype, which is designated by the mitochondrial Cox4p-GFP (Fig. 4.6A). Interestingly, cells staying longer in the circular state had a longer RLS (Fig. 4.6B). Indicating that the circular mitochondrial state in normal aging cells may be related to longer lifespan. Interestingly, cells classified in the aggregate state had a longer budding rate time when compared to those in the circular state (Fig. 4.6C).

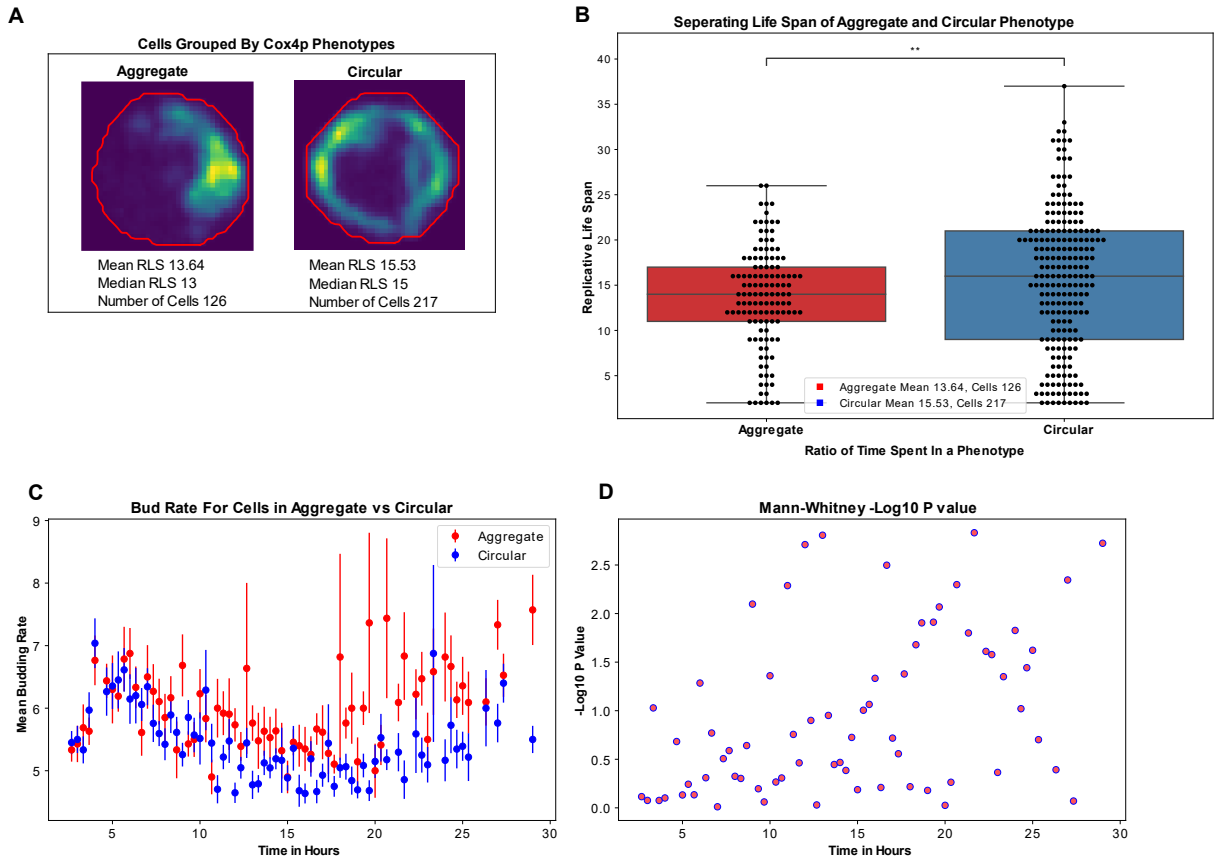


Fig 4.6. Cells displaying the mitochondrial dysfunction aging hallmark have a shorter RLS.

(A), is a example of the aggregate and circular phenotype. For simplicity, cells displaying binary and triple phenotype are reclassified into the aggregate state. Cells displaying the fragmented state are reclassified into the circular state. This is decided by observing phenotypes similarities to the aggregate or circular state. Next cells are grouped into aggregate or circular based on the time spent in the designated state. (B), is a boxplot of the RLS for each cell classified in the aggregate or circular state with a Mann-Whitney P value of $9.605e-03$. (C) is a scatter plot displaying the mean budding rate of cells in either phenotype. Times with less than 10 dividing mother cells are excluded. The SEM of cells dividing at that time is depicted as error bars. (D), the graph is the $-\log_{10}$ P values calculated using a Mann-whitney U test where each point represents individual cells budding rate calssified in the aggregate or circular state. The dataset consolidates our Cox4p-GFP and Rpn11p-mCherry strains from six independent experiments, encompassing 343 cells.

When observing the trajectory of cells in aggregate or circular states more closely, it was noted that cells that remained in the aggregate state for longer durations exhibited a smaller mitochondrial area and cell area (Fig 4.7A, C). In terms of the nucleus-to-cell area ratio, circular cells maintained a stable ratio for a more extended period (Fig 4.7D). However, this difference in ratio is influenced by the cell area, as the nucleus area remained consistent (Fig 4.7B). Overall, variations in size scaling are associated with

different mitochondrial morphologies. It is still unclear whether size scaling in a cell drives mitochondrial morphology. To date, no single gene or protein has been identified that solely influences cell size scaling. Yet, considering that the proteasome can affect both cell size scaling and mitochondrial morphology, the changes might be related to the proteasome.

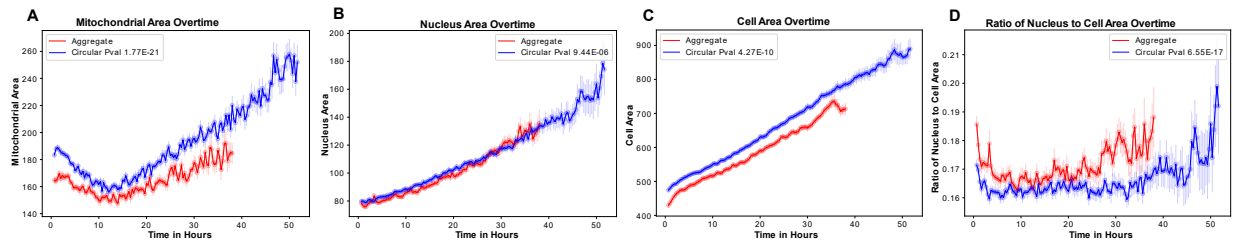


Fig 4.7. Mitochondrial morphology displays differences in scaling dynamics.

The graphs display the different organelle areas of cells classified in either the aggregate or circular phenotype. The x-axis is the time in hours of live dividing cells, times with less than 25 cells are excluded. The blue curves represent the circular (n=217), and the red curves represent the aggregate (n=126). SEM is displayed as the shaded areas within the curves. The Mann-Whitney P value between the mean values is depicted in each box. (A), is the mitochondrial inner area with the y-axis denoting the mean levels of the mitochondrial area (P value $1.77\text{E-}21$). (B), is the nucleus area (P value $9.44\text{E-}8$). (C), is the cell area (P value $4.27\text{E-}10$). (D), is the ratio between the nucleus to cell area (P value $6.55\text{E-}17$).

When clustering cells based on their mitochondrial morphology, the levels of nuclear Rpn11p and cytoplasmic Rpn11p are higher in the circular cells (Fig. 4.8A-B). As expected, aggregate cells exhibited a higher Cox4p intensity, likely due to decreasing Rpn11p levels (Fig. 4.8C-D). This confirms that the mitochondria react to decreasing proteasome levels even in a standard aging context. Decreasing Rpn11p levels coincided with a larger cell area in the circular cells; however, the nucleus area did not appear to be substantially different (Fig 4.7B-C). This suggests differences in scaling and proteasome trajectories, which are related to the mitochondrial dysfunction aging hallmark. Upon further observation of differences in mitochondrial morphology, we found the number of foci to be lower in the aggregate cells (Fig. 4.9A).

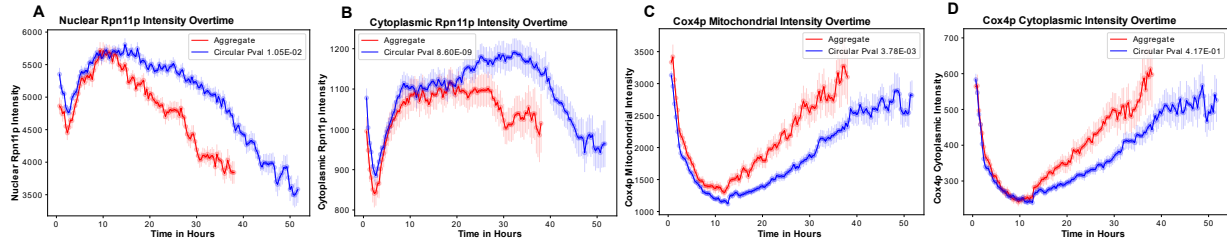


Fig 4.8. Cox4p and Rpn11p maintain distinct trajectories based on mitochondrial morphology.

The graphs display the Cox4p and Rpn11p regional intensities of cells classified in either the aggregate or circular phenotype. The x-axis is the time in hours of live dividing cells. Times with less than 25 cells are excluded. The blue curves represent the circular (n=217), and the red curves represent the aggregate (n=126). SEM is displayed in the shaded areas within the curves. The Mann-Whitney P value between the mean values is depicted in each box. (A), is the nuclear intensity of Rpn11p mCherry with the y-axis denoting the mean levels of nuclear Rpn11p (P value $1.05e-2$). (B), is the cytoplasmic levels of Rpn11p (P value $8.6e-9$). (C), is the mitochondrial levels of Cox4p intensity (P value $3.75e-3$). (D), is the cytoplasmic level of Cox4p (P value $4.17e-1$).

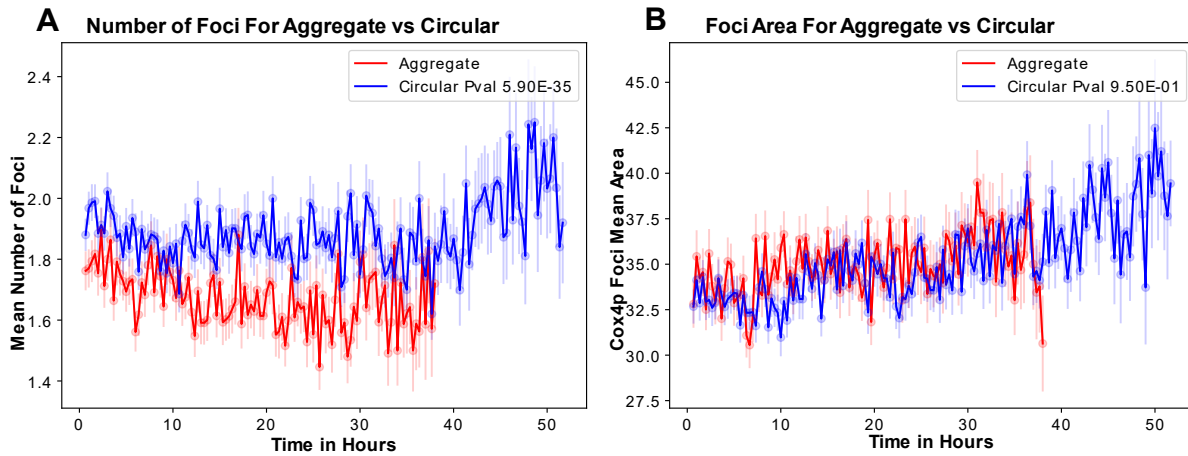


Fig 4.9. Mitochondrial circular state has a greater number of foci.

The graphs above display the foci changes in the mitochondria when cells are classified in either the aggregate or circular state. The x-axis is time in hours of live cells with a minimum of 25 cells used. The blue curves represent the circular (n=217) and the red curves represent the aggregate (n=126). SEM is displayed as the shaded areas within the curves. The Mann-Whitney P value between the mean values can be seen within each box. (A), y-axis is the mean number of foci of live dividing cells, (P value is $5.9E-35$). (B), y-axis is the mean foci area of live dividing cells, (P value is $9.5E-1$). Multiple foci areas were not treated separately.

Given the distinct trajectories of Rpn11p in relation to the mitochondrial dysfunction hallmark, we sought to determine if Rpn11p could also be used to assess proteostasis stress. Previous reports suggest that Hsp104p leads to the formation of protein aggregates due to an increase in misfolded proteins^{8,17,56}. These aggregates can be mitigated by increasing the proteasome through a Ubr2 knockout. Overexpression of Hsp104p and reduction of

rDNAs were also found to reduce protein aggregates¹⁷. On the other hand, the aggregate phenotype can be induced by reducing proteasome function through an Rpn4 knockout¹⁷. These findings suggest a strong causal relationship between the proteasome and proteostasis stress. However, it remains unclear whether proteasome protein trajectories significantly vary in cells displaying proteostasis stress. Using our phenotype identifier, we categorized cells into either the aggregate or cytoplasmic state (Fig 5.1A). This classification was based on whether the cells spent more time in the aggregate state versus the cytoplasmic state throughout their RLS (Fig 5.1C). As previously established, cells displaying Hsp104p aggregates had a shortened RLS. We further validated that Hsp104p aggregates can co-localize with nuclear Rpn11p (Fig 5.1B). We observed minor differences in Hsp104p intensity for aggregate cells and cytoplasmic cells (Fig. 5.2 A-C). Interestingly, we observed that Rpn11p levels varied in subcellular regions of cells showing different Hsp104p phenotypes (Fig. 5.2D-F). Similar to cells ending with mitochondrial aggregates, those with Hsp104p aggregates demonstrated decreasing levels of Rpn11p in nuclear regions (Fig. 5.2E). However, cells with Hsp104p aggregates exhibited marginally higher cytoplasmic Rpn11p levels compared to cells categorized under the cytoplasmic phenotype (Fig. 5.2F). This contrasts with cells containing mitochondrial aggregates, which had significantly lower cytoplasmic Rpn11p levels (Fig 4.8B). Cells classified in the aggregate state had a smaller cell area and nucleus area (Fig. 5.2G-I). Interestingly, the ratio between the two organelles was significantly higher in the Hsp104p aggregate cells.

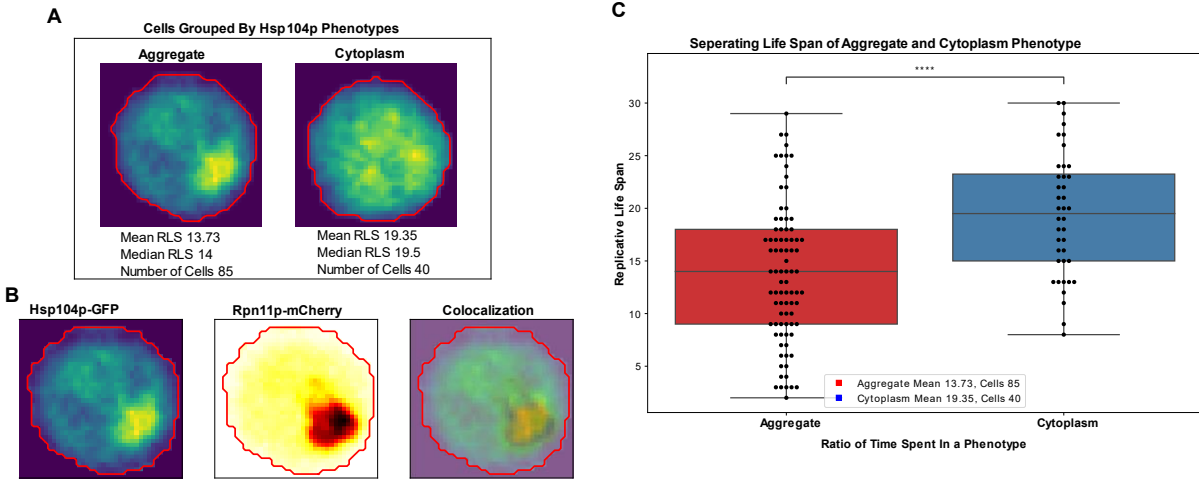


Fig 5.1. Cells displaying proteostasis stress have a shorter RLS.

Displays the Hsp104p aggregate and cytoplasm phenotype. (A), are representative images of the Hsp104p aggregate and cytoplasm phenotype. (B), is a representative image of a single cell displaying the Hsp104p aggregate, which is colocalizing with Rpn11p. (C), is the RLS of cells classified in the aggregate (N = 85, mean RLS 13.73) or cytoplasm (N=40, mean RLS 19.35) phenotype, with a Mann-Whitney P value of 6.55e-6.

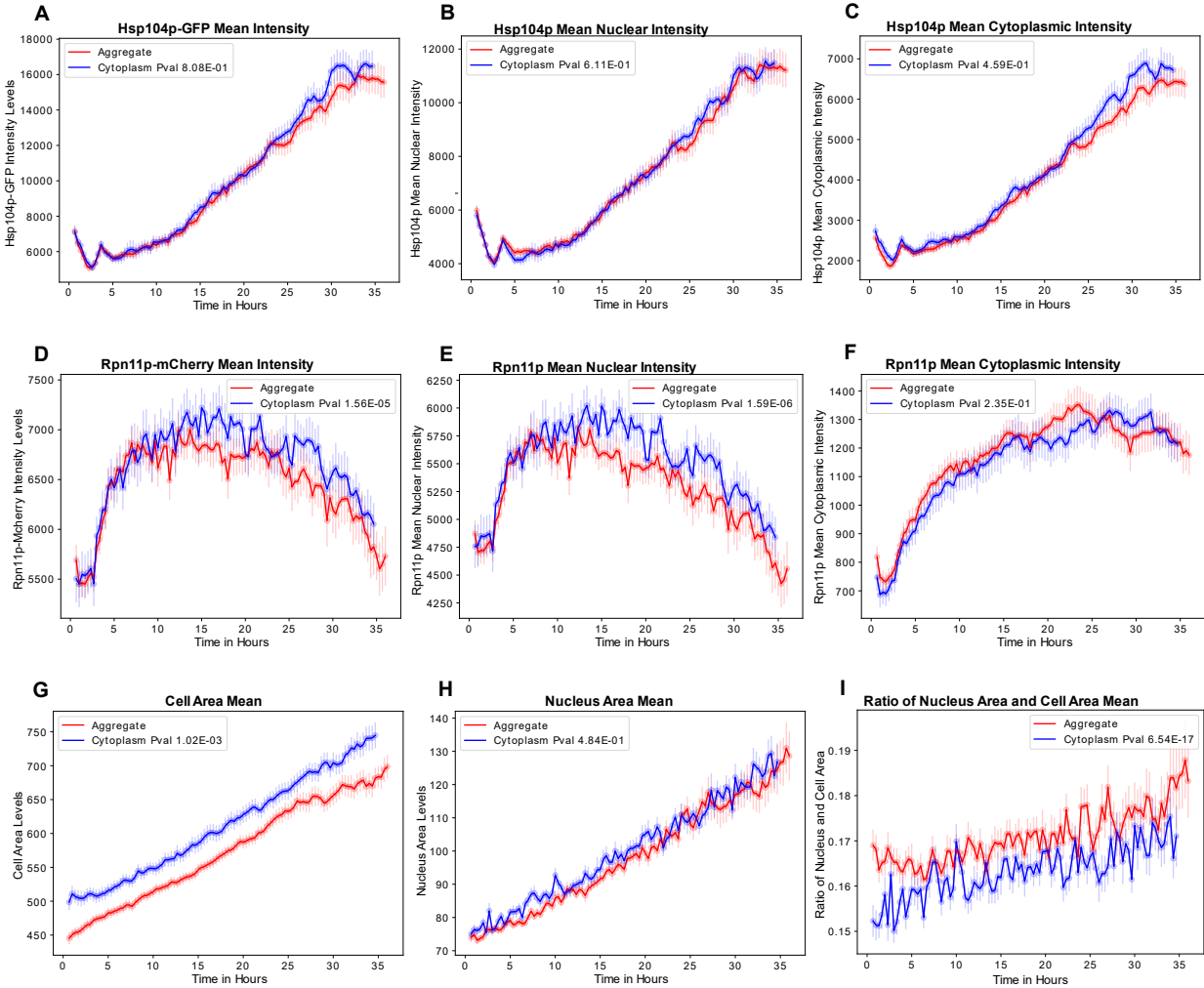


Fig 5.2. Hsp104p aggregates display distinct Rpn11p and size scaling trajectories.

The graphs above display the cells classified in the Hsp104p aggregate or cytoplasmic state. The data is an accumulation of two separate experiments composed of the same Hsp104-GFP and Rpn11p-mCherry strain. The red curve represents the Hsp104p aggregate (N = 85, mean RLS 13.73), and the blue curve represents the Hsp104p cytoplasm (N=40, mean RLS 19.35). (A), is the Hsp104p mean intensity overtime. (B), is the mean Hsp104p nuclear intensity determined by GMM of the nuclear Rpn11p-mCherry. (C), is the mean Hsp104p cytoplasmic intensity determined by GMM of the cytoplasmic Rpn11p-mCherry. (D), is the mean intensity of Rpn11p overtime. (E), is the mean nuclear intensity of Rpn11p. (F), is the mean cytoplasmic intensity of Rpn11p. (G), is the mean cell area between the different Hsp104p phenotypes. (H), is the nucleus area. (I), is the ratio of the nucleus and cell area mean overtime. SEM is depicted as the shaded regions. Time points with fewer than 25 dividing cells are excluded.

Having observed that Rpn11p possesses predictive properties for distinguishing Hsp104p aggregate cells, we sought to determine whether Rpn11p could influence Hsp104p trajectories. Previous studies have already established the influence of Rpn4 on proteostasis stress and the Hsp104p phenotype¹⁷.

Additionally, it is known that Rpn4 and the Hsp104p transcription factor regulator Hsf1 can influence one

another. However, it remains largely unknown whether Hsp104p responds to a single protein of the proteasome subunit, Rpn11p, with predictive properties for the Hsp104p phenotype. We first attempted to ascertain if there was a specific time during which Rpn11p intensity is predictive of Hsp104p levels. Surprisingly, using our non-linear Granger causality, we found that there were no instances when Rpn11p could accurately predict Hsp104p levels (Fig. 2.3). To corroborate this, we transiently overexpressed Rpn11p-mCherry in an Hsp104p-GFP and Rpn11p-mCherry strain (Fig. 2.4). This induction elevated Rpn11p levels but did not alter Hsp104p-GFP levels (Fig. 2.4A-B). The RLS and the number of remaining buds were also consistent (Fig. 2.4 C-D). Efforts to determine the effect on organelle scaling were confounded by the fact that Rpn11p-mCherry overexpression made nucleus segmentation and identification challenging, as illustrated by a representative image of the Rpn11p approximately 2 hours post-induction (Fig. 2.4F). We also could not accurately determine if the cell area was altered during Rpn11p induction (Fig. 2.4E). In summary, we did not detect significant changes in Hsp104p levels following Rpn11p induction, thereby corroborating our non-linear Granger causality test. We then sought to discern if Rpn11p induction could alleviate some of the proteostasis stress, as gauged by the Hsp104p aggregates. We observed that Rpn11p induction led to a spike in the Hsp104p cytoplasmic phenotype (Fig. 2.5C). Yet, this increase was modest, suggesting that Rpn11p might only alleviate a moderate level of stress, which does not significantly affect lifespan (Fig. 2.4A-B).

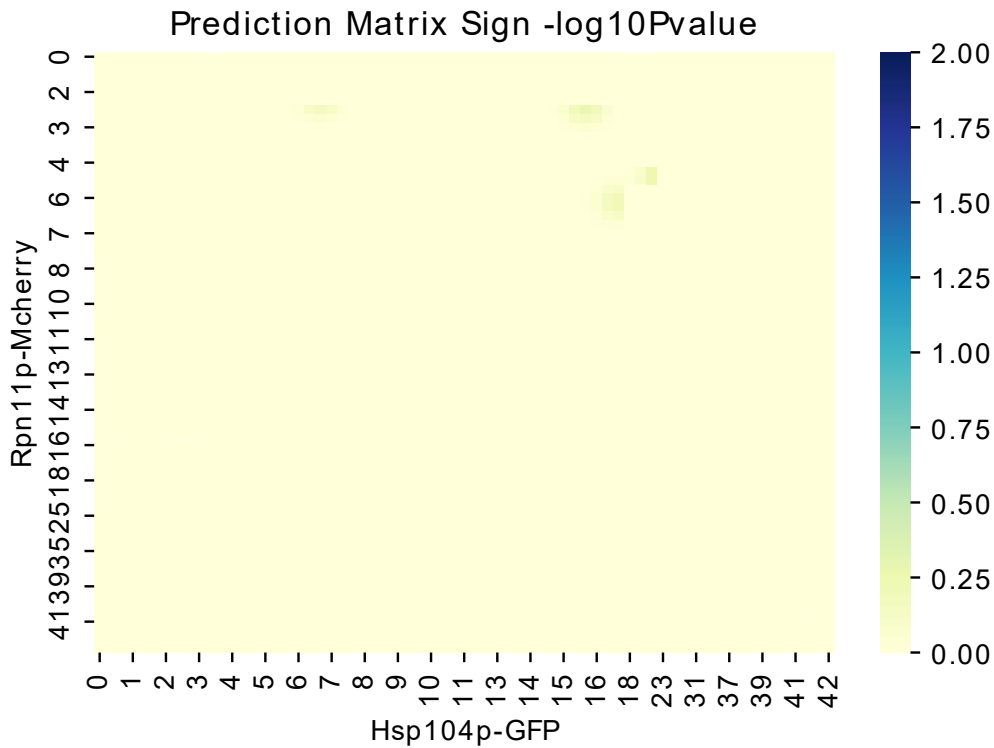


Fig 5.3. Granger causality reveals that Rpn11p cannot predict Hsp104p levels.

Predicting temporal order using Granger causality with decision trees. The heatmap presented displays the $-\log_{10} P$ values, calculated from an F-test. The y-axis utilizes Rpn11p intensity to predict subsequent Hsp104p levels represented on the x-axis. Time points for both the y-axis and x-axis indicate the hours for the respective variables. The dataset consolidates our Hsp104p-GFP and Rpn11p-mCherry strains, encompassing 125 cells. Time points with fewer than 56 dividing cells have been excluded.

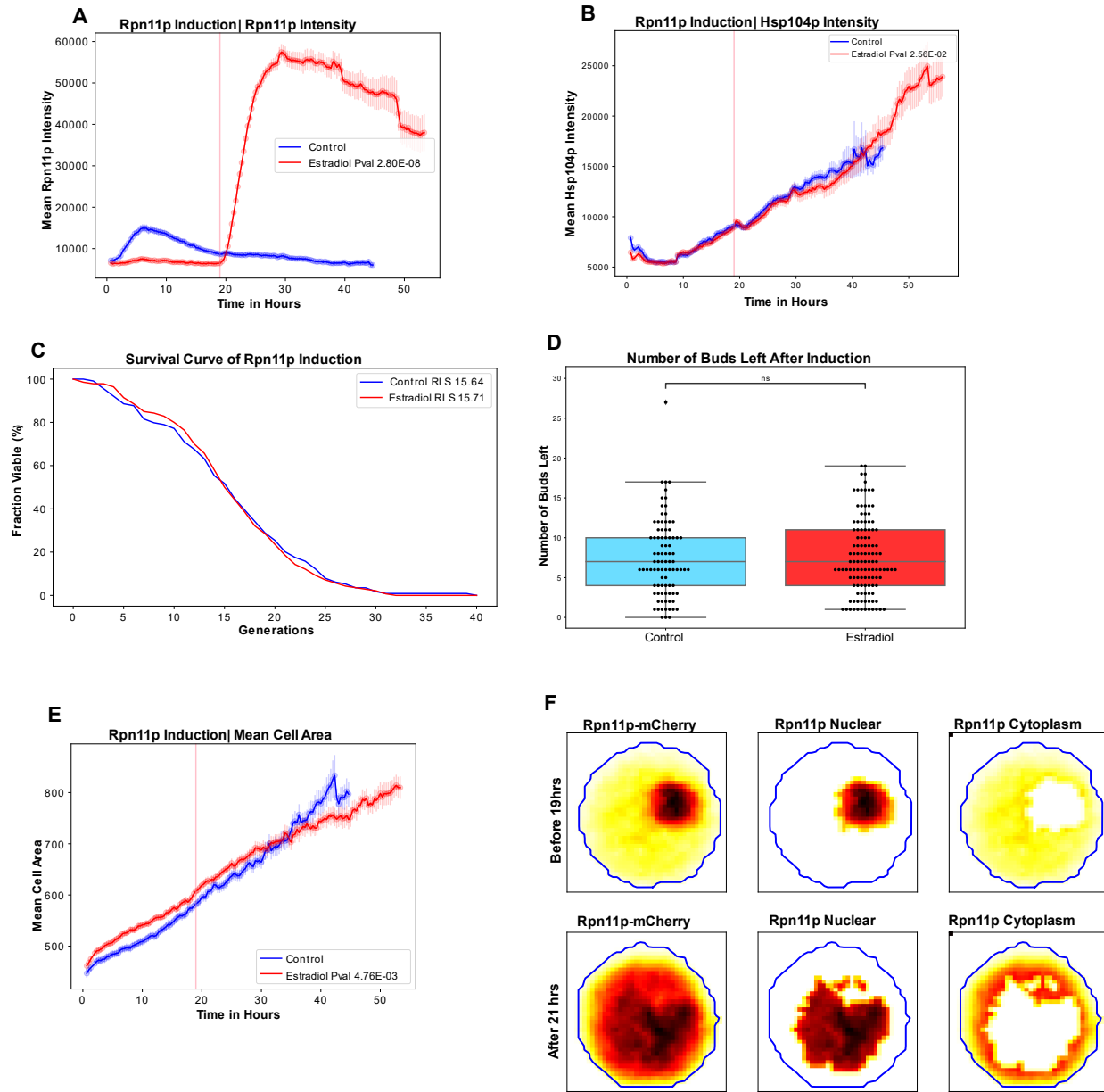


Fig 5.4. Rpn11p temporal overexpression does not influence Hsp104p intensity.

The graphs display the induction experiment of Rpn11p at 19.2 hours in a strain with a Hsp104p-GFP and Rpn11p-mCherry tag. (A) represents the Rpn11p intensity, and (B) shows the Hsp104p intensity. The x-axis indicates the time in hours for live cells tracked over time. Instances with fewer than 15 cells have been excluded. The red curve represents the Rpn11p estradiol construct that received estradiol (N=118, mean RLS=15.71), and the blue curve depicts the control (N=89, mean RLS=15.54) which did not receive estradiol. The time of induction is marked by the pink vertical line. P values, calculated using a Mann-Whitney U test, are shown on the graphs. (Figure caption continued on the next page).

(Figure caption continued from the previous page). (C) is a survival curve with the number of generations on the x-axis and the fraction viable on the y-axis. (D) represents the number of buds remaining after the media switch, either with or without estradiol; a P value of $7.760e-01$ was determined using the Mann-Whitney U test. (E) illustrates the nucleus area, and (F) provides a representative image, utilizing GMM to differentiate the nucleus Rpn11p from the cytoplasm. The top panel displays the cell before Rpn11p induction, while the bottom panel shows the same cell 21 hours post-induction. The data is an accumulation of two separate experiments.

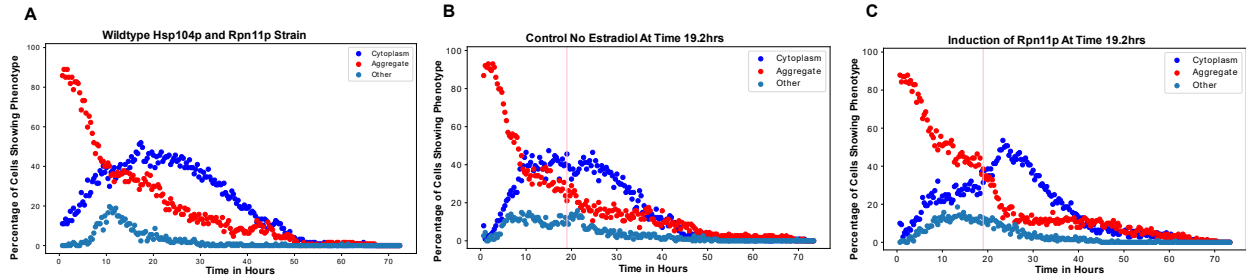


Fig 5.5. Rpn11p may modestly increase the Hsp104p cytoplasm phenotype.

The three graphs represent the percentage of live cells at each time displaying either the Hsp104p cytoplasm, aggregate, or other phenotype. The x-axis is the time in hours of live cells and the y-axis is the percentage of cells alive displaying a particular phenotype. (A) is the Hsp104p-GFP and Rpn11p-mCherry wildtype strain without an estradiol system (N=125). (B) is the Control (N=89) with the estradiol system that received no estradiol at time 19.2hrs. (C) is the induction of Rpn11p at time 19.2hrs (N=118), which received estradiol and has the estradiol system. The pink vertical line indicates when the estradiol system was induced. The experiments are the accumulation of two experiments performed independently. The experiments for (B) and (C) are done together.

DISCUSSION

We developed a phenotype identifier tool to quantify and categorize cell topologies efficiently. Using this tool, we pinpointed the proteasome as an influencer of both mitochondrial morphology and activity (Fig. 4.2 and Fig. 4.3.2). Notably, there was an inverse relationship between Rpn11p and Cox4p levels (Fig. 4.3.2 and Fig. 4.4.1), suggesting that mitochondria adapt to proteasome fluctuations. Yet, data from our *dnm1Δ* and Cox4p temporal overexpression experiments indicate the proteasome might not reciprocally adapt to mitochondrial changes (Fig. 4.3.1 and Fig. 4.4.2). This unidirectional response could be an evolutionary outcome of mitochondria integrating into cellular systems and adjusting to dynamic cellular environments. While Rpn11p mutations have been linked to mitochondrial morphology changes, the variations in mitochondrial activity might still directly correspond to escalating Rpn11p levels. This would align with our model where mitochondria adjust to proteasome alterations, especially since Rpn11p levels are modulated by Rpn4. For both mitochondrial dysfunction and proteostasis stress, we discerned the most significant scaling differences in cell area (Fig.4.7 and Fig. 5.2). When juxtaposing these scaling deviations with Rpn11p alterations, scaling deviations manifested earlier, while Rpn11p alterations emerged later in the process (Fig 4.7, Fig. 4.8, and Fig. 5.2). Nuclear Rpn11p levels consistently declined across both aging hallmarks. Conversely, cytoplasmic Rpn11p levels showed a decrease in mitochondrial dysfunction but an increase during proteostasis stress (Fig. 4.8 and Fig. 5.2). This discrepancy could stem from cell responses to either distinct or shared stressors preceding the aging signs, leading to varied Rpn11p trajectories. In both instances, scaling evidently serves as a predictor for these aging hallmarks and might even precipitate their emergence. Examining Hsp104p and Rpn11p intensity variations, we were intrigued that our non-linear Granger causality didn't reveal a strong interrelation, despite shared regulatory mechanisms (Fig. 5.3). This discrepancy might suggest divergent regulations our model can discern. Although demarcating between cytoplasmic and nuclear levels during Rpn11p overexpression proved challenging, our results implied that elevated Rpn11p levels don't influence Hsp104p (Fig. 5.4). This bolsters our hypothesis that Hsp104p levels might be steered by a distinct regulatory mechanism.

SUPPLEMENTAL

Below is table 1, which indicates proteins that were temporarily overexpressed with the designated times.

Supplementary Table 1. Estradiol System Induction Strains

Gene Induction	Times	Strain	Remaining Life Span	Phenotypes
Rpn4*	5hrs, 19.2hrs	Cox4:GFP and Rpn11: mCherry	No Difference	Increase nucleus size
Rpn11	0, 19.2hrs	Hsp104:GFP and Rpn11: mCherry	No Difference	Not significant
Rpn11-Sv40NLS	19.2hrs	Hsp104:GFP and Rpn11: mCherry	Decreased	Number of buds decreased
Cox4	19hrs	Rpn11: mCherry	No Difference	No difference

The estradiol system we used was based on the Hana El-Samad Z4EM system (see methods for more details on plasmid construction^{57,58}). We tested the concentrations of estradiol using flow cell cytometry and microfluidics. Dosages below 2nM of estradiol were excluded because their fluorescent intensity was undetectable under the confocal microscope. We utilized the Rpn11p-GFP tag as overexpression of Rpn11p did not affect RLS (See chapter 3).

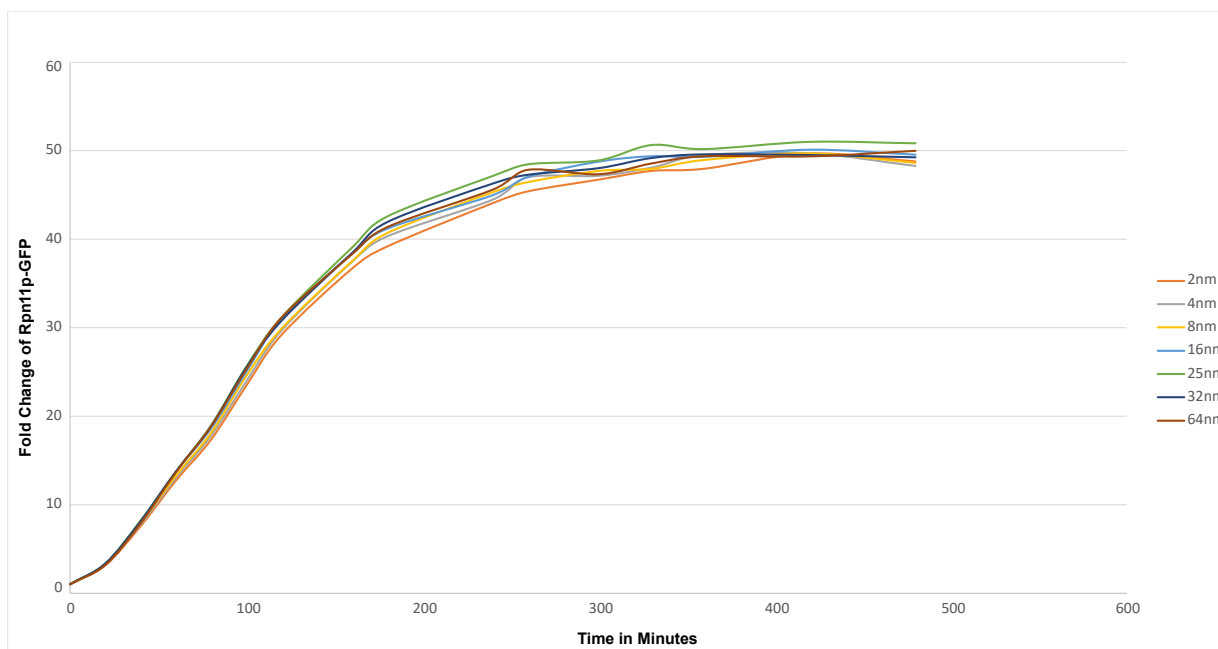


Fig. S1.1. Measuring estradiol dosage response by Rpn11p-GFP

Dose-response curves for varying concentrations of Beta estradiol on an endogenous Rpn11p-mCherry and inducible Rpn11p-GFP strain. The x-axis represents time in minutes, while the y-axis depicts the fold change in Rpn11p-GFP intensity. Different estradiol dosages are represented by distinct colors: 2nM, 4nM, 8nM, 16nM, 25nM, 32nM, and 64nM. Intensities are recorded at intervals ranging from 20 to 40 minutes over an 8-hour period.

To assess the stability of estradiol under light exposure and ensure strict regulation of the construct, we conducted a live imaging experiment. We used the three candidate estradiol concentrations previously identified in Fig. S1.1 and captured images at 30-minute intervals. Due to constraints imposed by the number of wells compatible with a 63x oil lens, we couldn't test additional concentrations or shorter time intervals. Our findings suggest that RLS might be impacted by higher estradiol dosages when used in conjunction with the microfluidic device (Fig. S1.2A). Nonetheless, the system demonstrated tight control, with 16nM of estradiol emerging as the most promising candidate for gene expression (Fig. S1.2B).

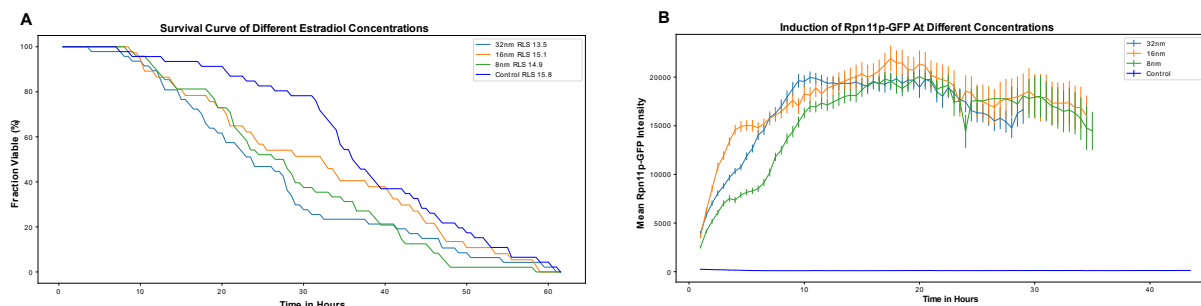


Fig. S1.2. Observing Z4EM estradiol system in the microfluidics device.

Different dosages of estradiol were tested: 16nM (N=47, Mean RLS=15.1), 32nM (N=47, Mean RLS=13.5), 8nM (N=48, Mean RLS=14.9), and 0nM, which served as the control (N=46, Mean RLS=15.8). (A) illustrates a survival curve based on various estradiol dosages administered one hour after plating. The x-axis represents time in hours. P-values derived from the Mann-Whitney U test were calculated for the survival curve in comparison to the control: 32nM (P value=2.6e-4), 16nM (P value=4.5e-2), and 8nM (P value=1.6e-2). (B) depicts the intensity of Rpn11p-GFP post estradiol induction. The x-axis indicates the time in hours for live, dividing cells, with time points having fewer than 15 dividing cells being excluded. The y-axis denotes the mean Rpn11p-GFP intensity.

To determine temporal ordering, I initially employed linear models such as ARMA, ARIMA, Pearson correlations, and VAR models. However, the inherent noise and non-stationarity in our data posed challenges for these models since they are optimized for stationary data, including Granger causality. My efforts to denoise the data through differencing or smoothing proved unproductive, at times obscuring relationships or introducing spurious ones. Consequently, I turned to decision trees for their ability to capture non-linear relationships. To mitigate overfitting, I restricted the tree depth and used stringent parameters for data comparisons (See methods 2.6). By normalizing the data between 0 and 1, I focused on comparing trend changes. The non-linear Granger causality model parameters were designed specifically for our vacuole and mitochondrial dataset. Since vacuole dysfunction is known to precede mitochondrial dysfunction, and not the other way around, we used this established knowledge to assess if our model could differentiate between causal relationships (Fig. S1.3.A-B). We found Vma1p trend changes are predictive of mitochondrial Cox4p changes (Fig. S1.3.A-B). To validate the model against spurious relationships, I perturbed our times and shuffled cell IDs (Fig. S1.3.C-D). This helped to validate whether the model identified true signal. After utilizing our model to identify times when the proteasome predicted changes in the nucleus area (See Chapter 2), I evaluated its capacity to detect the transitory overexpression of Rpn4* at 5.5 hours. This overexpression directly influenced the proteasome and

subsequently the nucleus area. The results from the model were in agreement with our experimental findings as highlighted in Chapter 2 and supplementary figure S1.3E-F. Our non-linear Granger causality model proved remarkably adept at determining temporal order. Yet, a fundamental limitation of Granger causality is its inability to definitively distinguish cause from effect. Hence, induction experiments are essential to validate the findings from the non-linear Granger causality model.

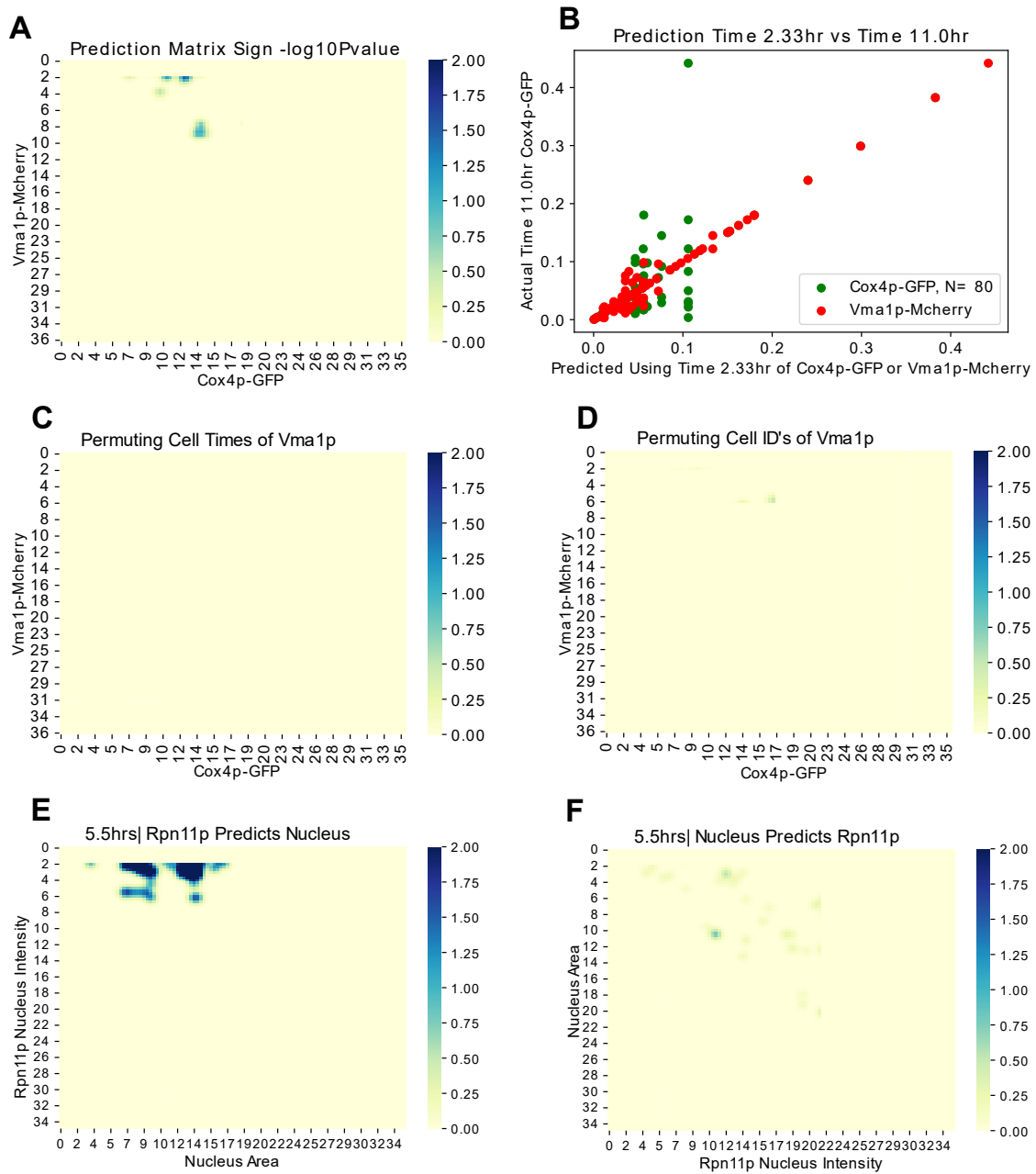


Fig. S1.3. Validating methodology for non-linear Granger causality

(A), the y-axis is Vma1p intensity times, and the x-axis is Cox4p intensity times. (B), displays the predictive values on the x-axis and the actual values on the y-axis. At 2.33 hours Vma1p is predictive of Cox4p at 11 hours. The two colors indicate the different features being used to predict Cox4p at 11 hours. Red is Vma1p intensity, and the green is Cox4p intensity. (C-D) different permutations applied to Vma1p time series. (C) is Vma1p intensity times being randomly permuted. (D) is Vma1p intensity of different cell labels being randomly permuted. (Figure caption continued on the next page).

(Figure caption continued from the previous page). (E-F) is applying the method on a validation dataset where Rpn4* is induced at 5.5 hours. (E) is observing when Rpn11p nuclear intensity is predictive of the Nucleus area. (F), is using the same dataset and observing whether nucleus area is predictive of Rpn11p nucleus intensity.

DISCUSSION

Hsp104p increased overtime whereas both Rpn11p and Rpn6p decreased. The proteins are representative of different parts of the proteostasis pathway that work together yet their behavior differs. As Hsf1p levels increase over time and Rpn4p is negatively regulated by rising proteasome activity, it's plausible that chronic stress due to aging disrupts the balance between proteasome and chaperone protein regulation. Intriguingly, Rpn11p overexpression did not influence Hsp104p levels. This suggests that the chaperone response is influenced by upstream regulators of proteostasis proteins, particularly the transcription factors Msn2p, and Hsf1p. Notably, Hsp104p levels have been observed to rise over time in conjunction with Msn2p, and Hsf1p⁵. This likely stems from the Hsp104p promoter possessing multiple binding sites for these stress-related transcription factors^{5,59}. The transcription factors that regulate Hsp104p have been noted to interact with Rpn4. Our data and literature suggests that the proteasome indirectly affects Hsp104p aggregates by removing the misfolded proteins. It is curious that Rpn11p levels does not increase linearly like Hsp104p, this could be because it may not have as many binding sites for these stress-related transcription factors. Another possibility is the chaperone and the proteasome are responding differently to the increasing cell size and protein synthesis. Our data indicates a clear relationship of the proteasome directly influencing the scaling dynamics. However, we cannot rule out the impact of protein translation as the *sgf73Δ* affected both the proteasome and scaling trajectories. When exploring how certain nuclear proteins trajectories differ within the nucleus, we found that Whi5p and Hsf1p increased with time whereas proteins like Hh01p displayed similar trajectories to the proteasome proteins. The notion that some of the proteins seem to increase with time whereas others decrease may tie to the idea that perhaps certain protein promoters scale with organelle size whereas others do not. The change could also be due to certain nuclear transporters becoming dysregulated due to aging. We investigated the scaling dynamics between the nucleus and cell area during cellular aging, identifying an approximate two-fold increase in both parameters. The nucleus area also increased in differently aged mice tissue of the lung and liver. Our analysis revealed a negative correlation in the nucleus area ($R=-0.42$) to RLS. The cell area had a milder correlation ($R=-0.215$). While connection between cell area and

RLS appeared tenuous, a pronounced correlation emerged between the rate of change in cell area and RLS, highlighting that cells with accelerated growth tend to exhibit shorter RLS. Interestingly, the negative correlation observed in the nucleus area slope was predominantly attributable to the short-lived cells. This observation aligns with previous findings, in which significant enlargement of the nucleus area was documented towards the end of lifespan. Although the nucleus and cell area scale in size, it would appear that the nucleus area does not increase linearly to the cell area. Perhaps the increase in cell size is driven by increasing protein translation of cytoplasmic proteins more so than nuclear proteins. Our Hsp104p, Rpn6p, and Rpn11p data supports this notion as both cytoplasmic levels increased while the Rpn11p nuclear, Rpn6 nuclear, and Hh01p levels decreasing. However, when we overexpressed nuclear levels of Rpn11p-SV40NLS tag we did not see a dramatic increase in the nuclear size. This may suggest that certain key protein complexes are needed to increase the nucleus size and simply increasing a nuclear protein, especially a deubiquitinase, may not be enough. This suggests that the difference in size scaling may be related to nuclear and cytoplasmic transport of specific proteins. Our studies cannot rule out the impact of increasing extracellular transport which could be attributing to the rapid increase of the cytoplasm over the nucleus. It has been posited that size scaling dilutes and mediates protein production. Our findings support the notion that perturbations in the proteasome can affect the nucleus area, but it is unclear how this occurs. Our SV40NLS tag indicated that this increase in nucleus area is not due to increasing nuclear Rpn11p. Despite overexpressing the proteasome, a gradual decline in Rpn11p nuclear trajectory persists, leading us to consider the possibility that this decrease might be influenced by the expanding nucleus area. As the nucleus area increases, we observe a significant reduction in the proteasome. Perhaps the decrease is due to the nucleus area diluting the proteasome levels. However, this hypothesis does not account for the continued decline in Rpn11p intensity when the nucleus area stabilizes, as seen with the *fov1Δ* and *sgf73Δ* mutants. The major decrease in nuclear Rpn11p cannot be accounted for by the increasing cytoplasmic Rpn11p. Further investigation is required to unravel these complex interactions of what is decreasing nuclear Rpn11p. When classifying strains into short-lived cells or long-lived cells, we found different trajectories between the nucleus area, cell area, and ratio of the

areas. The short-lived cells' organelle areas were found to increase more so than the long-lived cells. The phenomenon is observed in all knockouts and proteasome overexpression experiments, indicating that perhaps the scaling dysregulation is a universal path. The observations also indicate the proteasome is not the predominant controller of the size scaling as different perturbations, *sgf73Δ* and *fob1Δ*, influenced scaling independent of Rpn11p changes. Apart from *fob1Δ*, the RLS extending knockouts displayed an initial smaller cell area, yet all the life extending mutants maintained the ~ two-fold increase from the initial state. The idea of cells growing to a certain point supports the loss of scaling as a possible endpoint for a cell. It also opens the idea of utilizing size scaling to predict age or RLS. It is still unclear how the cell knows when it reaches this ultimate size. In both mitochondrial dysfunction and proteostasis stress, differential scaling is apparent. Mitochondrial dysfunction, marked by Cox4p aggregates, yielded cells with significantly smaller cell and nucleus areas but a higher nucleus-to-cell area ratio. A similar pattern was observed in proteostasis loss, characterized by Hsp104p aggregates. These variations in organelle scaling proved more distinctive than Rpn11p and seem to relate with aging hallmarks, possibly even driving their appearance. The overexpression of Rpn4* was associated with an increase in nucleus area and altered mitochondrial morphology. Whether the changes in mitochondrial morphology occur because of the proteasome or the changes in scaling dynamics remains to be elucidated. Despite overexpression of Rpn4* and the similarities to that of the *ubr2Δ*, we did not observe a major lifespan increase in the cells. While Rpn4 enhances the activity of the proteasome, it's possible that under stressful conditions, the proteasome could become overwhelmed with damaged proteins. This could lead to a delay in removing the harmful Rpn4 target proteins, subsequently reducing the viability of the cell. Currently, there has been no lifespan measurement study to solely overexpress Rpn4 in cells as most studies rely on *ubr2Δ* to increase RLS. However, just like *ubr2Δ* we observed that induction of Rpn4* could influence scaling trajectories as well as mitochondrial morphology. Whether the healthspan of a cell is affected remains unclear. The *dnm1Δ* has been reported to increase RLS through an unknown mechanism. In our hands we did not observe an increase in RLS. Instead, the survival curve of *dnm1Δ* (mean RLS=12.79) is slightly lower in comparison to wildtype (mean RLS=14.63). However, the *dnm1Δ* growth curve is similar to

wildtype as previously indicated⁶⁰. The variations in RLS could be due to the difference in measuring lifespan using a microfluidics device vs micromanipulation. In typical micromanipulation experiments, cells are placed in a petri dish and are generally taken in and out of a 4 celcius fridge. The changes in conditions could thereby alter the mutants lifespan. Another possibility is the *dnm1Δ* is more sensitive to stress and thereby the extension in lifespan may have been inhibited. However, the *dnm1Δ* still displayed the predominant mitochondrial aggregate phenotype. The *dnm1Δ* mutation is known to affect mitochondrial activity, and in line with this, we also detected an upregulation of Cox4p. Furthermore, we utilized the *dnm1Δ* mutation to assess the potential effects of mitochondrial morphology on the proteasome. We observed similar Rpn11p levels and trajectories compared to the control. This suggests that Rpn11p may not respond to the mitochondrial aggregate phenotype. Previously, it has been noted that Rpn11p has a role in mitochondrial morphology, yet *dnm1Δ* did not cause any major changes to the proteasome. Either the proteasome does not respond to changes in mitochondrial phenotypes or the mitochondrial alterations do not significantly disturb the homeostasis of the cell. Despite the mitochondrial morphology not having a dramatic effect on the proteasome, we cannot exclude the possibility that other mitochondrial phenotypes could influence the proteasome. Additionally, our data seems to indicate a cross talk between the proteasome and the mitochondria where perhaps the mitochondria activity may increase when the proteasome is compromised. This seemed to be the case in our *rpn4Δ*, where the cells maintained a stronger presence of a circular phenotype with higher levels of Cox4p. We did not see an increase in the circular phenotype occurring in natural aging cells where the levels of Rpn11p decrease with time. Instead we observed a decline in the circular phenotype and an increase in the aggregate and other phenotype. However, we did observe an increase in Cox4p intensity indicating a change in mitochondrial activity. This suggests a different mitochondria response to the proteasome. Furthermore, we discovered Rpn11p levels to be a strong predictor for cells identified within the mitochondrial aggregate or circular state. Remarkably, both the nuclear and cytoplasmic levels of Rpn11p were found to be lower in these cells. This decline was accompanied by an increase in Cox4p levels, a cytochrome protein involved in the respiration chain. In yeast, a shift from glycolysis to cellular

respiration occurs due to aging, but the underlying reasons for the energy alteration remains unclear. Our investigations into proteasome perturbations revealed a causal role in mitochondrial morphology and cellular respiration activity. We observed that the levels of Cox4p decreased with proteasome overexpression and increased with proteasome downregulation. Paired with our observational findings, our data supports a causal relationship where the decreasing proteasome drives the increasing levels of Cox4p activity. These results hint at a complex interplay between the proteasome and cellular energy metabolism that warrants further exploration. Rpn11p emerged as a more insightful predictor for cells in the Hsp104p aggregate state than Hsp104p itself. Our analysis revealed that while nuclear levels of Rpn11p decreased, cytoplasmic levels increased. In yeast, maturation of the proteasome occurs within the nucleus before it is exported to the cytoplasm where it will remain active. The increasing cytoplasmic Rpn11p levels in Hsp104p aggregates reinforces earlier findings that have linked the Hsp104p aggregates to elevated proteasome activity. Strikingly, this trend contrasts with the mitochondrial dysfunction hallmark, where we observed a decrease in cytoplasmic Rpn11p levels. This divergence in proteasome activity between hallmarks highlights differences in proteasome behavior and impact. The intensity of Rpn11p had a larger decline in both the short-lived cells and cells classified in the mitochondrial aggregate state. This suggests the possibility of the declining levels of the proteasome, which may start the cascade of aging hallmarks. It is still unclear, however, the cause of decline in Rpn11p or the proteasome. The *sgf73Δ* changed the trajectory of the Rpn11p nuclear levels where it remained lower than the control and maintained a steady rate. This suggests that perhaps the proteasome may be responding to changes in protein synthesis. Whether protein synthesis leads to cell size increase or vice versa remains to be determined. Our data raises a question on key differences in aging pathways and their overlaps. It is also possible the proteasome, protein synthesis, and scaling changes may be influencing each other in a circular fashion, where like a spinning top one may become dysregulated, which pushes the others and thereby leads to a feedback mechanism.

CONCLUSION

Our findings identified a causal relationship between proteasome and scaling dynamics, with differential scaling and proteasome activity as predictors of the mitochondrial dysfunction and proteostasis stress hallmark. While our findings have shed light on the influence of proteasome on nuclear area, the mechanisms remain elusive. This study has paved the way for further exploration of the interplay between proteostasis, organelle scaling, and the aging hallmarks. Importantly, our observations emphasize the differential responses to aging hallmarks, raising key questions about differences in aging pathways and their overlaps.

METHODS

1.1 Strains

By4741 (*MATa his3Δ1 leu2Δ0 met15Δ0 ura3Δ0*) was used.

1.2 Cell Tracking and Segmentation Pipeline

For segmentation a pretrained Unet model was trained to receive one channel 512x512 images. The pretrained model was trained on a curated dataset containing only segmented yeast mother cells. The purpose was to teach the model to differentiate between cells and the microfluidic device wells. The pretrained model was then retrained on a training set data composed of the YeaZ dataset and our hand segmented dataset of yeast cells. Cell masks are generated by turning all values, including Yeaz dataset into 0 or 1. A Binary Cross Entropy with logits loss function and Adam Optimizer is used with a starting learning rate of .001. The model was trained for 100 epochs on batches of 5 with 755 images, each image contained 3-300 cells. Out of the 755 images, 423 are images made from experiments using the Li lab's microfluidics device, while the rest are composed of the YeaZ dataset. The model's accuracy was determined on a testing dataset of 14 images, which were created through a separate imaging experiment that the model has never seen, each image contained more than 5-100 cells. Augmentations used included random horizontal flipping, random vertical flipping, random rotations (0,24,90,135,270), gaussian blur, random gaussian noise, colorjitter, CutMix, Random Crop, and translations. The final Unet model is trained to receive a single 512x 512 image. Out of the 17 Zstacks taken per time for each well and experiment, only the top two brightfield images were extracted and merged. The top two brightfield images for each mother cell are identified using a Laplacian absolute value mean. Images are then normalized to values of 0-1 and fed to the trained Unet model to determine cells. After segmentation, the boundary of the cell was determined by using skimage find contour function. Yeast mother cells were identified during the first timepoint of imaging and tracked using a python-based pipeline. Should issues arise due to segmentation, the pipeline used a watershed-based approach to further help separate out daughter cells from mother cells. The cell's previous cell eccentricity and cell area is used to determine

whether segmentation proceeded correctly. If not, the model would back track to create a better segmentation. If the model failed to track the cell, manual hand curation is utilized. This occurred in cases where large shifts in the microscope occurred or several mother cells are plated relatively close, pushing the others. To filter out any outliers, a Pearson correlation of the cell area to timepoints up to the last budding time of an individual mother cell is calculated. Only cells with a Pearson value greater than .7 are kept for downstream data analysis.

1.3 Segmentation of Nucleus in Liver Cells

The data is shared through Diana Jurk. Images are of high quality and segmentation. The nucleus segmentation procedure was executed through the Python programming language utilizing multiple packages: readlif.reader, scipy.stats, time, numpy, skimage.measure, and pandas. The process was initialized by loading images from LIF files using the LifFile function from readlif.reader. The nucleus segmentation process was initiated by obtaining the DAPI-stained image of the cell nucleus. A binary mask of the nucleus was generated through adaptive thresholding, where pixels with intensities greater than the mean plus one standard deviation were set to true. Post thresholding, any remaining holes in the binary mask were filled using the binary_fill_holes function from scipy's ndimage module, and small objects less than 700 pixels in size were eliminated using the remove_small_objects function from the skimage.measure module. Using a similar method the cytoplasmic mask was created. For each nucleus, the overlap with the cytoplasm mask was determined. Only nucleus sizes that shared one overlap with a cytoplasm label are kept. Further filtering included removing cells where the nucleus area is larger than the cytoplasmic area. Cells are then checked by eye to determine proper nucleus segmentation.

1.4 Segmentation of Cryo-Section Lung Data

The U-Net architecture was utilized for semantic segmentation of cellular structures in microscopic images, beginning with a pretrained U-Net model designed for 512x512 yeast segmentation. This model was trained on a subset of nucleus data, augmented with additional images from various sources. The dataset included 81 images from a study published on the European Bioinformatics Institute website

(<https://www.ebi.ac.uk/biostudies/bioimages/studies/S-BSST265>), 34 images from previously published aged fibroblast DAPI stains, and 18 miscellaneous images of lung fibroblast and passaged fibroblast cells. Two hand-annotated images were used for validation, these images had more than 50-100 cells each. All images had reasonably segmented cells. The U-Net model was trained with a dataset that was augmented through random rotations, zooms, shifts, CutMix, and flips. Brightness and contrast of the images were randomly adjusted for additional variety. Given the usage of a pretrained U-Net model, only 30 epochs were required for training with a starting learning rate of 0.001. The Adam Optimizer and a Binary Cross Entropy with Logits Loss (BCEWithLogitsLoss) were used in the training process. The Soft Dice Loss was deemed detrimental to model performance. A smaller batch size of 3 was favored for better learning. Images larger than 512x512 were patched and fed to the model for training. For segmentation, if the image exceeded the size of 512x512, it was cropped to patches of this size. Padding is added if the image is too small. A threshold selecting for nucleus areas between 80 and 500 was applied. This filter eliminated most double nuclei and overlapping cells. To validate the findings of the violin plot, more stringent thresholds were applied using eccentricity of .6 and .7 to filter out cells that were less circular. The general trend of older cells possessing a larger nucleus area was maintained. The figure focused on using the nucleus area threshold of 80 to 500 as it captured most of the cells.

1.5 Foci Segmentation

For the main training set data, 628 files, focusing heavily on mitochondrial foci, were utilized. A total of 179 images lacking proper cell segmentation were used to facilitate model training, supplemented by 13 images of Cox4p-GFP and 16 of Rpn11p-mCherry foci that were augmented by hand. A separate hand-curated validation set contained 25 files from an independent Cox4p-mCherry-tagged experiment not included in the training set data. Augmentation techniques such as CutMix, random erasing, horizontal and vertical flipping, random rotations, translations, gaussian blur (sigma of 2), and random gaussian noise were implemented to enhance model robustness. The weights were initialized using the yeast U-Net model, designed for 512x512 input images and segmentation. However, the image size for training and

foci detection was reduced to 40x40. Cells were identified using our segmentation pipeline, and the mother cells were cropped. To maintain a consistent 40x40 image size, padding was added and blank areas were filled with the minimum intensity value found within the cropped cell. For model training, we employed the Binary Cross-Entropy with Logits Loss (BCEWithLogitsLoss) function, Adam optimizer, and an initial learning rate of 0.0001. The model underwent 50 epochs of training with a batch size of 25.

1.6 Phenotype Classifier

Seven phenotypes are classified for a training set data of 10713 images and validation dataset of 965 images. Phenotypes are identified using GFP tagged data collected from our single reporter strains. Phenotypes are easier to see when performing a background subtraction on each of the 17 zstacks before aggregating the zstacks together. Training images and validation images are identified through a Mean Maximum Discrepancy Variational Autoencoder to identify novel protein characteristics and confirmed by hand. The phenotypes included, Circular (2022 images), Aggregate (2338 images), Cytoplasm (1549 images), Other (1475 images), Fragmented (1357 images), Binary Aggregates (1144 images), and Triple (828 images). The Other phenotype included images of phenotypes not identified. The phenotype labeled Aggregate can be used to differentiate between Hsp104p aggregates, nuclear localization, and mitochondrial aggregates. The Circular, Fragmented, Binary Aggregates, and Triple phenotypes pertain specifically to the mitochondria but could be used on other organelles. The model was tested on two separate datasets to determine its accuracy. The mitochondrial marker was Mdm38p-GFP and the cytoplasmic was Trx2p-GFP treated with rapamycin, for a total of 965 testing images with about 120-150 images per category. To create a classifier model, we used a pretrained ResNet50 model trained on the ImageNet database. The ResNet50 is then retrained on our phenotype data. Here, I merged the first layer of the pretrained ResNet50 model into one channel. All portions of the model were frozen except for the first conv1D and the last linear layer. Segmented single mother cells are fed to the model, these cells are resized to a 224x224, to utilize the pretrained properties of the ResNet50 model. Augmentations used: random rotations (0,45,90,135,180,270), horizontal flipping, vertical flipping, gaussian blur, random

noise, unsharp filter, and random translations. To further help the model identify key differentiating phenotypes, a random threshold is performed along with downsizing and then resizing the images to increase blurriness. The MixUp augmentation did not help with model performance. Model was trained with a batchsize of 32 for 100 epochs with a Adam Optimizer and a starting iteration rate of .0001. Accuracy is further tested by using knockout experiments to determine if the model could accurately identify phenotypes. The *dnm1*Δ is known to cause mitochondria aggregation and ablate the mitochondrial circular phenotype. The trained ResNet50 model corroborated this.

1.7 Microfluidic Setup

Cells were grown overnight in YEPG media free of glucose. Cells were then diluted from an O.D of 600 through a 1/5 dilution and allowed to grow for 3 hours and 30 minutes before washing the cells with YEP three times and incubating in YEP for 1 hour. By placing in YEP for an hour most cells will be temporarily arrested. After incubation, cells were diluted 1:2 with YEPD and plated using a PSI of 20 to insert cells in the wells. Adding 135ul of fresh YEPD media, cells plated in the wells are washed using a pump to push new YEPD media for 2 minutes at a PSI of .5. The media is then removed and a fresh 280ul of YEPD is added on one side of the well and 135ul of YEPD on another. Neighboring empty wells will receive 250ul of water to help with hydration. Imaging begins anywhere between 20-30 minutes after plating.

1.8 Confocal Imaging Protocol

Cells are imaged every 20 minutes using the lowest laser settings possible to view tagged proteins. Cells are incubated at 30 Celsius. A Zeiss Axio Observer Z1 at 63x oil objective is used to capture cells every 20 minutes and 17 zstack images are acquired with .45um distance. A Zeiss microscope was used with two laser settings 405nm and 588nm. Laser power was at 15% and exposure time was 200ms.

1.9.1 Protein Quantification

Proteins were quantified using custom python code to identify single mother cells and quantify fluorescent protein tag. Median background pixels is obtained per zstack by observing areas without cell

or well occupancy. Protein tags are quantified by taking the pixel sum values per zstack of the region of interest designated by the mother cell segmentation program. Next the median background for that zstack is subtracted from the values. Protein intensity can be determined by normalizing the total pixel values by the area of occupancy of the respective proteins or organelle areas. Organelle areas can be determined by pixel occupancy.

1.9.2 Mobaraki Method

The analysis focuses on identifying the high region of intensity per zstack for each single cell and time. First, for each z-stack, the median background was identified and subtracted from the sum of the cell's pixels to derive an initial measure. This value was then divided by the protein occupancy within the corresponding cell. The values were then summed across the seventeen zstacks. To accurately calculate the protein occupancy, we began by subtracting the median background for each z-stack's image and converting any resulting negative values to zero. This yielded an initial estimation of occupancy, which we further refined using a Gaussian filter with a sigma of 1, blurring the image to fill any empty regions. We then defined a threshold based on the mean of the blurred image, and by summing the pixels greater than this threshold, we isolated the occupancy of high pixel intensities within each z-stack per single cell. This methodical approach allowed us to establish a quantification of protein intensity by incorporating background correction, statistical filtering, and thresholding techniques tailored to each z-stack within individual cells.

1.9.3 Gaussian Mixture Model (GMM)

To obtain strong differences between distributions zstacks were aggregated together, which allowed both signal and noise to increase. After which, a gaussian filter with a sigma of 3.5 is applied to the aggregated image to further distinguish distributions. The mother cell is then segmented. The Max threshold is used to identify pixel regions that were greater than or equal to the threshold. The min peak comprised of values less than the max threshold. Using the regions identified though GMM, the pixel intensity, sum,

and area was identified in the aggregated image before gaussian filter. Through visual inspection the nucleus, mitochondria, and vacuole organelle could be distinguished.

2.1 Induction Experiment Protocol

Fresh media containing 16nM of estradiol was made each time. Experiments were paused and media was removed on both well sides. 135ul of new media would be added. The well that would be induced, received fresh estradiol. The control would receive fresh YEPD media without estradiol. The media would be pumped using a PSI of .5 for 2 minutes after which the respective media would be removed and replaced with a new fresh media of YEPD with 16nM of estradiol or YEPD. Volume added is 280ul for one side of the well and 135ul on the other side.

2.2 Protein Tagging with Fluorescent Tags

Saccharomyces cerevisiae strains were generated using standard yeast transformation techniques to enable protein quantification and phenotypic analysis. Three fluorescent protein tags were employed for this purpose: Green Fluorescent Protein (GFP), mCherry, and a near-infrared fluorescent protein (iRFP). These tags were fused to the C-terminus of a target protein of interest, which was selected based on its well-characterized expression pattern and biological significance identified through our preliminary analysis. Selection markers for the fluorescent tags used are nourseothricin, Ura3, and hygromycin B. Plasma membrane P2-type H⁺-ATPase, Pma1p, is fused to iRFP to tag the individual mother cells, however, in our experiments the marker was not used to identify or keep track of the single mother cells.

2.3 Gene Deletion

Kanamycin gene was inserted between the promoter and the terminator of a gene of interest. For homologous recombination, Primer designs of 57bp of the start of the coding sequence and 57bp of the end of the terminator are used. Deletion is confirmed through gel PCR and sanger sequencing composed of primers 500bp upstream and downstream of the gene of interest. For all knockouts at least 5 or more colonies are seen 3-4 days after plating cells on a kanamycin plate.

2.4 Estradiol Plasmid Construction

The estradiol Z4EM plasmid was given to me by the Hana El-samad lab. The plasmid was remade to insert into the Ura3 region with a kanamycin selectable marker, site insert, and Cys4 protein. The Ret2 promoter is used to induce the expression of the activating protein. The Ura3 region was chosen as a site of genomic insert as it was previously indicated to have relatively small epigenetic changes with time. Cys4 protein was included in the plasmid in case multiple genes needed to be overexpressed. For this paper only one gene was expressed at a time during induction experiments. To insert a gene of interest, upstream primers containing a Kozak sequence for the start of the coding sequence along with the enzyme AVRII were constructed and the terminator sequence 200bp at the end of the gene was added with a enzyme sequence SBFI. If a gene had a fluorescent tag the terminator past the GFP tag was taken. To insert a gene, restriction digest enzymes AVRII and SBFI were used. Inserts were checked through gel PCR and sanger sequencing. Induction can be measured through live microscopy and is visually seen within 15- 20 minutes of estradiol induction. Flow cell cytometry also confirmed rapid induction and stabilization.

2.5 Proteasome Measurement Assay

Cells were cultured to OD₆₀₀ ~0.8 to 1.0 in 15ml of galactose rich media. Cell pellets were collected by spinning samples down at 1500RPM for 5 minutes and washing in 10ml of deionized water twice. Pellets were then stored in -80 for one night before resuspending in 50µl of cold lysis buffer [50 mM tris-HCl (pH 7.5), 0.5 mM EDTA, 5 mM MgCl₂, and protease inhibitor cocktail tablet; Roche], and p200 was used to squirt cell mixture into a 2.0ml tube. The capped tube was then placed in liquid nitrogen, creating frozen droplets within the tube. Eight 3.0 mm Diameter beads (D1032-30) were then placed inside the tube with frozen droplets. At this point tubes are kept in liquid nitrogen. Cell breakage was performed by mixer milling. Mixer milling was performed three times at a frequency of 30 Hertz for 1 minute, samples and rack were placed back in liquid nitrogen for two minutes between breakage times. At this point the frozen droplets appear as a refined powder. 15µl of cold lysis buffer was then added to the tubes and

samples were allowed to thaw on ice for 15 minutes before supernatant was collected at 13,000 rpm for 8 min at 4°C. Protein concentration was determined by a Bradford assay (Bio-Rad) using bovine serum albumin as standard and 3-5µl of samples. Proteasomal chymotrypsin-like activity was measured by using Suc-LLVY-AMC (Bachem), and proteasomal caspase-like activity was measured by using Ac-nLPnL-AMC (Bachem). Each reaction volume was 200µl, including 50µg of total lysate protein, 100µM peptide substrate, and lysis buffer. The fluorescent intensity was recorded after incubation for 15 min at 30°C in a TECAN with an excitation wavelength of 380nm and an emission wavelength of 460nm. Samples were recorded in the absence or presence of 50µg/ml of the proteasome inhibitor MG132.

2.6 Temporal Ordering with Granger Causality

The primary intention is to determine whether feature 1 is predictive of feature 2 at a later time. The Granger causality is expressed through a combination of Decision Trees and F-test in this analysis. Two datasets representing feature 1 and feature 2 activities at distinct time points were used. Both datasets were aligned based on a common time frame and cell population. The data points were normalized by Singular Value Decomposition (SVD) to equalize the scale. Moreover, the data for each cell were normalized to the 0-1 range to facilitate trend recognition. A Decision Tree Regressor was employed for the Granger causality test. Granger causality is generally used for linear relationships; however, the use of a Decision Tree Regressor allows us to capture the nonlinear relationships between datasets. The trees were optimized by setting the maximum depth as a function of the square root of the number of live cells in the sample, which adapts the model complexity to the data size. Furthermore, the Friedman Mean Squared Error criterion was applied as the function to measure the quality of a split. Time points with less than 56 live dividing cells are excluded. For each time point, the decision tree model predicted the future feature activity based on the feature activity at a previous time. For example, the model would compare whether Rpn11p intensity (feature 1) or nucleus area (feature 2) at time 2 is a better predictor of a later time, time 4 of the nucleus area. These predictions were then compared with the actual future feature 2 activities. The difference between predicted and actual feature 2 activities were calculated and subjected

to an F-test, where the null hypothesis is that the variances of the two sets of differences are equal. The essence of the approach is to capture which model has less variation. The one that has less variation would thereby be a better predictor. The result of this F-test determines the Granger causality: if the p-value of the F-test is below a given significance level (α), it indicates that the past feature 1 activities vs past feature 2 activities have a statistically significant effect on the future feature 2 activities, and hence we can infer that feature 1 predicts feature 2. Finally, the \log_{10} -transformed p-values (signed according to the sign of the F statistic) of the F-tests were assembled into a matrix where rows and columns represent different time points. A rolling window approach was applied with a window size of two where the maximum value within each window was selected. This helped to reduce the noise and increase the signal. Magnitudes less than two standard deviations of the signal greater than zero were turned to zero. Following the thresholding step, a gaussian filter with a $\sigma = 1.2$ was used to further smooth and enhance true feature distinctiveness. This matrix was then visualized using a heatmap, providing a visual overview of the temporal relationship between feature 1 and feature 2 across all time points. The predictive relationships were identified through negative logarithmic p-values, indicating statistically significant Granger causality from feature 1 to feature 2. A greater magnitude of these values represents stronger evidence of causality.

REFERENCES

1. López-Otín, C., Blasco, M. A., Partridge, L., Serrano, M. & Kroemer, G. Hallmarks of aging: An expanding universe. *Cell* **186**, 243–278 (2023).
2. López-Otín, C., Blasco, M. A., Partridge, L., Serrano, M. & Kroemer, G. The Hallmarks of Aging. *Cell* **153**, (2013).
3. Aunan, J. R., Watson, M. M., Hagland, H. R. & Sørdeide, K. Molecular and biological hallmarks of ageing. *British Journal of Surgery* **103**, e29–e46 (2016).
4. Zimmermann, A. *et al.* Yeast as a tool to identify anti-aging compounds. *FEMS Yeast Res* **18**, (2018).
5. Xie, Z. *et al.* Molecular phenotyping of aging in single yeast cells using a novel microfluidic device. *Aging Cell* **11**, 599–606 (2012).
6. Bilinski, T., Bylak, A. & Zadrag-Tecza, R. The budding yeast *Saccharomyces cerevisiae* as a model organism: possible implications for gerontological studies. *Biogerontology* **18**, 631–640 (2017).
7. Janssens, G. & Veenhoff, L. Evidence for the hallmarks of human aging in replicatively aging yeast. *Microbial Cell* **3**, 263–274 (2016).
8. Erjavec, N., Larsson, L., Grantham, J. & Nystrom, T. Accelerated aging and failure to segregate damaged proteins in Sir2 mutants can be suppressed by overproducing the protein aggregation-remodeling factor Hsp104p. *Genes & Development* **21**, 2410–2421 (2007).
9. Hendrickson, D. G. *et al.* A new experimental platform facilitates assessment of the transcriptional and chromatin landscapes of aging yeast. *Elife* **7**, (2018).
10. Lee, S. S., Vizcarra, I. A., Huberts, D. H. E. W., Lee, L. P. & Heinemann, M. Whole lifespan microscopic observation of budding yeast aging through a microfluidic dissection platform. *Proceedings of the National Academy of Sciences* **109**, 4916–4920 (2012).
11. Chen, K. L., Crane, M. M. & Kaerberlein, M. Microfluidic technologies for yeast replicative lifespan studies. *Mech Ageing Dev* **161**, 262–269 (2017).
12. D’Mello, N. P. & Jazwinski, S. M. Telomere length constancy during aging of *Saccharomyces cerevisiae*. *J Bacteriol* **173**, 6709–6713 (1991).
13. Brion, C., Pflieger, D., Souali-Crespo, S., Friedrich, A. & Schacherer, J. Differences in environmental stress response among yeasts is consistent with species-specific lifestyles. *Mol Biol Cell* **27**, 1694–1705 (2016).
14. Neurohr, G. E. *et al.* Dereglulation of the G1/S-phase transition is the proximal cause of mortality in old yeast mother cells. *Genes Dev* **32**, 1075–1084 (2018).
15. Hughes, A. L. & Gottschling, D. E. An early age increase in vacuolar pH limits mitochondrial function and lifespan in yeast. *Nature* **492**, 261–265 (2012).

16. Hughes, C. E. *et al.* Cysteine Toxicity Drives Age-Related Mitochondrial Decline by Altering Iron Homeostasis. *Cell* **180**, 296-310.e18 (2020).
17. Paxman, J. *et al.* Age-dependent aggregation of ribosomal RNA-binding proteins links deterioration in chromatin stability with challenges to proteostasis. *Elife* **11**, (2022).
18. Escusa-Toret, S., Vonk, W. I. M. & Frydman, J. Spatial sequestration of misfolded proteins by a dynamic chaperone pathway enhances cellular fitness during stress. *Nat Cell Biol* **15**, 1231–1243 (2013).
19. Kaganovich, D., Kopito, R. & Frydman, J. Misfolded proteins partition between two distinct quality control compartments. *Nature* **454**, 1088–1095 (2008).
20. Motosugi, R. & Murata, S. Dynamic Regulation of Proteasome Expression. *Front Mol Biosci* **6**, (2019).
21. Kruegel, U. *et al.* Elevated proteasome capacity extends replicative lifespan in *Saccharomyces cerevisiae*. *PLoS Genet* **7**, e1002253 (2011).
22. RINALDI, T. *et al.* Participation of the proteasomal lid subunit Rpn11 in mitochondrial morphology and function is mapped to a distinct C-terminal domain. *Biochemical Journal* **381**, 275–285 (2004).
23. Nillegoda, N. B. *et al.* Ubr1 and Ubr2 Function in a Quality Control Pathway for Degradation of Unfolded Cytosolic Proteins. *Mol Biol Cell* **21**, 2102–2116 (2010).
24. Ju, D., Wang, X., Ha, S.-W., Fu, J. & Xie, Y. Inhibition of Proteasomal Degradation of Rpn4 Impairs Nonhomologous End-Joining Repair of DNA Double-Strand Breaks. *PLoS One* **5**, e9877 (2010).
25. Wang, X., Xu, H., Ha, S.-W., Ju, D. & Xie, Y. Proteasomal Degradation of Rpn4 in *Saccharomyces cerevisiae* Is Critical for Cell Viability Under Stressed Conditions. *Genetics* **184**, 335–342 (2010).
26. Koyuncu, S., Fatima, A., Gutierrez-Garcia, R. & Vilchez, D. Proteostasis of Huntingtin in Health and Disease. *Int J Mol Sci* **18**, 1568 (2017).
27. Vilchez, D. *et al.* Increased proteasome activity in human embryonic stem cells is regulated by PSMD11. *Nature* **489**, 304–308 (2012).
28. Li, S. C. & Kane, P. M. The yeast lysosome-like vacuole: Endpoint and crossroads. *Biochimica et Biophysica Acta (BBA) - Molecular Cell Research* **1793**, 650–663 (2009).
29. Anderson, A. J., Jackson, T. D., Stroud, D. A. & Stojanovski, D. Mitochondria—hubs for regulating cellular biochemistry: emerging concepts and networks. *Open Biol* **9**, (2019).
30. Lavoie, H. & Whiteway, M. Increased Respiration in the *sch9Δ* Mutant Is Required for Increasing Chronological Life Span but Not Replicative Life Span. *Eukaryot Cell* **7**, 1127–1135 (2008).
31. Ohlmeier, S., Kastaniotis, A. J., Hiltunen, J. K. & Bergmann, U. The Yeast Mitochondrial Proteome, a Study of Fermentative and Respiratory Growth. *Journal of Biological Chemistry* **279**, 3956–3979 (2004).

32. Leupold, S. *et al.* Saccharomyces cerevisiae goes through distinct metabolic phases during its replicative lifespan. *Elife* **8**, (2019).
33. Li, Y. *et al.* A programmable fate decision landscape underlies single-cell aging in yeast. *Science (1979)* **369**, (2020).
34. Rafelski, S. M. *et al.* Mitochondrial Network Size Scaling in Budding Yeast. *Science (1979)* **338**, 822–824 (2012).
35. Jorgensen, P. *et al.* The Size of the Nucleus Increases as Yeast Cells Grow. *Mol Biol Cell* **18**, 3523–3532 (2007).
36. Heckenbach, I. *et al.* Nuclear morphology is a deep learning biomarker of cellular senescence. *Nat Aging* **2**, 742–755 (2022).
37. Chan, Y.-H. M. & Marshall, W. F. Organelle Size Scaling of the Budding Yeast Vacuole Is Tuned by Membrane Trafficking Rates. *Biophys J* **106**, 1986–1996 (2014).
38. Chan, Y.-H. M. & Marshall, W. F. Organelle Size Scaling of the Budding Yeast Vacuole Is Tuned by Membrane Trafficking Rates. *Biophys J* **106**, 1986–1996 (2014).
39. Hartmann, C. *et al.* Systematic estimation of biological age of in vitro cell culture systems by an age-associated marker panel. *Frontiers in Aging* **4**, (2023).
40. Dungrawala, H. *et al.* Identification of new cell size control genes in S. cerevisiae. *Cell Div* **7**, 24 (2012).
41. Huh, W.-K. *et al.* Global analysis of protein localization in budding yeast. *Nature* **425**, 686–691 (2003).
42. Ghaboosi, N. & Deshaies, R. J. A Conditional Yeast E1 Mutant Blocks the Ubiquitin–Proteasome Pathway and Reveals a Role for Ubiquitin Conjugates in Targeting Rad23 to the Proteasome. *Mol Biol Cell* **18**, 1953–1963 (2007).
43. Wendler, P. & Enenkel, C. Nuclear Transport of Yeast Proteasomes. *Front Mol Biosci* **6**, (2019).
44. Meller, A. & Shalgi, R. The aging proteostasis decline: From nematode to human. *Exp Cell Res* **399**, 112474 (2021).
45. Liu, X. *et al.* Reliable cell cycle commitment in budding yeast is ensured by signal integration. *Elife* **4**, (2015).
46. Georgieva, M., Roguev, A., Balashev, K., Zlatanova, J. & Miloshev, G. Hho1p, the linker histone of Saccharomyces cerevisiae, is important for the proper chromatin organization in vivo. *Biochimica et Biophysica Acta (BBA) - Gene Regulatory Mechanisms* **1819**, 366–374 (2012).
47. Ogrodnik, M. *et al.* Cellular senescence drives age-dependent hepatic steatosis. *Nat Commun* **8**, 15691 (2017).
48. Reyes, N. S. *et al.* Sentinel p16^{INK4a+} cells in the basement membrane form a reparative niche in the lung. *Science (1979)* **378**, 192–201 (2022).

49. Yao, Z., Gendreau, M., Li, M., Ran, L. & Wang, Z. Service operations of electric vehicle carsharing systems from the perspectives of supply and demand: A literature review. *Transp Res Part C Emerg Technol* **140**, 103702 (2022).
50. Chvosteková, M., Jakubík, J. & Krakovská, A. Granger Causality on forward and Reversed Time Series. *Entropy* **23**, 409 (2021).
51. Karalis, G. Decision Trees and Applications. in 239–242 (2020). doi:10.1007/978-3-030-32622-7_21.
52. Morlot, S. *et al.* Excessive rDNA Transcription Drives the Disruption in Nuclear Homeostasis during Entry into Senescence in Budding Yeast. *Cell Rep* **28**, 408-422.e4 (2019).
53. Scheckhuber, C. Q. *et al.* Reducing mitochondrial fission results in increased life span and fitness of two fungal ageing models. *Nat Cell Biol* **9**, 99–105 (2007).
54. Kaiming He, X. Z. S. R. J. S. Deep Residual Learning for Image Recognition. 1–12 Preprint at (2015).
55. Shirozu, R., Yashiroda, H. & Murata, S. Proteasome Impairment Induces Recovery of Mitochondrial Membrane Potential and an Alternative Pathway of Mitochondrial Fusion. *Mol Cell Biol* **36**, 347–362 (2016).
56. Saarikangas, J. & Barral, Y. Protein aggregates are associated with replicative aging without compromising protein quality control. *Elife* **4**, (2015).
57. Gómez-Schiavon, M., Dods, G., El-Samad, H. & Ng, A. H. Multidimensional Characterization of Parts Enhances Modeling Accuracy in Genetic Circuits. *ACS Synth Biol* **9**, (2020).
58. Ng, A. H. *et al.* Publisher Correction: Modular and tunable biological feedback control using a de novo protein switch. *Nature* **579**, (2020).
59. Janssens, G. E. *et al.* Protein biogenesis machinery is a driver of replicative aging in yeast. *Elife* **4**, (2015).
60. Cheng, W.-C. *et al.* Fis1 deficiency selects for compensatory mutations responsible for cell death and growth control defects. *Cell Death Differ* **15**, 1838–1846 (2008).

Publishing Agreement

It is the policy of the University to encourage open access and broad distribution of all theses, dissertations, and manuscripts. The Graduate Division will facilitate the distribution of UCSF theses, dissertations, and manuscripts to the UCSF Library for open access and distribution. UCSF will make such theses, dissertations, and manuscripts accessible to the public and will take reasonable steps to preserve these works in perpetuity.

I hereby grant the non-exclusive, perpetual right to The Regents of the University of California to reproduce, publicly display, distribute, preserve, and publish copies of my thesis, dissertation, or manuscript in any form or media, now existing or later derived, including access online for teaching, research, and public service purposes.

DocuSigned by:
Michael Mobaraki
175A4007747940F... Author Signature

11/28/2023
Date